Physics – Uspekhi **61** (3) 247 – 279 (2018)

REVIEWS OF TOPICAL PROBLEMS

PACS numbers: **34.10.** + **x**, 34.50.Fa, **34.70.** + **e**

Influence of atomic processes on charge states and fractions of fast heavy ions passing through gaseous, solid, and plasma targets

I Yu Tolstikhina, V P Shevelko

DOI: https://doi.org/10.3367/UFNe.2017.02.038071

Contents

Abstract. An overview of experimental data and theoretical methods is given for charge-changing processes with ion beams passing through gaseous, solid, and plasma targets. The main focus is on electron capture and electron loss processes involving heavy many-electron ions (like Ar^{q+}, Kr^{q+}, Pb^{q+}, W^{q+}, U^{q+}) at relatively large and relativistic ion energies $E = 50$ keV/u – 50 GeV/u, including multielectron processes, which increase the total cross sections to about 50% or more. A large part of the paper is devoted to consideration of the stopping power of matter — the basic quantity characterizing kinetic energy losses of ions due to interactions with particles in matter. The electron capture processes for heavy ions colliding with atoms at low energies $E < 10$ eV/u and the arising isotopic effect are briefly discussed. The formation dynamics of charge-state fractions and average equilibrium charges in the ion beams interacting with medium particles are considered on the basis of the balance rate equations, including the creation of equilibrium charge-state fractions and average charges, an equilibrium target thickness and ion beam average charge, etc. A short description of the computer programs ETACHA, GLOBAL, CHARGE, and BREIT for calculating the charge-state fractions as a function of the target thickness is given, and some applications directly using charge-state fractions, e.g., in the detection of superheavy elements and in solving problems in laboratory and astrophysical plasmas, are considered. All physical processes and effects touched upon in the paper are explained in terms of atomic physics using the radiative and collisional characteristics of heavy many-electron ions interacting with electrons, atoms, ions, and molecules.

I Yu Tolstikhina, V P Shevelko Lebedev Physical Institute, Russian Academy of Sciences,
Leninskii prosp. 53, 119991 Moscow, Russian Federation
Tel. +7 (499) 132 67 15, +7 (499) 132 69 26
E-mail: inga@sci.lebedev.ru, shev@sci.lebedev.ru

Received 10 January 2017, revised 15 February 2017
Uspekhi Fizicheskikh Nauk **188** (3) 267 – 300 (2018)
DOI: https://doi.org/10.3367/UFNr.2017.02.038071
Translated by I Yu Tolstikhina, V P Shevelko; edited by A Radzig

Keywords: ion–atom collisions, effective cross sections, charge-state fractions, balance rate equations, stopping power of matter, electron capture and loss processes

1. Introduction. Role of atomic interactions in the passage of ions through targets

Interactions of ion beams with media particles, occurring in their penetration through gaseous, solid, and plasma targets, are of interest for solving fundamental problems in atomic and nuclear physics, plasma and accelerator physics, as well as for mastering many new applications — from cancer ion–beam therapy to constructing modern powerful heavy-ion accelerators, from detecting superheavy chemical elements to modeling biochemical reactions in living cells [1–10].

The interaction of ions with media particles and the evolution of ion–beam fractions are determined by the properties of electron–ion and ion–atom processes, as well as photo-processes related to radiation and absorption of photons. Information on atomic characteristics (effective cross sections, radiative and Auger transition probabilities, and others) are needed for investigations in many fields of atomic physics and atomic spectroscopy, plasma physics, quantum electronics, accelerator physics, and thermonuclear fusion, as well as for creating reliable methods of spectroscopic and corpuscular diagnostics of laboratory and astrophysical plasmas. Basic features of atomic processes governing interactions of ions with target particles, such as dependences on relative velocity and the atomic structure of colliding particles and target-density effects, are considered in many review articles and books [11–26].

In recent years, due to intensive development of accelerating technology, the interest in investigations of atomic processes involving heavy many-electron projectile ions like Ar^{q+}, Xe^{q+}, Au^{q+}, W^{q+}, Bi^{q+}, and U^{q+} has significantly increased because of their key role in thermonuclear fusion [27, 28], the slowing down of ion beams in matter [29], the fragmentation of exotic nuclei [30], the generation of extreme states of matter [31], astrophysics [32], investigations of new materials structures [33], and other fields. Information about international databanks on the electronic structure of atoms and ions and effective cross sections of electron–atom, ion–atom, and other collisional processes can be found on the IAEA website [34].

The design of modern heavy-ion accelerators and storage rings is based on optimization of the so-called *vacuum conditions*, i.e., a residual-gas composition and a gas density in order to reach minimum ion losses and maximum ion–beam lifetimes. These principles are the focus of international projects such as FAIR (Facility for Antiproton and Ion Research), started at GSI, Darmstadt, in 2011 [35]. Another important example is given by the NICA Project (Nuclotron-based Ion Collider fAcility), a Russian collider of protons and heavy ions being constructed around the Nuclotron accelerator at JINR, Dubna, in order to create a high-density material in collisions of gold ions (atomic number $Z = 79$) with a kinetic energy of about 10 GeV/u. The project began to be developed from 2013, and a construction of the accelerator was started in March 2016.

Interest in processes of ion interactions with media arose more than 100 years ago in experimental investigations of ion neutralization in collisions with gaseous targets [36]. Later on, a significant contribution to those investigations was made by many well-known physicists, including L D Landau, P V Vavilov, W L Bragg, W E Lamb, N Bohr, J Lindhard, N O Lassen, E Teller, H D Betz, H G Berry, and K Shima (see Refs [1, 9, 10]). At the present time, experiments involving heavy ions are being carried out at leading world-class accelerators in Dubna JINR (Russia), CERN (Switzerland), GANIL (France), UNILAC (Germany), NSCL (National Superconducting Cyclotron Laboratory) and SuperHILAC (Super Heavy Ion Linear ACcelerator) (USA), RIKEN (Japan), and HIRFL (Heavy Ion Research Facility in Lanzhou) (China).

In the penetration of a heavy-ion beam with a certain charge state through matter (gas, plasma, solid), beam ions interact with the target atoms, molecules, ions, and electrons, resulting in the formation of charge-state ion *fractions* $F_q(x)$ with different charge states q and individual evolutions as a function of the penetration depth (target thickness) x. At relatively large x, significantly exceeding ion mean free path L in the media, $x \gg L$, the fractions $F_q(x)$ become independent of x and the charge state of ions in the incident beam and reach the so-called *equilibrium distribution*. The charge-state fractions at equilibrium are called *equilibrium* ion fractions, and correspond to establishing balance between the number of ionization and recombination events occurring with ions having a given charge and colliding with the target particles.

The aim of this survey is to present information about state-of-the art experimental data on charge-changing processes involving heavy ions with kinetic energies of $50\ \mathrm{keV/u} < E < 10\ \mathrm{GeV/u}$, which penetrate through gaseous, plasma, and solid targets, as well as theoretical methods and computer programs for calculating interaction cross sections, equilibrium and nonequilibrium charge-state fractions, mean charges of ion beams, and other characteristics.

The main attention is paid to the consideration of heavy many-electron projectiles and target atoms, i.e., atomic systems having more than one electron shell. These systems are of great interest from both experimental and theoretical points of view: the presence of a large number of electrons in colliding systems often leads to situations where the inner-shell electrons play an essential, and even the main role. For example, multiple-electron ionization and recombination (electron capture) of ions in collisions with neutral atoms leads to an increase in the total cross sections up to more than 50%, which, in turn, strongly influences the evolution of the charge-state fractions and their mean charges. Explanations of physical processes and different effects are made in terms of the atomic physics, i.e., using the properties of atomic elementary radiative and collisional processes.

The system of atomic units is used throughout: $m = \hbar = e = 1$, where m and e denote electron mass and charge, respectively, and $\hbar$ is the Planck constant. In atomic units, the Bohr length and velocity are $a_0 = \hbar^2/me^2 = 1$, and $v_0 = e^2/\hbar = 1$.

1.1 Gaseous targets

Usually, H_2 and N_2 gases are used as targets, as are inert gases He, Ar, Kr, and Xe in two versions: in a gas cell with solid windows or jet-based gas injection. In the gas cells, the gas density is rather high ($\sim 100\ \mu\mathrm{g\ cm}^{-2}$) to minimize corrections due to passing through solid windows.

The gas-jet targets are used in storage rings or to determine the collision cross sections, when it is necessary to provide one-collision conditions, i.e., to take advantage of relatively low gas densities. One of the main disadvantages of using gas-jet targets is the large scattering angles (angle struggling), which make the detection of collision events quite difficult. For such gas systems, special control methods are applied, where the gas injection is synchronized with the pulsed timing of the accelerator (see, e.g., Ref. [29]).

1.2 Solid targets (foils)

Foils are usually made from metallic elements beginning with Be ($Z = 4$) and ending with U ($Z = 92$), where Z is the atomic number. The manufacturing technique of the foils depends on their material and thickness, which varies from a few μg cm^{-2} for keV/u-energy ion beams up to a few g cm^{-2} for relativistic ions [29, 37]. Carbon ($Z = 6$) foils are used most often, because they are produced with a high accuracy. In recent years, multilayer foils produced from different chemical elements have come to be of special interest in obtaining an ion beam with the required charge at the output (see report [38] and references cited therein).

We note that in a large number of experiments, e.g., on the detection of superheavy elements, foils should not be destroyed and retain their atomic properties during long-term interaction with a high-energy ion beam. To a large extent, this relates to a thick foil substrate (for example, C), on which a thin layer of a heavy element (for example, Pb) is deposited, which actually participates in the synthesis process. In this case, the foil lifetime, i.e., the time before its destruction, depends mainly on the radiation interaction with the incident ion beam and the target evaporation, and varies from fractions of a second to hundreds of hours, depending on the type of the foil material, energy, and charge state of the beam before and after passing through the target [39]. Calculations of the properties of such foils and their lifetimes are performed taking into account the thermodynamic and hydrodynamic conditions, which the solid targets have to satisfy (see, for example, papers [40, 41]).

1.3 Plasma targets

The interaction of heavy-ion beams with plasma targets is used to study inertial thermonuclear fusion and beam plasma diagnostics, and to obtain the maximum possible average charge of the emergent ion beam. For these purposes, special gas-discharge devices have been designed, consisting mainly of a quartz tube and a gas in it at a pressure of several Torr [29, 42, 43]. A composition of gas-discharge plasmas (atoms, ions, molecules, molecular ions, and electrons) depends on the type of gas, plasma density, and temperature [44, 45]. The interaction of ion beams with D – T plasmas is of a particular interest [46, 47]. The determination of plasma temperature and density is usually carried out by spectroscopic methods, laser interferometry, or absorption techniques [48, 49].

An important way to study the interaction of ion beams with plasma targets is to increase the average charge of the ion beam at the output (and, hence, the *stopping power*) 10 or more times compared to a cold gas target made of the same element. This occurs in the so-called *plasma windows*, corresponding to certain ion beam energies, when the probability of capturing the bound electrons from neutral atoms is much less than the probability of radiative electron capturing (radiative recombination) the plasma free electrons [48–50].

1.4 Liquid targets

Besides the pure physical interest in studying the properties of liquids, the interaction of ion beams with such targets is also of practical importance for biological research and medicine, especially for beam therapy of cancer tumors [6, 7]. For example, ionization of cancer tumors by protons and carbon nuclei with energies of the order of several MeV/u is effectively used in many medical centers in Russia, the USA, Japan, and Germany. That is why the interaction of ion beams with water molecules, which the human body mainly consists of (80%), is studied most intensively. Certainly, there are still many problems to be solved, related to the structure of complex molecules and secondary electron ionization of cells, which can lead to a greater cell damage than the primary ion flux, and some others [51–53].

2. Characteristics of ion beams interacting with the medium

In its passage through media, an ion beam losses kinetic energy due to interaction with media particles, and the energy spread and the scattering angle increase. Below, a brief discussion is given on the characteristics of ion beams after passing through media, which depend mainly on the *stopping power* of matter (see Section 3).

2.1 Kinetic energy loss

As a result of the ion beam interaction with media particles, it loses part of its kinetic energy, so that the energy distribution shifts toward lower energies and becomes wider (Fig. 1a). The energy loss $\langle \Delta E \rangle$, averaged over all collisions, is determined by collisional-fluctuation losses due to three main processes — ionization, recombination, and charge-state fluctuations — and depends on the penetration depth of the ion beam in the target.

The energy loss $\langle \Delta E \rangle$ is defined by the following expression [10]:

$$\langle \Delta E \rangle = Nx \sum_i T_i \sigma_i = Nx \int T \, \mathrm{d}\sigma = Nx \int T \frac{\mathrm{d}\sigma}{\mathrm{d}T} \, \mathrm{d}T \,, \qquad (1)$$

where N is the density of target atoms, x is the penetration depth, T is the energy loss in one collision, and σ is the energy-loss cross section [10, 20, 54]. Angle brackets $\langle \ldots \rangle$ stand for statistical averaging over all collisions of ions with media

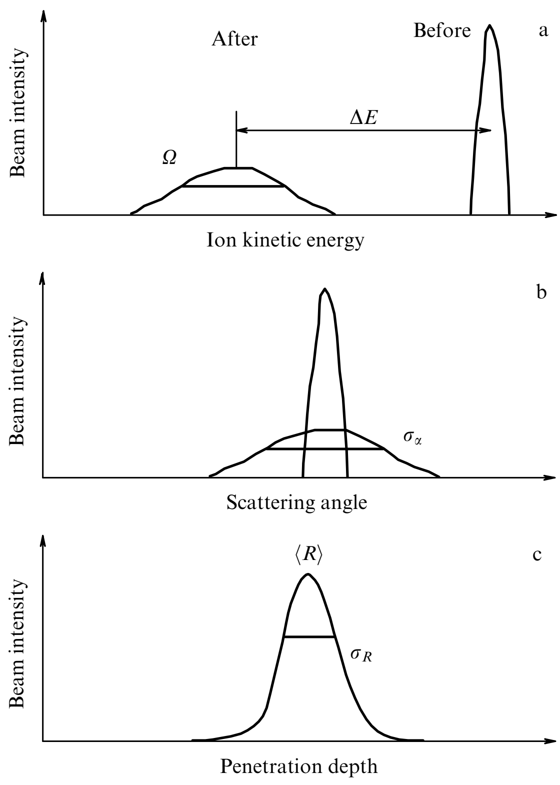

Figure 1. Properties of an ion beam as it passes through a medium: (a) losses and broadening of the beam in energy; (b) spread in the scattering angles, and (c) penetration depth (particle range). (Taken from Ref. [54].)

particles. At relatively low ion energies $E \sim 10-100$ keV/u, the energy losses are determined mainly by elastic collisions with the nuclei of media atoms, and at higher energies $E \sim 10-100$ MeV/u by inelastic collisions with target electrons, accompanied by electron capture (charge-exchange) processes and ionization of projectile ions (*stripping*) and target atoms (Section 3.3).

In practice, the ion kinetic energy loss is defined by the *stopping power* $\mathrm{d}E/\mathrm{d}x$ of ions in media by the formula

$$\Delta E = -\int_0^L \frac{\mathrm{d}E}{\mathrm{d}x}\,\mathrm{d}x\,, \tag{2}$$

where L is the target thickness, and the function $\mathrm{d}E/\mathrm{d}x$ can be taken from various tables (see, for example, Ref. [55]) or calculated by the SRIM program (Stopping and Ranges of Ions in Matter) [56] (see Section 3 for more details).

In a dense medium, the energy profile of a beam scattered due to multiple collisions is close to a Gaussian function with a width Ω called the *energy loss straggling*, which has the form [10]

$$\Omega^2 = \left\langle \left(\langle\Delta E\rangle - \Delta E\right)^2 \right\rangle = Nx\sum_i T_i^2\sigma_i = Nx\int T^2\,\mathrm{d}\sigma = Nx\int T^2\,\frac{\mathrm{d}\sigma}{\mathrm{d}T}\,\mathrm{d}T\,. \tag{3}$$

In general, obtaining Ω in a closed analytical form is a very complicated problem, but in the special case of two ion fractions with charges q_0 and q_1, the width of the energy spread due to the influence of atomic processes assumes the form [57, 58]

$$\Omega^2 = 2L\,\frac{F_0^\infty F_1^\infty}{N(\sigma_{01}+\sigma_{10})}\left[\frac{\mathrm{d}E}{\mathrm{d}x}(q_0) - \frac{\mathrm{d}E}{\mathrm{d}x}(q_1)\right]^2, \tag{4}$$

where L and N are the target thickness and density, respectively, σ_{01} and σ_{10} are electron-loss and electron-capture cross sections, $F_{0,1}^\infty$ are the *equilibrium fractions* (Section 4), and $\mathrm{d}E/\mathrm{d}x\,(q)$ are the partial stopping powers.

In a *low-density* medium (rarefied gas), the energy profile of the beam is described by the Landau–Vavilov formula [59, 60]. The spread of energy losses in *relativistic* collisions is considered in paper [61].

The exact energy distribution of ions escaping the target is required for many applications, e.g., for the manufacture of electronic chips and semiconductor detectors and in cancer therapy, where it is necessary to know accurate values of ion energies before and after interaction with the patient's body. Methods for measuring beam energies in the range keV/u–MeV/u are described in Refs [5, 62].

2.2 Angular straggling. Radiation length

An important property of an ion beam passing through media is its angular spreading due to elastic scattering on media particles, when a well-collimated ion beam becomes broadened in scattering angles, as shown in Fig. 1b.

Multiple scattering of ions by particles of the medium has been considered in various theoretical (e.g., Refs [63–65]) and experimental (see Ref. [29]) studies. In practice, to determine the width σ_α for a Gaussian distribution, the following expression is used [64]:

$$\sigma_\alpha^2\;[\mathrm{rad}^2] = \frac{Z_1^2\,199\;\mathrm{MeV}^2}{(p\beta c)^2}\,\frac{L}{L_{\mathrm{rad}}}\left(1+\frac{1}{9}\log\frac{L}{L_{\mathrm{rad}}}\right), \tag{5}$$

where L is the target thickness, Z_1 and p are the charge and momentum of the incident ion, L_{rad} is the *radiation* length, and $\beta = v/c$.

By the radiation length is meant the distance, at which the intensity of gamma radiation and the flux of high-energy electrons are attenuated by a factor of e. Radiation length is usually given in units of g cm^{-2}, i.e., in a form independent of the aggregate state of matter (liquid, gas, or solid) and can be estimated by the expression [66]

$$L_{\mathrm{rad}} \approx \frac{1432.8\,M}{Z(Z+1)(11.319-\ln Z)}\;[\mathrm{g\;cm^{-2}}]\,, \tag{6}$$

where Z is the atomic number, and M is the atomic mass of the target atom. To express the radiation length in cm, one has to divide L_{rad} in Eqn (6) by the density of matter in its aggregate state. For example, substituting $Z = 82$, $M = 207$ for lead (Pb) atoms in Eqn (6) one obtains $L_{\mathrm{rad}} = 6.37$ g cm^{-2}, so that in solid Pb with density 11.34 g cm^{-3} one has $L_{\mathrm{rad}} = 0.57$ cm.

2.3 Penetration depth (ion range)

Heavy ions passing through matter interact mainly with target electrons and deflect little from the direction of their motion, so their trajectories are close to rectilinear. Therefore, the *range* (or *penetration depth*) of a heavy particle is determined by the distance from the ion source to the point at which the ion completely stops. The magnitude of the path of the beam, like the kinetic energy loss or angular spreading, is determined by the stopping power $\mathrm{d}E/\mathrm{d}x$ of the substance, and the penetration depth R of the ion beam with initial energy E_0 is given by the expression (see Fig. 1c)

$$R(E_0) = \int_0^{E_0}\left(-\frac{\mathrm{d}E}{\mathrm{d}x}\right)^{-1}\mathrm{d}E\,. \tag{7}$$

The range R is expressed in cm or g cm^{-2}, depending on the units in which the stopping power is specified.

Since the stopping power depends on the characteristics of the incident ions and penetrable substance approximately as

$$\left|\frac{\mathrm{d}E}{\mathrm{d}x}\right| \sim \frac{Z_1^2}{v^2}\,\rho\,, \tag{8}$$

the particle range shows the following dependences:

$$R \sim \frac{Mv^4}{Z_1^2\rho} \sim \frac{E^2}{MZ_1^2\rho}\,, \tag{9}$$

where M, v, E, and Z_1 are mass, velocity, energy, and charge of the incident ion, respectively, and ρ is the density of the target material. Therefore, for a fixed particle velocity, the range is proportional to the particle mass and inversely proportional to its charge, and for a fixed energy the range is inversely proportional to the particle mass. Since the stopping power increases with increasing the electron density of the substance and the ion charge, then the beam range R decreases. For example, the range of 10-MeV alpha particles in air and an aluminum target is $R = 11.0$ and 0.007 cm, respectively.

Information on the ion ranges in media is required for many applications in radiation physics, biology, etc. The ranges of ions in various media are given in books [5, 9, 10].

The slowing-down time of a particle with an initial energy E_0 in matter is determined by the expression

$$T_{\text{stop}} = \int_0^{E_0} \left(-v\, \frac{\mathrm{d}E}{\mathrm{d}x} \right)^{-1} \mathrm{d}E\,. \tag{10}$$

3. Stopping power of matter

3.1 Definition of stopping power

In passing through a substance, a fast ion experiences tens of thousands of collisions with the target particles, gradually losing its kinetic energy E. The energy loss is characterized by the *stopping power* (SP) of matter $\mathrm{d}E/\mathrm{d}x$, where $\mathrm{d}E$ is the energy lost by the ion in a target layer of thickness $\mathrm{d}x$ [5, 67]:

$$-\frac{\mathrm{d}E}{\mathrm{d}x}\bigg|_{E=E_1} = \lim_{\Delta x \to 0} \frac{E_0 - E_1}{\Delta x} > 0\,. \tag{11}$$

Here, E_0 and E_1 are the kinetic energies (in eV) of ions before and after their passage through a target layer Δx (in cm). The quantity defined in Eqn (11) is called the *linear stopping power* and has the dimension of eV cm^{-1}.

The kinetic energy, lost by a charged particle during its passage through matter, is often called *ionization loss* because in many cases the ion energy losses are also related to the target-particle ionization. Information on the SP for ions in matter is necessary for solving many problems in accelerator physics, thermonuclear synthesis, medicine, etc.

Measurements of SPs as a function of the ion energy are carried out at a fixed thickness of the target and consist in measuring the beam energy in the presence of the target and without it in the beam line. At present, SPs in the energy range of $E \sim 1$ keV/u–200 GeV/u are being thoroughly investigated starting for protons and ending for uranium ions (see, for example, Refs [68–72]). For relativistic energies, experimental data on SPs were obtained mainly at CERN [70], GSI (Darmstadt) [69, 72], and BEVALAC (Berkeley) [3].

In the relativistic Born approximation, the stopping power for a heavy charged particle with a charge Z_1 as a function of energy has the form (the Bethe–Bloch approximation) [67, 73]

$$-\frac{\mathrm{d}E}{\mathrm{d}x} = \frac{4\pi e^4}{m}\, \frac{Z_1^2}{c^2\beta^2}\, N_\mathrm{e} \left(\ln \frac{2mc^2\beta^2}{I} + \ln \gamma^2 - \beta^2 \right), \tag{12}$$

where m and e are the electron mass and charge, respectively, $\beta = v/c$, with v being the ion velocity, N_e is the electron density, I is the average excitation energy of the target atom, and γ is a relativistic factor.

Equation (12) was obtained at relativistic energies for bare nuclei with a charge $Z_1 = Z_\mathrm{N}$, where Z_N is the nuclear charge, although it is often utilized for many-electron ions and nonrelativistic energies by introducing an effective charge Z_{eff} instead of Z_1. Because of the electron screening, the effective charge of heavy many-electron ions is always less than the nuclear charge, $Z_{\text{eff}} < Z_\mathrm{N}$, and, generally speaking, depends on the ion velocity v (see Section 3.2).

The electron (N_e) and atomic (N_{at}) densities of matter are related as

$$N_\mathrm{e} = ZN_{\text{at}} = \frac{ZN_\mathrm{A}\rho}{M}\,, \tag{13}$$

where $N_\mathrm{A} = 6.022 \times 10^{23}$ is the Avogadro constant, and Z, M, and ρ are the atomic number, atomic mass in a.m.u., and the density of matter in g cm^{-3}, respectively. Atomic masses M of atoms are given in the Periodic Table of elements.

In the nonrelativistic case, formula (12) takes the form

$$-\frac{\mathrm{d}E}{\mathrm{d}x} = \frac{4\pi e^4}{mv^2}\, Z_1^2 Z N_{\text{at}} \ln \frac{2mv^2}{I}\,, \tag{14}$$

which coincides with that given in book [74]. Formula (14) was obtained within the framework of the theory of collisions for 'effective slowing down', i.e., for the average energy loss κ of the incident ion in matter:

$$-\frac{\mathrm{d}E}{\mathrm{d}x} = N_{\text{at}}\kappa\,, \qquad \mathrm{d}\kappa = \sum_n (E_n - E_0)\,\mathrm{d}\sigma_n\,, \tag{15}$$

where E_0 and E_n are the energies of the ground and excited states, and σ_n are the excitation and ionization cross sections of the target-atom inelastic collisions, respectively. The summation is made over atomic states in the discrete and continuous spectra. In the derivation of Eqn (14), the first order of the perturbation theory in the dipole approximation for the cross sections is used, and the sum rule for dipole oscillator strengths f_{0n} of $0-n$ transitions with transition energies $E_n - E_0$ is written as

$$\sum_n f_{0n} \equiv \sum_n \frac{2m}{(e\hbar)^2}(E_n - E_0)\big|(d_x)_{0n}\big|^2 = Z\,,$$

where $d_x = e\sum_i x_i$ stands for the x-component of the total dipole moment of the target atom.

The *average excitation energy* I of the target atom under the logarithms in Eqns (12) and (14) is determined by the relation

$$\ln I = \frac{\sum_n f_{0n} \ln (E_n - E_0)}{\sum_n f_{0n}} = \frac{1}{Z}\sum_n f_{0n} \ln (E_n - E_0)\,.$$

Thus, the origin of quantities under the logarithm sign becomes evident from the derivation of this equation: the dependence $Z_1^2(\ln v^2)/v^2$ follows from the asymptotic behavior of the excitation and ionization cross sections at high velocities v, while the average excitation energy I comes from summation of κ over excited states of the target atom.

In Fig. 2, the recommended average excitation energies I of neutral atoms are given as a function of the atomic number Z. In the literature, the semiempirical Bloch formula is often utilized: I [eV] $\approx 10Z$, which gives the average value shown in Fig. 2.

Along with the linear stopping power defined in Eqn (11), the *mass stopping power* is used:

$$-\frac{1}{\rho}\,\frac{\mathrm{d}E}{\mathrm{d}x}\ [\text{MeV cm}^2\ \text{g}^{-1}]\,, \tag{16}$$

which is independent of the density of matter ρ.

A comparison with the experimental data (see paper [29]) showed that the Bethe–Bloch formula (12) is applicable for the following values of the collision parameter:

$$\frac{Z_1\alpha}{\beta} = \frac{Z_1}{v} \leqslant 1\,, \tag{17}$$

where Z_1 and v are the charge and velocity of the incident ion, respectively, and $\alpha = 1/137$ is the fine-structure constant.

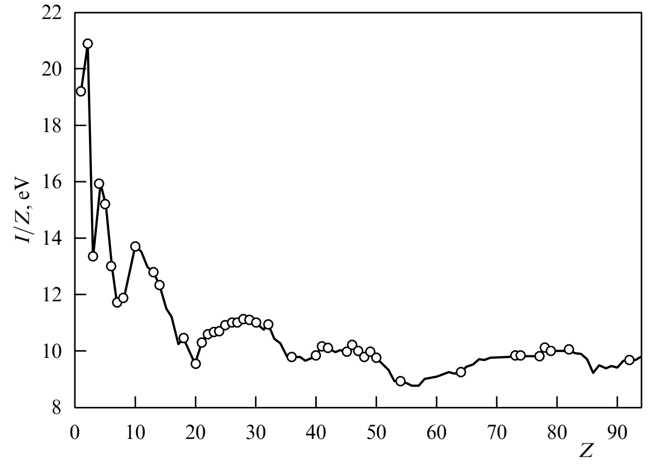

Figure 2. Recommended I/Z values (in eV) of neutral atoms as a function of atomic number Z. Oscillations of the curve reflect the influence of atomic electron-shell structure. (Taken from Ref. [75].)

As the parameter Z_1/v increases, experimental data for SPs begin to disagree with calculated results using the Bethe–Bloch formula (12). For a more accurate description of the stopping power for a large class of ions, atomic targets, and energies, the Lindhard–Sørensen approximation based on the Dirac equation [67] is applied with account for higher-order corrections: the Bloch correction for close relativistic collisions [76], the Barkas correction for polarization effects of the target atoms [77], the Fermi correction for density effects [78], the nuclear finite-size correction [67], shell effects [75], and others.

Figure 3a shows experimental relative SPs for relativistic bare nuclei from O to U in the Be target as a function of the collision parameter (17) at $\beta = 0.84$ in comparison with the Bethe–Bloch and Lindhard–Sørensen models. It is seen that with Z_1/v increasing, the experimental data come to be in good agreement with the Lindhard–Sørensen model.

If experiments with relativistic *bare* nuclei are in relatively good agreement with the Lindhard–Sørensen theory, the situation with many-electron ions is not so simple: with decreasing energy of incident ions, their *effective* charge $Z_{\rm eff}$ becomes much less than the nuclear charge due to electron screening effects and the influence of atomic charge-changing processes (loss and capture). Figure 3b plots ratios of the experimental SPs to those calculated in the Lindhard–Sørensen theory for Au, Pb, and Bi ions with charges close to *equilibrium* ones, when the ions with energies of 100 MeV/u–1 GeV/u pass through foils made of materials from Be to Pb. At energies $E < 300$ MeV/u, the ratios become less than unity, i.e., $Z_{\rm eff} < Z_{\rm N}$, which indicates the influence of the strong screening effects on the ion charges in the medium.

3.2 Effective charge of an incident ion. Stopping power tables

A projectile ion passing through matter changes its charge due to atomic interactions with medium particles, which requires the introduction of an average or *effective charge* $Z_{\rm eff}$, depending, in general, on the impact parameter and ion energy. The effective charge plays an important role in the theory of the slowing-down of ions in matter and is still the subject of detailed studies (see Refs [83–89]). Determining $Z_{\rm eff}$ of ions in plasmas is an especially difficult task because of the Debye screening of the Coulomb ion potential by free plasma electrons (see papers [88, 89] and Section 3.5).

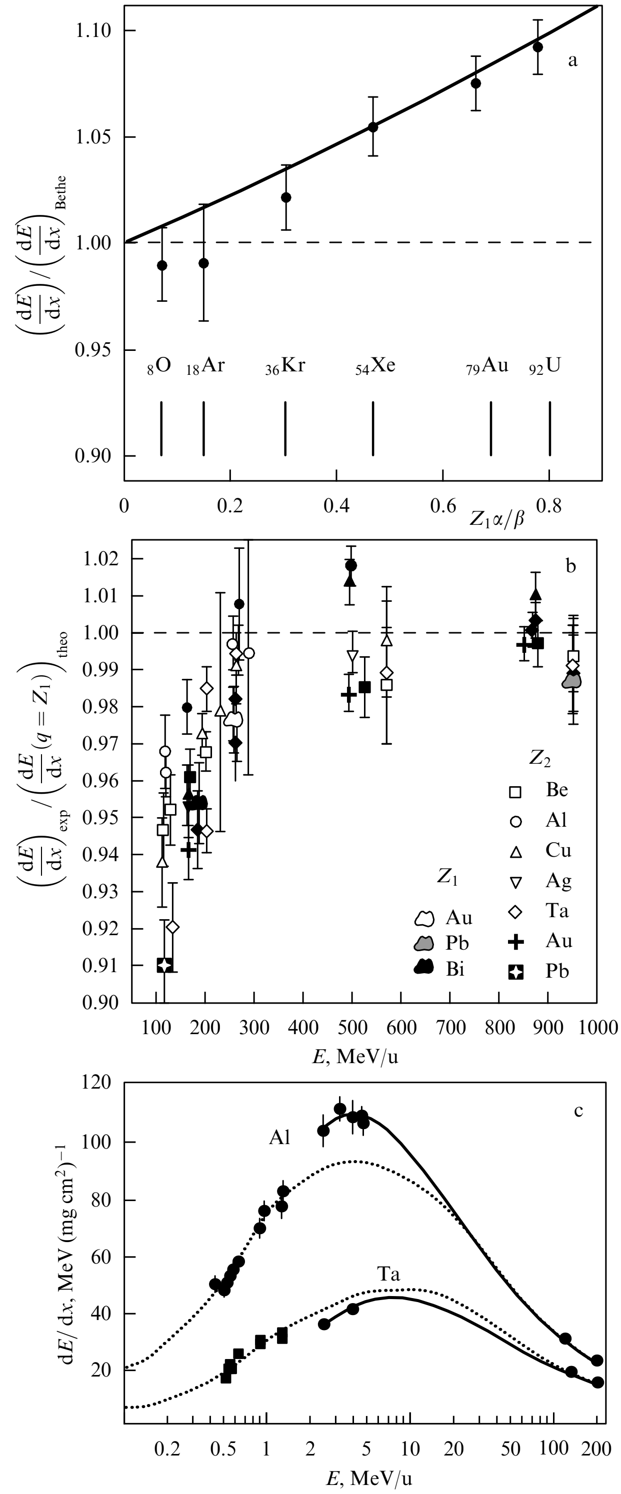

Figure 3. (a) Relative SPs for bare nuclei from O ($Z_1 = 8$) to U ($Z_1 = 92$) passing through a beryllium target at $\beta = 0.84$ ($v = 115.1$ a.e.) as a function of collision parameter (17): dots — experiment, dotted curve — Bethe–Bloch approximation (12), and solid curve — Lindhard–Sørensen approximation [67]. (Taken from Ref. [79].) (b) Ratios of experimental SP data for Au, Pb, and Bi ions in foils from Be to Pb to calculated ones obtained by the Lindhard–Sørensen theory as a function of ion energy. (Taken from Ref. [80].) (c) Experimental SP data for Pb ions in Al- and Ta-foils [69, 80, 81] (symbols) in comparison with semiempirical data of tables [65] and [82] (solid and dashed curves, respectively). (Taken from Ref. [29].)

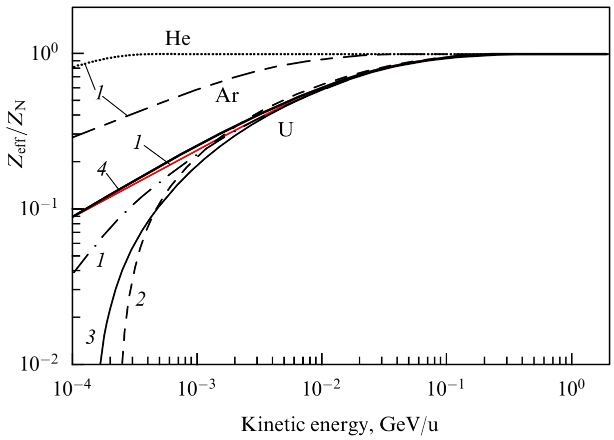

Figure 4. Ratios $Z_{\rm eff}/Z_{\rm N}$ calculated in different models for He, Ar, and U ions colliding with aluminum foil as a function of ion energy: *1* — from formula [5], *2* — [82], *3* — [83], and *4* — [84]. (Taken from Ref. [87].)

Since there is no unique general approach to the definition of $Z_{\rm eff}$, in practice, empirical or semiempirical formulas for $Z_{\rm eff}$ are used. So, in tables of the SPs for *many-electron ions*, scaling laws are adopted which were obtained on the basis of experimental data for protons and other light ions (He^+, α-particles) in the form

$$\left[\frac{{\rm d}E}{{\rm d}x}(E)\right]_{M_{\rm i},\, Z_{\rm eff}} = Z_{\rm eff}^2\left[\frac{{\rm d}E}{{\rm d}x}\left(\frac{E}{M_{\rm i}}\right)\right]_{\rm proton}, \qquad (18)$$

where $M_{\rm i}$, $Z_{\rm eff}$, and E are the mass (in units of proton mass), the effective charge, and the ion energy in MeV, respectively. The effective charge is often determined from simple physical assumptions or by fitting measured data to those for light nuclei as the exponential dependence on the ion velocity v. To estimate the effective charge $Z_{\rm eff}$, the following formula is often used [83]:

$$Z_{\rm eff}(v) = Z_{\rm N}\left[1 - \exp\left(-0.95 v Z_{\rm N}^{-2/3}\right)\right], \qquad (19)$$

where v and $Z_{\rm N}$ are the ion velocity and nuclear charge of the incident ion. The semiempirical correction of experimental data for complex ions makes it possible to describe and predict the stopping-power values rather well for many-electron ions in a wide energy range.

Figure 4 shows calculated relative values of $Z_{\rm eff}/Z_{\rm N}$ for He, Ar, and U ions colliding with aluminum foil as a function of ion energy. For energies $E > 50$ MeV/u, projectile ions are completely stripped to bare nuclei. At low energies, heavy Ar and U ions experience the strongest influence of the screening effects.

Tables of experimental SP data for many ions and targets may be found in Refs [5, 82, 90–92], as well as on the NIST [93] and ICRU [94] (International Commission on Radiation Units and Measurements) websites. A detailed comparative analysis of the available experimental and theoretical data on SPs for ions from Li to Kr at energies of 0.001–1000 MeV/u is given in Ref. [95].

Tables [66] present the SPs for ions with nuclear charges $2 \leqslant Z_{\rm N} \leqslant 103$ at energies of 0.0125–12 MeV/u, based on experimental studies in gases and foils. The semiempirical scaling formula (18) treating proton SP data was applied for heavy ions with effective charges $Z_{\rm eff}$ depending on the nuclear charge $Z_{\rm N}$ and ion velocity v. Since the amount of experimental information at that time was rather limited, sometimes the accuracy of the tables [66] is quite poor — not exceeding 50%. The SPs in foils at energies of 2.5–500 MeV/u are given in Refs [85, 92] using the rather complicated dependences of $Z_{\rm eff}$ on $Z_{\rm N}$ and v. Examples of making use the fitting tables for estimating the SPs for Pb ions are demonstrated in Fig. 3c.

3.3 Dependence of the mass stopping power on ion energy

On the basis of available experimental and theoretical data, it is possible to present schematically a general SP dependence on the ion energy. The qualitative dependence of the mass stopping power on ion energy E is illustrated in Fig. 5.

At low ion energies $E < 1$ keV/u, the SP is formed due to elastic collisions, accompanied by the transfer of some of the ion kinetic energy to the target *nuclei*. With an increase in ion energy $E > 10$ keV/u, the slowing-down of ions in a medium proceeds due to the interaction of colliding particles with electrons of both target atoms and projectile ions. In the range of ion velocities of 1 a.u. $< v < v_{\rm e}$, where $v_{\rm e}$ is the average orbital electron velocity in the target, the SP increases due to inelastic processes such as electron loss and electron capture. Then, according to the Lindhard–Sørensen theory, the SP reaches its maximum at $v \sim v_{\rm e}$, and decreases by the law $\sim v^{-2}$ to its minimum, as follows from the Bethe–Bloch formula (12):

$$-\frac{1}{\rho}\frac{{\rm d}E}{{\rm d}x}\bigg|_{\rm min} \approx 1.7\ {\rm MeV\ cm^2\ g^{-1}}\,, \qquad \beta\gamma \approx 3.5\,. \qquad (20)$$

In the energy range covering $10 - 10^3$ MeV/u, the main ion losses are due to electron excitation and ionization of target atoms, and a v^{-2} law of SP decrease is the same as for corresponding collision cross sections. With a further energy increase, the SP increases as $\sim \ln\gamma$ due to the relativistic effects described by the logarithmic term in formula (12).

At superrelativistic energies $E > 10^6$ MeV/u ($\beta\gamma \geqslant 100$), the relativistic growth in ion energy losses is compensated for by the density effects, and the function ${\rm d}E/{\rm d}(\rho x)$ becomes independent of ion energy, reaching a constant value called the *Fermi plateau* [78].

Several computer programs were implemented for numerical calculations of SPs for ions: SRIM (Stopping and Range of Ions in Matter) and TRIM (TRansport of Ions in Matter) [56], MSTAR [96, 97], and others.

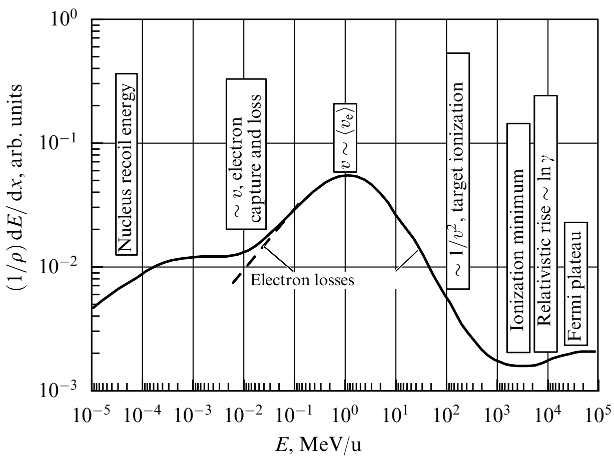

Figure 5. Dependence of the *mass* stopping power ${\rm d}E/{\rm d}(\rho x)$ on ion energy.

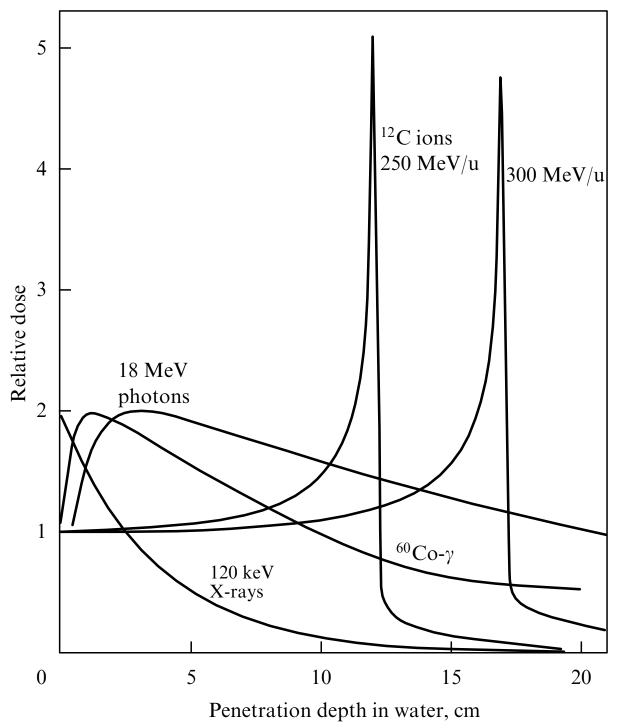

Figure 6. The shape and depth of penetration of the incident *photon* flux of different wavelengths and carbon *ions* (Bragg peaks at 250 and 300 MeV/u) when passing through water. (Taken from Ref. [6].)

3.4 Bragg peak

An important property of the stopping power lies in its dependence on the target *thickness*, which is exhibited in the so-called *Bragg peak* [98]. When a fast ion passes through a thick target, its velocity drops to zero (a complete stopping), and its stopping power increases with decreasing velocity due to an increase in the target-atom ionization cross section as v^2. Simultaneously, the SP reaches its maximum and dramatically decreases at a certain distance called the *particle range* (Fig. 6).

The presence of a Bragg peak in the ionization loss curve is widely used in applications for tumor therapy (mainly in cancer therapy [6, 7, 99]) exploiting proton or heavier ion beams (C^{q+}, N^{q+}), since in the latter case the radiation dose peak can be reached at a larger penetration depth into tissue than with photon radiation. The magnitude and position of the Bragg peak can be regulated by the choice of energy and type of ion, allowing great advantages of employing ion therapy over a short-wavelength photon irradiation, as shown in Fig. 6.

3.5 Stopping power in plasmas

The theoretical problems of ion deceleration in plasmas have been considered in many studies (see, e.g., Refs [50, 89, 100–107]). If the projectile-ion velocity v is larger than the electron thermal velocity $v_{\rm th}$ in plasma, the SP of plasma free electrons for nonrelativistic ions is determined by the Bohr formula [100]:

$$-\left[\frac{\mathrm{d}E}{\mathrm{d}x}\right]_{\rm free} = \left(\frac{Z_{\rm eff} e \omega_{\rm p}}{v}\right)^2 \ln \frac{m v^3}{Z_{\rm eff} e \omega_{\rm p}}\,, \qquad v \gg v_{\rm th} = \sqrt{\frac{k_{\rm B} T}{m}}\,, \tag{21}$$

where T is the plasma temperature, $k_{\rm B}$ is the Boltzmann constant, $Z_{\rm eff}$ is the effective charge of incident ions, and $\omega_{\rm p}$ is the plasma frequency, defined as follows:

$$\omega_{\rm p} = \left(\frac{4\pi N_{\rm e} e^2}{m}\right)^{1/2}. \tag{22}$$

Here, $N_{\rm e}$ is the density of *free* electrons.

In the case of the SP for nonrelativistic ions propagating in a (gas) target, Eqn (14) can be rewritten in a form similar to expressions (21) and (22):

$$-\left[\frac{\mathrm{d}E}{\mathrm{d}x}\right]_{\rm gas} = \left(\frac{Z_{\rm eff} e \omega_{\rm p}}{v}\right)^2 \ln \frac{2 m v^2}{I}\,, \tag{23}$$

where $N_{\rm e}$ now corresponds to the density of the *bound* electrons in gas.

Formulas (21) and (23) differ from each other by the expression under the logarithm sign. This means that even if the effective charges in plasma and gas targets are the same, the SP of free electrons in a plasma is always greater than that in a gas due to the logarithmic term. For a *partially* ionized plasma, the ion energy loss is defined by the sum of expressions (23) for the bound electrons of atoms and ions in a plasma and Eqn (21) for free electrons, where each term has to be multiplied by the corresponding particle density in a plasma.

The presence of *free* electrons in a plasma significantly changes the picture of the *atomic interactions* of the ion beam with the plasma in comparison with a cold gas. In addition to free electrons, the presence of ions in a plasma should be remembered, and the concentrations of all particles depend strongly on plasma temperature and density. Besides the electron loss and capture processes occurring in targets of neutral atoms, interaction with free electrons and plasma ions leads to the appearance of additional atomic processes like radiative recombination (ion capture of free plasma electrons followed by photon emission), dielectronic recombination, triple recombination, and projectile ion ionization by plasma electrons and ions (see Section 5.4).

The rates of radiative recombination of free electrons are much smaller than those of electron capture on bound electrons, which leads to a substantial increase of the effective charge $Z_{\rm eff}$ in a plasma compared to a cold-gas target of the same element. This property, predicted in paper [101], leads to an increase in the SP of a plasma for ions because, in the first approximation, $-\mathrm{d}E/\mathrm{d}x \sim Z_{\rm eff}^2$. Experimental studies of heavy-ion SPs in a hydrogen plasma were carried out in Refs [108–110], where a hydrogen plasma was created in Z-pinch with electron density $N_{\rm e} \sim 10^{16} - 10^{19}\ \mathrm{cm}^{-3}$ and electron temperature $T_{\rm e} = 10-20$ eV. The main conclusion made in these papers is that a plasma constitutes a more effective medium for ion beam deceleration than gas targets.

A comparison of ionization losses in a gas and in a fully ionized plasma is given in Fig. 7a. As was mentioned before, the quantity $\mathrm{d}E/\mathrm{d}x$ for a fully ionized gas is larger than for a cold gas, because of a different logarithmic dependence of the stopping power: in a plasma, free electrons are much easier to excite (plasma waves) than bound electrons in atoms and ions. This conclusion is confirmed by experimental data (see, e.g., Refs [109–112]).

Figure 7b plots experimental data on SPs for Kr ions in a fully ionized hydrogen plasma and in a cold gas as a function of ion energy. It is seen that at low ion energies $E \sim 0.1$ MeV/u, a 200-fold increase in the energy losses is observed in the hydrogen plasma compared to a cold gas.

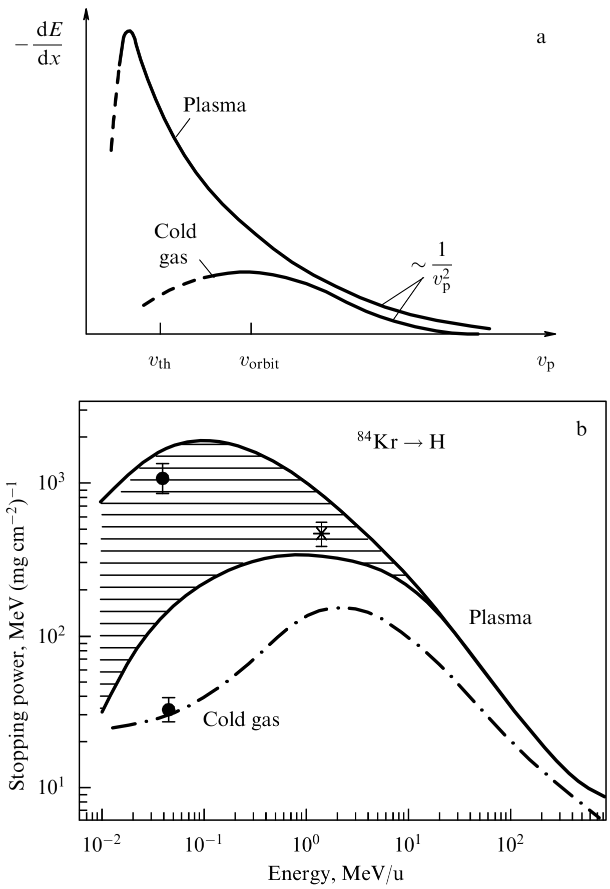

Figure 7. (a) Illustration of SP increase in a plasma compared with a cold gas as a function of ion velocity, assuming that the effective charge is the same for both cases. (Taken from Ref. [50].) (b) Experimental SP values for Kr ions in a fully ionized hydrogen plasma and in a cold gas as a function of ion energy (symbols). Theoretical estimates are represented by solid and dashed–dotted curves. (Taken from Ref. [110].)

At the same time, the difference in SP for a gas and plasma at high ion energies $E > 10$ MeV/u is about a factor of 2.

At present, intensive studies on the slowing-down of heavy ions are being carried out in a carbon laser-produced plasma with high electron densities $N_e \sim 10^{21}$ cm^{-3} and temperatures $T_e = 60-250$ eV (see, for example, Refs [113–116]). Large values of N_e and T_e, as well as the presence of ions with different charges (C^{q+}) in a plasma, make it possible to investigate in more detail the effect of physical processes accompanying an ion beam–plasma interplay, for example, dielectronic recombination, which does not arise in a hydrogen plasma because of the absence of doubly excited atomic states in the hydrogen.

In general, it should be noted that, while the slowing-down of heavy ions in solid and gaseous targets has been studied sufficiently well and many theoretical models adequately reproduce the experimental results, the interaction of charged particles with a plasma has been investigated in less detail, and the number of available experimental data is very limited.

3.6 Influence of the target-density effect on the stopping power

The *target-density* or *gas-solid* effect has been first observed experimentally by Lassen [117, 118] in the study of charge-state fractions of uranium-ion beams passing through a carbon foil and a gas target, and later on, in measuring the energy loss (stopping power) of ions in gas and solid media [119]. The density effect consists in increasing the average (equilibrium) charge of ions when an ion beam passes through a solid body in comparison to a gas target. The first theoretical models taking account of the influence of the effect on ion fractions and energy losses were presented in papers [120, 121]. With the development of heavy-ion accelerating technology, experimental and theoretical studies of density effects have been continued (see Refs [1, 5, 10, 122–126]. At present, the term *density effects* is understood more broadly, i.e., the influence of the effect on the atomic cross sections, the stopping of ions in a dense medium, the equilibrium charge-state fractions in ion beam passage through gas, plasma, foils, etc.

A qualitative explanation of the density effect is as follows (see also Section 5.3.2). As a target density increases, the frequency of projectile ion collisions with target atoms increases and the time between neighboring collisions becomes shorter than the lifetime of the ion excited states in medium, so that some excited ions experience further collisions with the target particles. The excited ions do not have enough time to decay into lower quantum states by radiative transitions or any other way, which leads to their ionization in subsequent collisions with the target particles.

As a result, with an increase in target density, the electron capture (charge exchange) cross sections decrease, because the number of vacant excited states of the formed ion decreases, and, in contrast, the loss (stripping) cross sections increase, because ionization of the incident ion occurs not only from the ground state, but also from excited states. Since the average ion charge is formed as a result of establishing the steady equilibrium between the processes of ionization and recombination, the combined influence of the density effect on both processes leads to an *increase in the average ion charge* in a denser medium, and, consequently, to an increase in the stopping power. A quantitative description of the influence of the density effect on the average charge of many-electron ions passing through gas and solid targets is given in paper [126] in terms of the electron-loss and electron-capture cross sections, which effectively depend on the target density, the relative collision energy, and the atomic structure of the colliding particles.

One of the first experiments focused on studying the SP for heavy many-electron ions with account for the density effect was performed at the UNILAC/GSI accelerator in Darmstadt, where partially ionized ions from Kr to U were studied at energies of several MeV/u, and it was shown that the SPs in gases are approximately 20% less than those in foils [124]. These results are presented in Fig. 8.

4. Equations of charge state balance

4.1 Charge-state balance equations in the passage of ions through matter. Average charge state and equilibrium thickness

One of the key questions arising in the passage of ion beams through gas, plasma, or solid targets is information on the evolution of the ion charge states as a function of the penetration depth (target thickness), i.e., charge-state *fractions* F_q with a relative number of ions having a given charge q. Determination of the ion fractions F_q plays an important

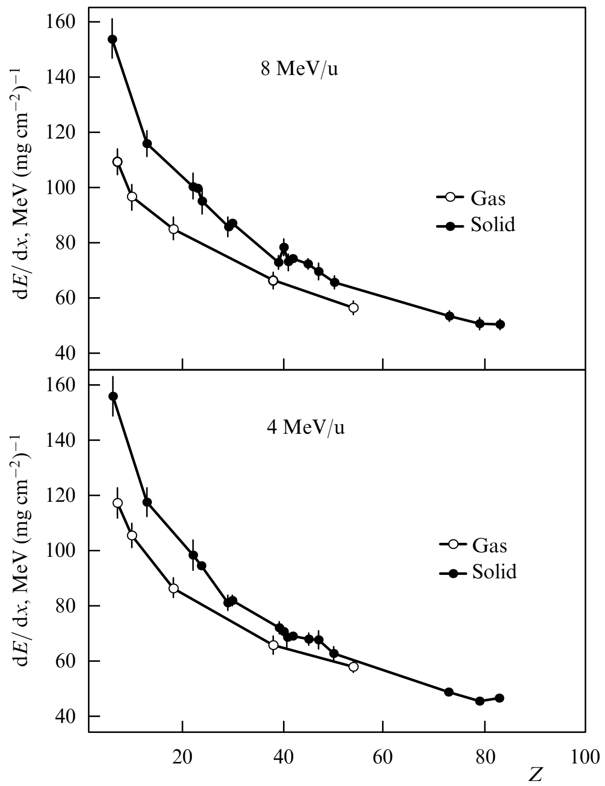

Figure 8. Experimental stopping powers for uranium ions in gases (circles) and solids (black dots) at energies of 8 and 4 MeV/u as functions of the target atomic number Z. (Taken from Ref. [69].)

role in solving many experimental and theoretical problems in atomic and nuclear physics, plasma physics, accelerator physics, and so on. For example, the effective cross sections of electron-loss and electron-capture processes, as a rule, are found from measured F_q values [1].

With increasing target thickness x, the charge-state fractions $F_q(x)$ change greatly due to the influence of competing ionization (electron loss) and recombination (electron capture) processes, i.e., charge-changing processes. The dependence of the $F_q(x)$ fractions on the target thickness x is found by solving the *balance* (rate) equations (first-order differential equations), which relate $F_q(x)$ fractions with the cross sections of projectile ion interactions with media particles [1]. In the case of gas/foil targets, the balance equations have the form

$$\frac{\mathrm{d}}{\mathrm{d}x}\,F_q(x) = \sum_{q'\neq q} F_{q'}(x)\sigma_{q'q} - F_q(x)\sum_{q'\neq q}\sigma_{qq'}\,, \tag{24}$$

$$\sum_q F_q(x) = 1\,, \qquad x = NL\,, \tag{25}$$

where x is the target thickness or the *areal* density. The sum over q means the summation of cross sections over all possible charge states: σ_{ij} for $i<j$ are the single- and multiple-electron loss (projectile ionization by target atoms), and σ_{ij} for $i>j$ are electron-capture (charge exchange) cross sections, respectively, in cm^2/atom or cm^2/molecule units (see Section 5 for interaction processes). Here, N is the target density in atom/cm^3 or molecule/cm^3 units, and L is the penetration depth of ions in the target or *effective length* in cm. The areal density x has the dimension of atom/cm^2 or molecule/cm^2. It is assumed that in system (24), (25) cross sections σ_{ij} do not change with varying parameter x (i.e., the change in the ion velocity v in ion passage through a layer of thickness x can be disregarded). The sum of all fractions is normalized to unity as a consequence of the conservation law for the number of ions before and after collisions with matter.

When the ion beam interacts with the *plasma* target, system of equations (24), (25) is solved using the *rate constants* $Nv\sigma$ of the processes instead of the cross sections (N is the plasma particle density) and taking into account the additional interaction processes of an ion beam with plasma free electrons and ions: radiative and dielectronic recombinations, ionization by electron impact, etc., which are absent in the case of gaseous and solid targets (about the interaction of ions with a plasma, see, for example, Refs [46, 50, 52, 88, 116]).

Equations (24), (25) with the left-hand sides $\mathrm{d}F_q(x)/\mathrm{d}x \neq 0$ have an *analytical* solution, if the number of fractions equals 2 or 3 [127]. Analytical expressions given in review [127] for $F_q(x)$ fractions are used to solve various problems for ion beams passing through a medium at relativistic energies, when the three main fractions (bare nuclei, H- and He-like ions) make a major contribution. In general, the system of equation is solved numerically, for example, by the Runge–Kutta method or by the diagonalization method for the interaction matrix (see Section 6).

In practice, the target thickness x is often expressed in g cm^{-2} units of areal density, using the relationships

$$x\ [\mathrm{atom/cm^2}] = N\ [\mathrm{atom/cm^3}]\ L\ [\mathrm{cm}] = x\ [\mathrm{g\ cm^{-2}}]\ \frac{N_\mathrm{A}}{M}\,, \tag{26}$$

where $N_\mathrm{A} = 6.022\times10^{23}$ is the Avogadro constant, and M is the atomic mass of the particles (atoms or molecules) of the medium in a.m.u.

Ion charge-state fractions in a medium possess an important property: at a certain target thickness x_eq, they reach their *equilibrium stage*, i.e., become stationary, independent of the target thickness upon its further increasing, $x > x_\mathrm{eq}$. The quantity x_eq is termed the *equilibrium thickness*, and the corresponding fractions $F_q(\infty)$ are called *equilibrium fractions*. The equilibrium thickness depends on the interaction cross sections entering into system (24), (25), and, in general, on the charge q_0 of the incident ions [10].

Figure 9 illustrates the evolution of bromine ion fractions in the collision of Br^{10+} ions with argon atoms at an energy of 13.9 MeV (174 keV/u) as a function of argon density. As is seen from the figure, for a thickness $x_\mathrm{eq}\approx 3\times10^{16}$ atom/cm^2, all ion fractions reach their equilibrium stage, i.e., become independent of the thickness x upon its further increasing. Strictly speaking, each fraction reaches its own equilibrium value at its specific thickness. The equilibrium thickness is referred to the target thickness, at which *all* fractions reach their equilibrium states.

The *mean* ion charge $\bar{q}$ in a medium at a thickness of x is identified as

$$q(x) = \sum_q qF_q(x)\,, \qquad \sum_q F_q(x) = 1\,. \tag{27}$$

The *equilibrium* average charge is defined by the formula

$$\bar{q} = q(\infty) = \sum_q qF_q(\infty)\,, \tag{28}$$

where $q(\infty)$ and $F_q(\infty)$ correspond to the equilibrium values.

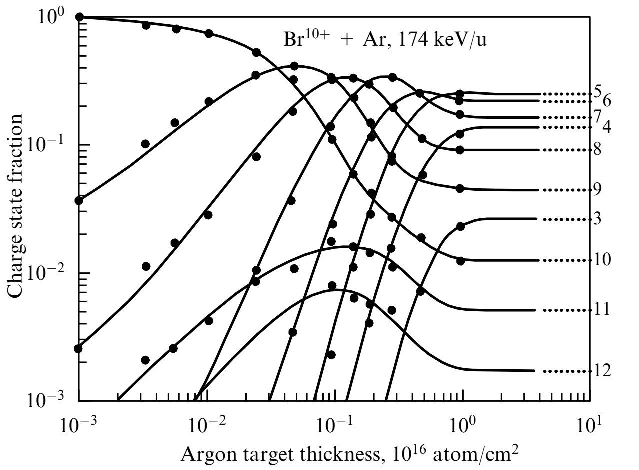

Figure 9. Evolution of bromine ion fractions in collisions of Br^{10+} ions with argon atoms at 13.9 MeV (174 keV/u) as a function of argon density. Symbols — experimental data, solid curves — calculations taking into account the contribution from multielectron loss cross sections. (Taken from Ref. [128].)

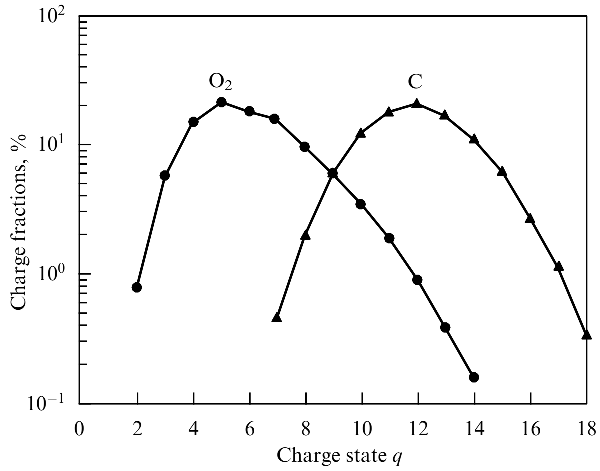

Figure 11. Distributions of experimental equilibrium fractions $F_q(\infty)$ (8) (%) of iodine ions I^{q+} upon collision with molecular oxygen and carbon foils as a function of charge state q at 12 MeV (94.5 keV/u). The equilibrium average charges are, respectively: $\bar{q}(O_2) \approx 5$ and $\bar{q}(C) \approx 12$. (Taken from Ref. [121].)

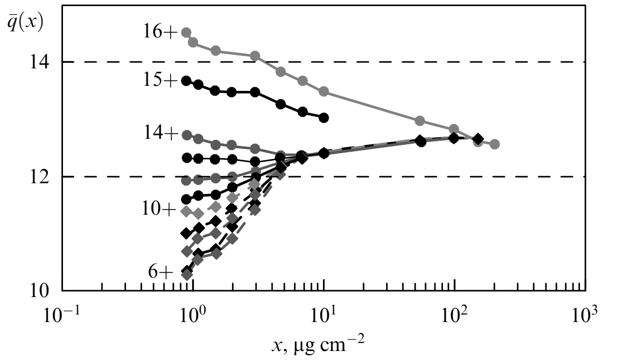

Figure 10. Dependence of the average charge $\bar{q}(x)$ on target thickness x in the collisions of 2 MeV/u-S^{q+} ions, $q = 6-16$, possessing equilibrium charge $\bar{q} = 12.68$ with a carbon foil. (Taken from Ref. [129].)

The maximum value $\bar{q}_{\max}(x)$ is reached in the equilibrium regime, i.e., when all fractions $F_q(x) \equiv F_q(\infty)$. Figure 10 plots experimental dependence of the mean charge $\bar{q}(x)$ on the target thickness x in the collisions of 2 MeV/u-Si^{q+} ions, $6 \leqslant q \leqslant 16$, with a carbon foil. For ions with initial charges $q_0 = 14-16$ and small values of x, the mean charge is greater than the equilibrium one: $\bar{q}(x) > \bar{q} = 12.68$. For all incoming ions with an initial charge of $6 \leqslant q_0 \leqslant 13$, the equilibrium charge $\bar{q} = 12.68$ is the maximum charge of the ion beam at the exit from the foil.

4.2 Equilibrium ion fractions and charges

Equilibrium fractions correspond to the solution of the system (24), (25) at $dF_q/dx = 0$, which is transformed into a system of linear algebraic equations

$$0 = \sum_{q' \neq q} F_{q'}(\infty)\sigma_{q'q} - F_q(\infty)\sum_{q' \neq q}\sigma_{qq'} \,, \qquad \sum_q F_q(\infty) = 1 \,, \tag{29}$$

and the equilibrium average charge is determined by formula (28).

System of equations (29) has a simple analytical solution, if the contribution of multiple-electron processes is ignored and only single-electron cross sections with $|q - q'| = 1$ are allowed for. In this case, the equilibrium fractions are determined from simple formulas through the ratios of single-electron loss-to-capture cross sections [1]. Thus, in the 4-fraction approximation, the solution assumes the form

$$\begin{aligned}
F_1(\infty) &= \left[1 + \frac{\sigma_{12}}{\sigma_{21}}\left(1 + \frac{\sigma_{23}}{\sigma_{32}}\left(1 + \frac{\sigma_{34}}{\sigma_{43}}\right)\right)\right]^{-1} , \\
F_2(\infty) &= F_1(\infty)\,\frac{\sigma_{12}}{\sigma_{21}} \,, \\
F_3(\infty) &= F_2(\infty)\,\frac{\sigma_{23}}{\sigma_{32}} \,, \\
F_4(\infty) &= 1 - \left[F_1(\infty) + F_2(\infty) + F_3(\infty)\right] ,
\end{aligned} \tag{30}$$

where σ_{12}, σ_{23}, and σ_{34} are single-electron loss (stripping) cross sections for ion transitions $q \to q+1$, and σ_{21}, σ_{32}, and σ_{43} are single-electron capture (charge-exchange) ones for ion transitions $q+1 \to q$. Equations (30) can easily be generalized to the case of an arbitrary number of charge-state fractions, if only single-electron cross sections are accounted for.

Figure 11 shows experimental distributions of equilibrium fractions in collisions of iodine ions with oxygen molecules and graphite foils at an energy of 12 MeV (94.5 keV/u). The shift in the distribution to the right in the case of a graphite foil is related to the target-density effect (see Section 5.3.2).

The equilibrium fractions $F_q(\infty)$ depend on cross sections of ion–target particle scattering but not on the initial charge q_0 of incident ions. This circumstance follows from experimental data (see, e.g., paper [129]) and theory [10], and has a wide application, for example, for detecting superheavy chemical elements (see Refs [130, 131] and Section 7.1).

In the case of beams of heavy many-electron ions, a large number of fractions are formed, the distribution of which over the charge state q covers quite a broad spectrum. For a few-electron projectiles, this distribution has a narrower profile, i.e., when only a few fractions dominate, as it takes place in relativistic ion–atom collisions.

The distribution of equilibrium fractions $F_q(\infty)$ over charge states q is usually described by a Gaussian distribution with the following parameters:
distribution width d is given by

$$d = \left[\sum_q (q - \bar{q})^2 F_q(\infty) \right]^{1/2}, \tag{31}$$

and asymmetry parameter s (skewness) is defined as

$$s = \sum_q \frac{(q - \bar{q})^3 F_q(\infty)}{d^3}. \tag{32}$$

In practice, the equilibrium average charge is found not from quite complicated system (24), (25), but from the intersection of the q-dependences of the projectile ionization (loss) and recombination (charge-exchange) cross sections, i.e., from the equality

$$\sigma_{\text{ion}}(\bar{q}) = \sigma_{\text{rec}}(\bar{q}). \tag{33}$$

This method gives a rougher estimate of the equilibrium average charge $\bar{q}$ than formula (28), but is simpler and clearer. In this case, the values calculated from formulas (28) and (33) can differ by 15–20% or more from each other (see, e.g., Refs [132, 133]).

4.3 Equilibrium average charge

There are several semiclassical and semiempirical formulas for estimating the equilibrium average charge. These formulas are rather simple and give an estimate of the desired quantities, but have a number of serious disadvantages: they do not take into account the atomic structure of the colliding particles or the target-density effect (see Section 5.3.2). However, these formulas are very useful in many cases and applications.

The first semiclassical formulas for the equilibrium average charge were obtained independently in the work of Bohr [134, 135] and Lamb [136] (for more details, see review [1]). The Bohr formula was obtained for *rarefied gas* targets on the assumption that the incident ion loses all electrons whose orbital velocity is greater than the ion velocity. The formula has the form

$$\bar{q} = v Z_{\text{N}}^{1/3}, \quad 1 < v < Z_{\text{N}}^{2/3}, \tag{34}$$

where Z_{N} is the incident ion *nuclear* charge. According to Eqn (34), a complete stripping of the incident ions to bare nuclei occurs at ion velocity $v \sim Z_{\text{N}}^{2/3}$. Formula (34), derived from simple physical considerations, is still used as the basic formula for ion transportation problems through media (see, for example, the problem of detecting superheavy elements in Section 7.1).

The formula reported by Betz et al. [137] was made up on the basis of experimental data for ions with a nuclear charge $Z_{\text{N}} > 10$ and energies $5 < E < 80$ MeV in *gaseous* and *solid* targets and has the form

$$\bar{q} = Z_{\text{N}} \left[1 - C \exp\left(-v Z_{\text{N}}^{-\gamma}\right) \right], \quad v > 1, \tag{35}$$

where the approximation parameters are $C \approx 1$, and $\gamma \approx 2/3$. If $v Z_{\text{N}}^{-2/3} \ll 1$, formula (35) coincides with the Bohr formula (34).

The Nikolaev and Dmitriev formula [138] was constructed using experimental data for heavy many-electron ions passing with energies $E > 100$ MeV through *solid* targets and has the form

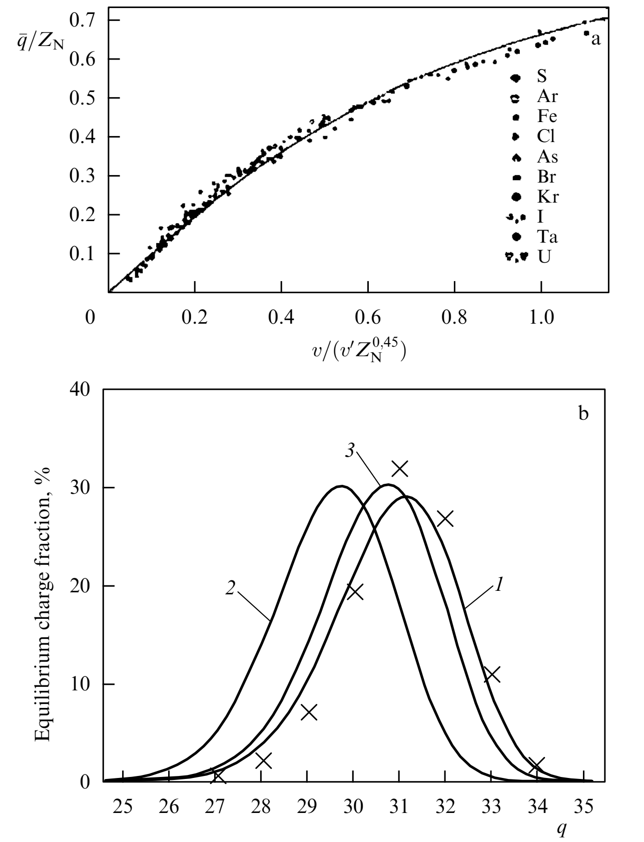

Figure 12. (a) Equilibrium average charge $\bar{q}/Z_{\text{N}}$ of ions for a carbon foil (dark symbols, experiment) and for foils of other elements (light symbols, experiment) as a function of the reduced ion velocity $v/(v' Z_{\text{N}}^{0.45})$, $v' = 3.6 \times 10^8$ cm s^{-1}. The solid curve is plotted using the Nikolaev–Dmitriev formula (36). (Taken from Ref. [1].) (b) Experimental equilibrium fractions of krypton ions (X's) in the collisions of 6.0 MeV/u-Kr^{13+} ions with a carbon foil as a function of ion charge in comparison with various semiempirical formulas: *1* — [139], *2* — [140], and *3* — [141]. (Taken from Ref. [142].)

$$\bar{q} = Z_{\text{N}} \left[1 + \left(\frac{0.608\, v}{Z_{\text{N}}^{a}} \right)^{-1/k} \right]^{-k}, \tag{36}$$

where the approximation parameters $a = 0.45$, and $k = 0.6$. A comparison of the average charge calculated by the Nikolaev–Dmitriev formula with experimental data for carbon foils and other elements is given in Fig. 12a.

The dependence of the average charge $\bar{q}/Z_{\text{N}}$ on the relative ion velocity $v/Z_{\text{N}}^{0.55}$ [1], obtained from experimental data for *gaseous* targets, is similar to the result calculated with formula (36), but the parameter k was not determined because of the scatter of the experimental data due to the different gas densities, i.e., because of the density effect, which is not accounted for in any of the known formulas for the equilibrium average charge.

For carbon foils, the formula by Shima et al. [139] is often used:

$$\begin{gathered} \bar{q} = Z_{\text{N}} \left[1 - \exp\left(-1.25x + 0.32x^2 - 0.11x^3\right) \right], \\ x = 0.608\, v Z_{\text{N}}^{-0.45}, \quad x < 2.4, \end{gathered} \tag{37}$$

where Z_{N} is the projectile nuclear charge.

In paper [140], empirical formulas for equilibrium ion charges were obtained for gaseous targets:

$$\bar{q}_{\text{gas}} = Z_{\text{N}} \frac{376x + x^6}{1428 - 1206x^{0.5} + 690x + x^6}\,,$$
$$x = \left(\frac{\eta}{Z^{0.017\eta - 0.03}}\right)^{1+0.4/Z_{\text{N}}}, \quad \eta = vZ_{\text{N}}^{-0.52}\,, \tag{38}$$

and solid targets:

$$\bar{q}_{\text{solid}} = Z_{\text{N}} \frac{12x + x^4}{0.07/x + 6 + 0.3x^{0.5} + 10.37x + x^4}\,,$$
$$x = \left(\frac{\eta}{Z^{0.019\eta}}\right)^{1+1.8/Z_{\text{N}}}, \quad \eta = vZ_{\text{N}}^{-0.52}\,, \tag{39}$$

where Z is the *target* atomic number. As is seen from Eqns (38) and (39), the equilibrium charges at low ion velocities do not decrease exponentially but by a power law:

$$\bar{q}_{\text{gas}} \sim v^{1+0.4/Z_{\text{N}}}\,, \quad \bar{q}_{\text{solid}} \sim v^{1+1.8/Z_{\text{N}}}\,. \tag{40}$$

Figure 12b shows experimental equilibrium fractions of krypton ions (marked by crosses) in the collisions of 6.0- MeV/u Kr^{13+} ions with a carbon foil as a function of ion charge in comparison with results calculated using different semiempirical formulas. The best agreement with experiment is achieved with the Shima formula (37).

5. Cross sections of heavy ion interactions with gaseous, solid, and plasma targets

This section briefly describes the processes of ion interactions with *gaseous*, *solid*, and *plasma* targets, accompanied by a change in the charge state of the incident ions, as well as the ionization of neutral *target atoms* by multiply charged ions. The probabilities (effective cross sections) of these processes play a major role in the formation of ionic fractions, average charge, stopping power, and other characteristics of ion interactions with various media (see, e.g., review [26]).

Ionization and capture processes proceeding in ion–atom collisions are described by the general reaction called *transfer ionization*, in which simultaneous capture and ionization occur with the participation of electrons from both colliding particles:

$$X^{q+} + A \rightarrow X^{q'+} + A^{m+} + (q' - q + m)\text{e}^-\,, \tag{41}$$

where q and q' are the charges of the X^{q+} ion before and after collision, respectively, and m is the charge of the target ion A^{m+} after collision.

The following atomic processes are distinguished:

(1) *multiple-electron* ionization of an incident ion or stripping (*loss* or *projectile ionization*):

$$X^{q+} + A \rightarrow X^{(q+m)+} + A + m\text{e}^-\,, \quad m \geqslant 1\,; \tag{42}$$

(2) *multiple-electron* capture (*charge exchange* or *electron transfer*):

$$X^{q+} + A \rightarrow X^{(q-k)+} + A^{k+}\,, \quad k \geqslant 1\,; \tag{43}$$

(3) *multiple-electron* ionization of the target atom (*target ionization*), in which the projectile charge does not change:

$$X^{q+} + A \rightarrow X^{q+} + A^{m+} + m\text{e}^-\,, \quad m \geqslant 1\,. \tag{44}$$

At nonrelativistic ion energies, collision processes (41)–(44) are of a multiple-electron nature, i.e., are accompanied by multiple-electron transfers, which is confirmed experimentally. For heavy ions (such as Xe^{q+}, Pb^{q+}, W^{q+}, U^{q+}), multiple-electron processes contribute significantly (50% or more) to the total cross sections, summed over all m, and therefore should be taken into account together with single-electron processes. With ion energy increasing, the contribution from multiple-electron processes decreases, and single-electron processes play a major role.

For relativistic energies $E > 200$ MeV/u, in addition to the single-electron *nonradiative capture* (NRC), process (43), *radiative single-electron capture* (REC) with a subsequent photon emission becomes important:

$$X^{q+} + A \rightarrow X^{(q-1)+} + A^+ + \hbar\omega_{\text{REC}}\,. \tag{45}$$

Process (45) is similar to radiative (photo)recombination, but in contrast electron capture occurs on the bound, not free, electrons of the target atoms. At relativistic energies, the total electron-capture cross section is given by the sum

$$\sigma_{\text{EC}}^{\text{tot}} = \sigma_{\text{NRC}} + \sigma_{\text{REC}}\,, \tag{46}$$

and the contribution of both capture processes can be of the same order, especially in the case of heavy targets such as Ar, Kr, and Xe (for more details about charge-exchange cross sections and other processes, see reviews [26, 143]).

At large (but nonrelativistic) ion energies E, the single-electron capture cross sections for NRC, REC, and EL (electron loss) processes have the following asymptotic behavior:

$$\sigma_{\text{NRC}} \sim \frac{q^5 Z^5}{E^a}\,, \quad 1 \leqslant a \leqslant 5.5\,, \quad v^2 \gg I_{\text{T}}\,, \tag{47}$$

$$\sigma_{\text{REC}} \sim \frac{q^5 Z}{E^a}\,, \quad 1 \leqslant a \leqslant 2\,, \quad v^2 \gg I_{\text{T}}\,, \tag{48}$$

$$\sigma_{\text{EL}} \sim \frac{Z^2}{q^2} \frac{\ln E}{E}\,, \quad v^2 \gg I_{\text{P}}\,, \tag{49}$$

where I_{P} and I_{T} are the binding energies of the incident ion and the target atom, respectively, v is the ion velocity, Z is the target atomic number, which for neutrals coincides with the number of electrons, and the power a depends on the structure of the electronic shells of the colliding particles. At high energies, as follows from Eqns (47) and (48), the total electron-capture cross section, given by the sum (46), increases with the number of target electrons.

At present, considerable material has been accumulated on the experimental and theoretical cross sections for electron loss and capture processes. At relatively low ion energies $E \lesssim 1$ keV/u, experimental data on cross sections of singly charged ions are given in tables [144, 145], and for $E > 1$ MeV/u, the data for multiply charged ions were obtained mainly at the Helmholtz Centre for Heavy Ion Research (GSI), Darmstadt [146–151], Texas synchrotron [152–154], Princeton Tokamak [155], BEVALAC accelerator, Berkeley [156], and the Nishina Center's heavy-ion accelerators (RIKEN), Japan [157–159]. More detailed information about electron loss and capture cross sections of heavy ions can be found in books and review papers [13, 20, 23–26, 160–162].

A typical example of charge-changing cross section behavior is given in Fig. 13a for collisions of U^{42+} ions with

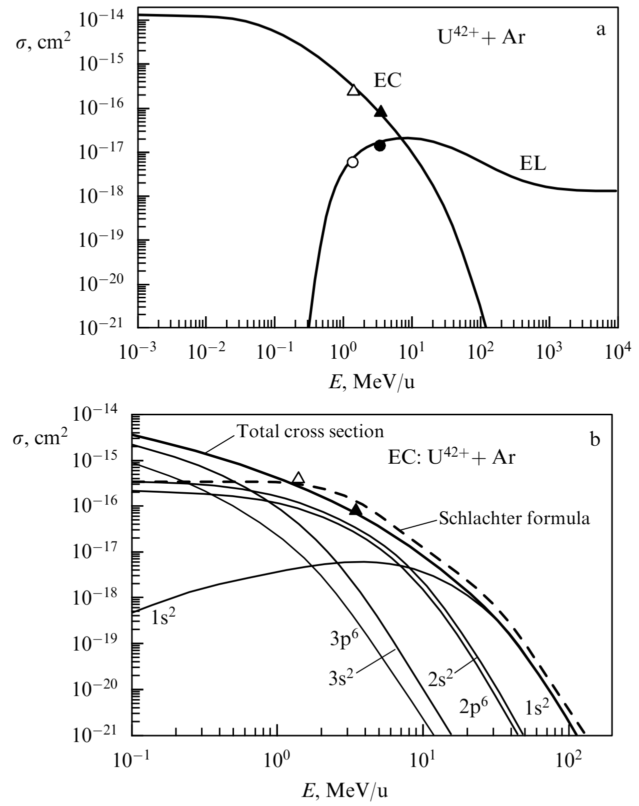

Figure 13. (a) Total cross sections of radiationless capture (EC) and loss (EL) processes in collisions of U^{42+} ions with argon atoms as a function of ion energy. Experiment: light and dark symbols — from Refs [146] and [154], respectively. Theory: solid curves — calculation by the CAPTURE (EC), DEPOSIT, and RICODE (EL) programs. (Taken from Ref. [163].) (b) Single-electron capture cross sections of U^{42+} ions on argon atoms as a function of ion energy. Experiment: light and dark symbols — from Refs [146] and [154], respectively. Theory: solid curves — calculation by the CAPTURE programs, dashed curve — semiempirical Schlachter formula (52) (see text). Contributions of the capture of all argon electrons from $1s^2$, $2s^2$, ..., $3p^6$ shells to the total capture cross section (total — calculations using the CAPTURE program). A detailed description of the CAPTURE, DEPOSIT, and RICODE programs is given in review [26]. (Taken from Ref. [164].)

argon atoms. For energies $E > 1$ keV/u, NRC plays a major role as a recombination process, which prevails up to energies $E \sim 1$ MeV/u. At the energy $E \sim 10$ MeV/u, the electron loss (EL) cross section reaches a maximum, which is also formed due to multiple-electron ionization. With a further energy growth, the EL cross section takes on a constant value, and EL becomes the main charge-changing process.

Figure 13b displays electron-capture cross sections as a function of energy E for the same case of U^{42+} ions colliding with argon atoms, but indicating the contribution from capture of argon inner-shell electrons to the total cross section (see below).

5.1 Electron capture processes

5.1.1 Basic properties of single-electron capture. Electron capture is one of the main processes occurring in the penetration of ion beams through gaseous, plasma, and solid targets, especially when the beam consists only of bare nuclei. In this section, we briefly discuss the main properties of single- and multiple-electron capture processes (43).

At moderate ion energies $E \sim 1-25$ keV/u, a capture of mainly one of the target outer-shell electrons takes place, and because of the contribution from a large number of excited states of the resulting $X^{(q-1)+}$ ion, the electron capture cross section features a *quasiconstant* character, i.e., shows a week dependence on the energy E. This behavior was predicted in paper [165], and the cross-section magnitude, close to experimental data, is estimated from the electron tunneling model through a Coulomb potential barrier created by the target atom and the incident ion [166]:

$$\sigma(v)\left[\frac{\text{cm}^2}{\text{atom}}\right] \approx 10^{-15}\,\frac{q}{(I_{\rm T}/\text{Ry})^{3/2}}\,, \quad q \geqslant 5\,, \quad v^2 < I_{\rm T}\,, \qquad (50)$$

where $I_{\rm T}$ is the ionization potential of the target atom, 1 Ry = 13.606 eV. According to this model, at moderate ion energies, electron capture occurs predominantly to the levels of the ion $X^{(q-1)+}(n)$ with the principal quantum numbers n estimated as follows:

$$n \approx \frac{q^{3/4}}{(I_{\rm T}/\text{Ry})^{1/2}}\,. \qquad (51)$$

The cross section in formula (50) is given in cm^2/atom, i.e., refers to one atom: when calculating cross sections for *molecular* targets, *Bragg's additivity rule* is applied (see Ref. [167]), according to which effective interaction cross sections (electron capture, loss) for a molecule target are given by the sum of the cross sections for its constituent atoms. For example, in the case of electron capture on a CO_2 molecule, one has $\sigma(CO_2)$ [cm^2/molecule] $= 2\sigma(\text{O})$ [cm^2/atom] $+$ $\sigma(\text{C})$ [cm^2/atom]. The use of Bragg's rule is associated with difficulties in calculating the cross sections for molecular targets, but it is partially justified by the fact that, at sufficiently high collision energies, the main contribution to the cross sections is made by the capture of target inner-shell electrons, whose structure in atoms and molecules is approximately the same.

At higher ion energies, $E \approx 25$ keV/u–30 MeV/u, the electron-shell structure of the target atom becomes significant due to the predominant capture of target *inner-shell* electrons, and this constitutes the main property of electron-capture reactions, distinguishing them from other processes in collisions of *fast* ions with atoms.

With ion energy increasing, the electron capture cross section from *one* fixed target shell decreases rapidly as $\sim E^{-5.5}$, in contrast to the ionization and excitation cross sections ($\sim E^{-1}$), and the capture of target *inner-shell* electrons with an orbital velocity $v_{\rm e}$, close to the incident ion velocity, $v_{\rm e} \sim v$, begins to play a role. This is the so-called *velocity matching* condition, when the electron capture cross section is close to its maximum value. The orbital electron velocity $v_{\rm e}$ of deeper target shells increases due to their binding energy increasing; therefore, with ion velocity v increasing, the target inner-shell electrons are captured with a higher probability, for which the velocity matching condition is satisfied, but the contribution from the target outer-shell electrons becomes small due to a rapid decrease in the cross section with increasing collision velocity. As a result, the electron capture cross section, summed over all target shells, decreases by a slower law than $E^{-5.5}$. The latter is realized only in the region of very high energies, where the main contribution is made by the capture of 1s electrons of the target atoms. For this reason, the electron capture cross sections for light targets (H, He) decrease much faster than in the case of heavy targets (Ne, Ar, Kr, Xe), which have a larger number of electron shells.

The predominant capture of the target inner-shell electrons with increasing ion energy is demonstrated in Fig. 13b for collisions of U^{42+} ions with Ar, having the electron configuration $1s^2 2s^2 2p^6 3s^2 3p^6$. First, the capture of $3s^2$ and $3p^6$ electrons of an argon atom occurs, then of $2s^2$ and $2p^6$ shells, and only at energies $E > 10$ MeV/u does the capture of $1s^2$ electrons make the main contribution and the cross section decrease according to the law $\sim E^{-5.5}$.

At present, there are several methods and corresponding computer programs to calculate electron-capture cross sections for heavy *many-electron* ions hitting target atoms: a classical-trajectory Monte Carlo method (CTMC) for ion energies $E > 1$ MeV/u [168], the method of continuum distorted waves (CDW) [169, 170] for $E > 10$ MeV/u, the eikonal method for $E > 1$ MeV/u) [171], and the normalized Brinkman-Kramers approximation (CAPTURE program) for $E > 10$ keV/u [172]. The accuracy of calculating electron-capture cross sections by these methods is within a factor of 2. A detailed description of these methods can be found in review [26].

To estimate *single-electron* capture cross sections, a semiempirical Schlachter formula [173] is often used, which was obtained from experimental data in the form

$$\sigma_{\rm Sch}\left[\frac{\rm cm^2}{\rm atom}\right] = \frac{1.1\times10^{-8}}{\tilde{E}^{4.8}}\frac{q^{0.5}}{Z^{1.8}}\left[1-\exp\left(-0.037\tilde{E}^{2.2}\right)\right] \times\left[1-\exp\left(-2.44\times10^{-5}\tilde{E}^{2.6}\right)\right], \qquad (52)$$

$$\tilde{E} = \frac{E}{Z^{1.25}q^{0.7}}, \quad q \geqslant 3, \quad \tilde{E} \geqslant 10, \qquad (53)$$

where Z is the target atomic number, and E is the ion energy in keV/u. Equations (52) and (53) reflect the *scaling* law of the electron capture cross sections on energy, ion charge, and target nuclear charge, and are widely used to estimate the cross sections to within a factor of 2. For collisions of U^{42+} ions with argon atoms, the cross section calculated from Eqn (52) is also depicted in Fig. 13b.

5.1.2 Multiple-electron capture. Electron-capture (and loss) processes involving heavy ions are characterized by a high probability of multiple-electron capture, which significantly contributes to the total capture cross sections. The contribution depends on the ion energy and the atomic structure of the colliding particles. Table 1 shows the experimental cross sections of single-electron and total capture cross sections for collisions of uranium ions with argon at an energy of 3.5 MeV/u. When the ion charge increases, the contribution of multiple-electron capture increases up to 40%.

Table 1. Experimental electron capture cross sections for collisions of 3.5 MeV/u-U^{q+} ions, $q = 28-51$, with Ar atoms. $\sigma_{\rm EC}^{(1)}$ and $\sigma_{\rm EC}^{(\rm tot)}$ are single-electron and total capture cross sections, respectively. (Taken from Ref. [154].)

Ion charge q	$\sigma_{\rm EC}^{(1)}$, 10^{-18} cm^2	$\sigma_{\rm EC}^{(\rm tot)}$, 10^{-18} cm^2
28	12.6	12.6
31	19.7	20.8
33	25.0	27.0
39	52.3	60.7
42	61.6	79.7
51	82.5	130.0

At relatively slow collision energies $E = 0.01$ eV/u–10 keV/u, experimental data on the *multiple-electron* capture of ions on atoms can be found in Refs [173–184]. At higher impact energies $E = 1-10$ MeV/u, electron capture cross sections were measured mainly for heavy Xe, Pb, and U ions colliding with gaseous targets [146, 147, 154, 184].

In conclusion, we have to pay attention to the following problems concerning electron-capture processes:

(1) In most cases, in determining capture cross sections, the number of ions in the final channel is measured, although correct experimental data can be obtained by simultaneously measuring both charges of scattered projectiles and target ions using the *coincidence technique*. However, the data obtained by the coincidence technique is very limited, so a comparison of the calculated cross sections with experimental ones should be made taking this circumstance into account (see paper [185]).

(2) In the case of molecular targets (H_2, N_2, CO_2, etc.), the discrepancy between theory and experiment is associated with, among others, violation of Bragg's additivity rule. This circumstance was pointed out in Refs [186, 187], where it was found that the ratio of the electron capture cross sections of ions on molecules and hydrogen atoms is not equal to 2, $\sigma(H_2)/\sigma(H) \neq 2$, but grows nonmonotonically with an energy increase from about 0.8 to 4.0, i.e., the question of using Bragg's rule for molecular targets requires further consideration.

(3) Finally, the role of *multiple-electron* capture by highly charged heavy ions colliding with target atoms has not been studied in detail so far (see Section 5.1.2). It is only known experimentally that the cross sections of multiple-electron capture increase with increasing ion charge, but their dependences on the energy and atomic structure of the colliding particles requires additional theoretical and experimental studies (see, e.g., [146, 147, 154]).

5.1.3 Charge exchange in slow collisions. Isotope effect. The processes arising in slow ion–atom collisions (relative particle velocity $v \ll 1$ a.u.) play an important role in various applications of plasma physics and controlled thermonuclear fusion, as well as in astrophysics. For example, the charge-exchange processes in a low-temperature tokamak plasma (near-wall plasma, plasma in a divertor) provide practically the unique mechanism for producing impurity heavy ions in excited states, the radiative decay of which leads to short-wave emission used for plasma diagnostics.

The processes of charge exchange of ions on hydrogen isotopes (H, D, and T) at low collision energies are also characterized by the presence of the so-called *isotope effect* revealing itself in a large difference (by several orders of magnitude!) in the cross sections: the heavier the isotope, the larger the cross section (see, for example, paper [188]), i.e., a heavier target can reach a region of strong rotational interaction at lower collision energies. The significant difference in the cross sections for the reactions with H, D, and T makes it necessary to take into account the isotope effect in modeling near-wall and divertor plasmas in facilities using hydrogen isotopes [20].

A strong isotope effect in the process of charge exchange of alpha particles on hydrogen isotopes, viz.

$$\mathrm{He}^{2+} + A(1\mathrm{s}) \to \mathrm{He}^{+}(n=2) + A^{+}, \quad A = \mathrm{H, D, T}, \qquad (54)$$

was predicted in Ref. [188] using the electron nuclear dynamics (END) method described in work [189]. Later on, this effect was also found for other shells of the incident ion

[190] and other collision systems, in particular, for heavy ions [191–197] using the *adiabatic* approach [198, 199].

For applications, as a rule, theoretical values of the charge exchange cross sections are used; there are practically no experimental data in this energy range. The values of the cross sections greatly depend on the method of describing the internuclear motion, i.e., on the relative motion of two nuclei in the presence of effective interaction between them. In the presence of a strong isotope effect, theoretical results should be sensitive to the trajectory of particles' approaching — that is, to details of internuclear interaction. Nevertheless, this aspect of the dynamics of slow collisions has not yet been fully studied.

In work [191], the presence of *negative* scattering angles was predicted using the END method for reaction (54) at certain collision parameters,, which cannot be explained by a purely repulsive Coulomb interaction

$$V_{\mathrm{C}}(R) = \frac{Z_1 Z_2}{R}\,, \tag{55}$$

where R is the internuclear distance, and Z_1 and Z_2 are the nuclear charges.

An explanation of the existence of negative scattering angles was recently given in Ref. [200], where the internuclear motion is described by the Born–Oppenheimer (BO) potential corresponding to the initial collision channel:

$$V_{\mathrm{BO}}(R) = V_{\mathrm{C}}(R) + E(R) - E_0\,, \tag{56}$$

where $E(R)$ is the electron energy in the field of nuclei fixed in space at a distance R from each other, which for the present system is the eigenvalue of the two-center Coulomb problem [201], and E_0 is the electron energy in the initial state. This potential effectively takes into account the *electron–nuclear* interaction, the inclusion of which allows us to explain the presence of negative scattering angles. The use of the BO potential proves that the exact *ab initio* description of the internuclear motion, required in the END approach adapted in papers [188, 190, 191], in the case of slow collisions can be reproduced within the framework of the BO approximation.

The following atomic parameters correspond to reaction (54): $Z_1 = 2$, $Z_2 = 1$, and $E_0 = -0.5$ a.u. The contribution of the terms for this system is shown in Fig. 14a. It should be noted that, while the Coulomb potential is repulsive ($\mathrm{d}V_{\mathrm{C}}(R)/\mathrm{d}R < 0$) for all R, the BO potential has a shallow minimum at $R \approx 3.9$ a.u. and is attractive ($\mathrm{d}V_{\mathrm{BO}}(R)/\mathrm{d}R > 0$) for larger R, i.e., potentials (55) and (56) describe different trajectories of the motion of the nuclei.

In work [200], the scattering angle for system (54) was calculated at a fixed energy $E = 50$ eV/u, as in work [191], using the BO potential (56). The results of calculations of the scattering angles as a function of the parameter ρE (ρ is the impact parameter) are shown in Fig. 14b by solid (H), dotted (D), and dotted–dashed (T) lines. They are in complete agreement over the entire range of ρE with END results [191]. Thus, the internuclear dynamics predicted in the END approach can be well reproduced using the BO potential (56). The attractive part of this potential, which appears as a result of the inclusion of the electron–nucleus interaction, is responsible for the appearance of negative scattering angles found in Ref. [191].

In paper [200], the adiabatic approach [198, 199] implemented in the ARSENY code [202] was adapted to calculate the cross section (Fig. 14c). Thin and thick lines show the results [200] obtained in the adiabatic approach [198, 199] with the Coulomb and BO internuclear trajectories, respectively. The dark symbols represent the results obtained in the END approach [189] from work [190]. The fine dotted line depicts the results of an adiabatic calculation without rotational coupling (albeit, for all three targets). The light-

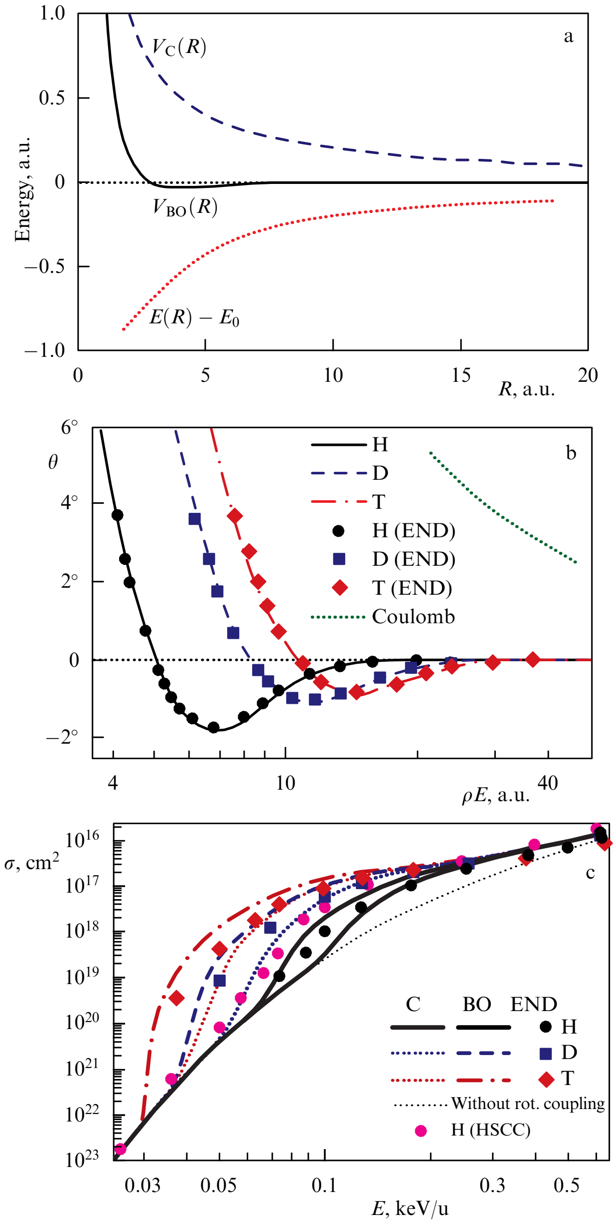

Figure 14. (Color online.) (a) Coulomb (55) and BO (56) internuclear potentials for reaction (54). (b) The scattering angle for internuclear motion in system (54) at a collision energy of 50 eV/n as a function of the product ρE. Solid, dashed, and dotted-dashed lines show the results of calculations [200] for H, D, and T, respectively, using the BO potential (56). The symbols denote *ab initio* END results from Ref. [191]. The dotted line reproduces the results for the Coulomb potential (55) (identical for all three targets). (c) Charge exchange cross sections for reaction (54) with H. Thin and thick lines show the results from Ref. [200] obtained in the adiabatic approach [198, 199] with the Coulomb and BO internuclear trajectories, respectively. The dark symbols represent the results obtained in the END approach [189] from [190]. The fine dotted line shows the results of an adiabatic calculation without rotational coupling (albeit, for all three targets). The light-colored dots mark the results of the hyperspherical calculation using the close-coupling method for the H target [203].

colored dots give the results of the hyperspherical calculation by the close-coupling method (HSCC) for the H target [203].

A completely quantum hyperspherical calculation by the close-coupling method (HSCC) for system (54) with H as the target was performed in Ref. [203]; the results of this calculation are shown by light-colored dots in Fig. 14c. This method solves the quantum three-body Coulomb problem without any approximations, provided that its numerical realization yields convergent results. It is noteworthy that the adiabatic results calculated with the BO trajectory are in better agreement with the HCC results than are the results of the END approach. Assuming that both *ab initio* calculations [190, 203] converge numerically, this means that the adiabatic approximation partially compensates for errors associated with the classical description of internuclear motion.

5.1.4 Charge exchange as a mechanism for creating an inverse medium in the plasma of a capillary discharge. In this section, we illustrate the importance of the ion–ion charge exchange process at low collision energies to create an inverse medium in the plasma of a capillary discharge with a subsequent emission in the soft X-ray range.

Recently, the generation on Balmer-α lines (transition $n = 3 \to n = 2$) in hydrogen-like carbon and oxygen ions was obtained in the ablative capillary discharge in the soft X-ray range [204, 205] at wavelengths of 18.22 nm (C^{5+}) and 10.24 nm (O^{7+}), respectively. The results were obtained at Ruhr University of Bochum (Germany) with the facility described in Ref. [206].

Studies on the creation of inverse population in the soft X-ray region have been carried out since 1985 at Livermore and Princeton laboratories using powerful lasers and heavy targets [207, 208]. At present, this problem is the subject of intensive research in many laboratories around the world (see, e.g., Refs [209, 210]).

Studies [204, 205] are notable for the fact that laser generation in the X-ray range was obtained on a compact (so-called table-top) laboratory installation using light ions. It should be noted that the first investigations on the creation of population inversion in capillary discharges were performed in works [211, 212].

It was concluded [204, 205] that the inversion of the $n = 3$ level in H-like carbon and oxygen ions is achieved as a result of ion–ion charge-exchange reactions

$$C^{6+} + C^{2+}(2s2p) \to \left[C^{5+}(n=3)\right]^* + C^{3+}\,, \tag{57}$$

$$O^{8+} + O^{3+}(2s^2\,2p\,^2P) \to \left[O^{7+}(n=3)\right]^* + O^{4+} \tag{58}$$

in the regime of hose instability of a plasma formed in a low-inductance ablative discharge in a capillary made of polyacetal $(CH_2O)_n$. In the constrictions, a hot plasma of fully ionized C (or O) atoms is formed, which are directed to colder regions where, by recharging on less-charged ions, they create an inverse population by selective charge exchange to the level $n = 3$. Thus, a series of thin plasma disks with an inverse population along the capillary axis is formed, which leads to enhancing the spontaneous emission on the Balmer-alpha line.

The assumption that the observed lasing in C and O ions is due to charge exchange was confirmed by experiments on collision processes in a laser plasma and by calculations of the charge exchange cross sections and populations of excited levels in the collisional–radiative model [213].

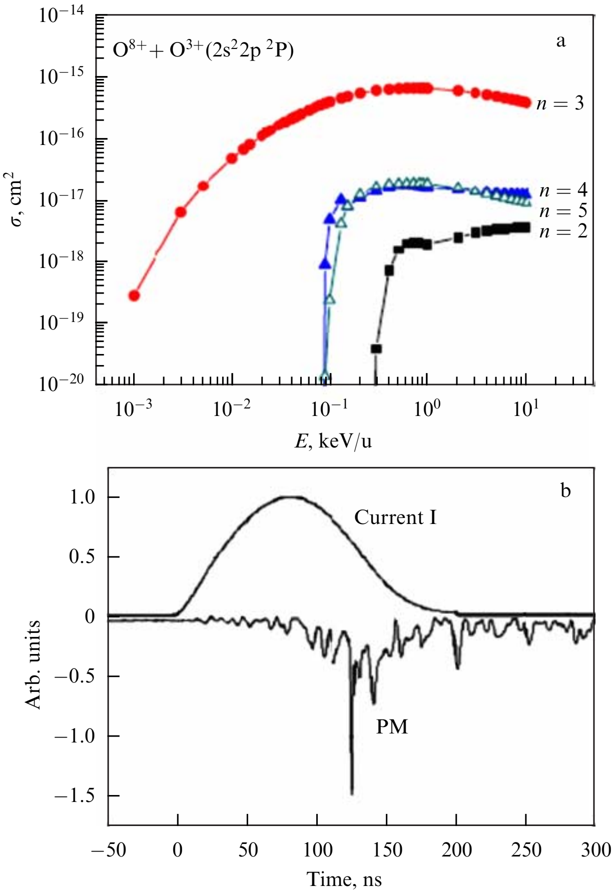

Figure 15. (a) Ion–ion charge-exchange cross sections for the reaction $O^{8+} + O^{3+}(2s^2\,2p\,^2P) \to O^{7+}(n) + O^{4+}$, $n = 2-5$, calculated in the adiabatic approximation by the hidden crossing method [204]. (b) Experimental evolutions of the current in the capillary discharge (current I) and the Balmer-α line emission (PM) in the O^{7+} ion [204].

In Refs [204, 205], the charge exchange cross sections were calculated for collisions of bare nuclei with ions of lower degrees of ionization that exist in cold regions of the plasma. The calculations were performed in the adiabatic approach [198] using the ARSENY program [202] based on the method of hidden crossings. A detailed description of the theoretical method is given in paper [163].

Figure 15a shows the dependences of the charge exchange cross sections of oxygen ions on collision energy; this process populates the ion final states with principal quantum numbers $n = 2-5$. As in the case of carbon ions (57), the largest charge exchange cross sections at low collision energies are achieved for the reaction (58), for which the electronic transition occurs due to radial interaction associated with the change in the internuclear distance.

In Fig. 15b, a typical example of the time evolution of the current in a capillary (current I) and the Balmer-α emission line in the O^{7+} ion at 10.24 nm (PM) is shown. At a time $t \approx 125$ ns, a sharp deep peak is observed in the PM curve with a duration of about 1 ns, which is interpreted [204] as the instant of the creation of inverse population. The results of Refs [204, 205] show the possibility of Balmer-α line generation in the O^{6+} and C^{5+} ions in the capillary discharge due to the selective population of the level $n = 3$ by ion–ion charge exchange during developing $m = 0$ plasma instability.

5.2 Electron-loss processes — ionization of incident ions by target atoms

Experimentally and theoretically, the processes of heavy ions stripping by neutral atoms (42) have been studied in more detail than the processes of charge exchange, including multielectron processes ($m > 1$), which have large effective cross sections, especially in the case of many-electron targets at low and medium collision energies (see, e.g., review [26]). Experimental data for stripping cross sections of heavy ions were obtained mainly for gas targets H_2, He, N_2, O_2, Ne, Kr, and Xe, as well as for complex molecules [214] in the nonrelativistic energy range of $E < 200$ MeV/u.

In recent years, the behavior of the stripping cross sections of heavy ions at *relativistic* energies, i.e., for $E > 200$ MeV/u, has attracted attention due to both purely theoretical interest and experimental investigations, started in 2011 within the framework of the FAIR International Project (Facility for Antiproton and Ion Research) [35]. In the energy range of 80 MeV/u–1 GeV/u, measurements of the stripping cross sections were carried out mainly for solid targets (foils) from Be to U [215–223].

When calculating the cross sections of single- and multiple-electron stripping of fast ions by neutral atoms, the following approaches are applied: the sudden perturbation method [224], the relativistic Born approximation [225], the classical trajectory Monte Carlo (CTMC) method [153, 168], and the classical approach in the energy deposition representation [226, 227]. Furthermore, a large contribution (up to 50%) to the total stripping cross sections at medium collision energies is made by multiple-electron ionization of incident ions (see Section 5.2.1).

Electron-loss cross sections (42) of heavy ions by neutral atoms reach their maximum at relative velocities $v \sim (I_P/\mathrm{Ry})^{1/2}$, where I_P is the ionization potential of the incident ion, mainly due to multiple-electron ionization. In this energy range, the Born approximation gives highly overestimated results; therefore, for calculating multiple-electron loss cross sections, classical methods like CTMC or energy deposition are used.

Figure 16 plots the dependence of the electron-loss cross sections for U^{28+} ions with energies of 30 and 50 MeV/u on the target atomic number Z_T from H to Xe. The experimental data (dark dots) are in good agreement with calculations of the cross sections using the DEPOSIT and the RICODE programs. The CTMC calculations overestimate the experiment by about a factor of 2.

At energies $E \approx 50-500$ MeV/u, the stripping cross sections are described well by the Born approximation with account for a contribution to the ionization process not only from outer-shell electrons, but also, importantly, from *inner* shells of the projectile ion. Electron-loss cross sections are scaled by the Bohr formula through ionization cross sections by electron (σ_{el}) and proton (σ_{pr}) impacts:

$$\sigma_{EL} \approx Z^2 \sigma_{pr}(v) + Z\sigma_{el}(v) \approx Z^2 + Z\,, \quad v^2 \gg I_P\,, \qquad (59)$$

where I_P is the ionization potential of the incident ion, and Z is the atomic number of the target atom.

At high velocities, the loss cross sections decrease by a law in accordance with the nonrelativistic Born approximation:

$$E \to \infty\,, \quad v \to \infty\,, \quad \sigma_{EL} \to Z^2 \frac{\ln v}{v^2} \sim Z^2 \frac{\ln E}{E}\,, \qquad (60)$$

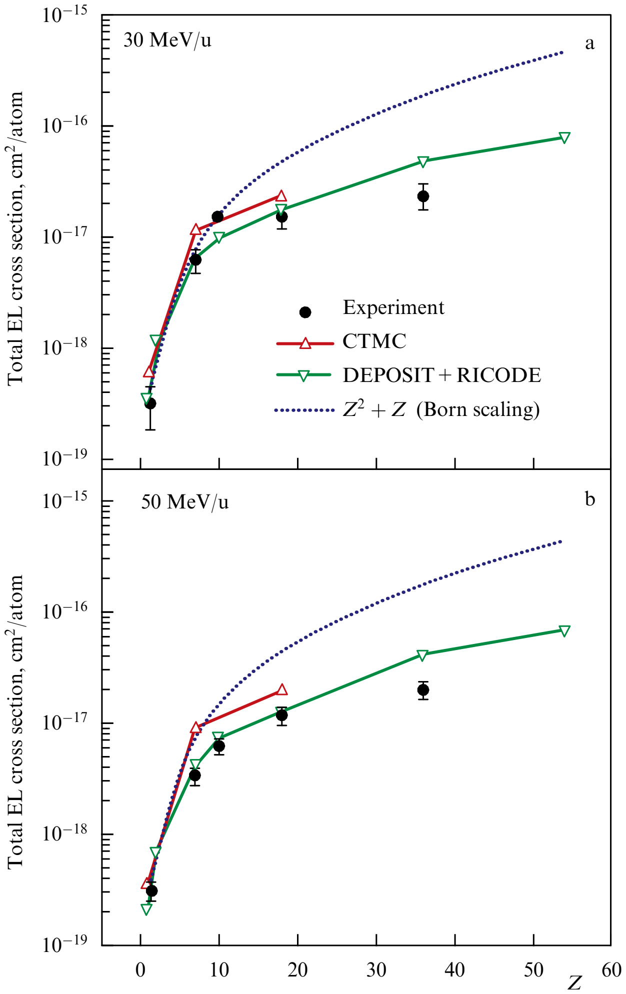

Figure 16. (Color online.) Dependence of the total electron-loss cross sections for U^{28+} ions with energies of 30 and 50 MeV/u on the target atomic number Z. Experiment: dark dots (GSI, Darmstadt [151]). Theory: $\triangledown$ — result of the energy deposition method (DEPOSIT code) [226] and the relativistic Born approximation (RICODE program) [225], $\triangle$ — CTMC [153], and dashed curve — scaling (59). (Taken from Ref. [151].)

i.e., the heavier the target atom, the more easily the projectile ion is ionized.

At relativistic ion energies, the electron-loss cross sections by neutral atoms become quasiconstant due to the influence of relativistic effects, and, unlike ionization by *neutral* atoms, the loss cross sections by *ions* increase logarithmically with energy as $\ln\gamma$:

$$E \to \infty\,, \quad v \to c\,, \quad \sigma_{EL} \sim \ln\gamma\,, \quad \text{for ionic targets}\,,$$
$$\sigma_{EL} \to \text{const}\,, \quad \text{for atomic targets}\,, \qquad (61)$$

where γ is a relativistic factor.

To estimate the electron-loss cross sections of heavy ions by neutral atoms at high energies, including the relativistic domain, a semiempirical formula was obtained in paper [228] based on numerical calculations and the properties of the Born approximation in the form

$$\sigma\left[\frac{\mathrm{cm}^2}{\mathrm{atom}}\right] = 0.88 \times 10^{-16}(Z+1)^2 \frac{u}{u^2 + 3.5}\left(\frac{\mathrm{Ry}}{I_P}\right)^{1+0.01q} \times \left(4.0 + \frac{1.31}{n_0}\ln(4u+1)\right), \qquad (62)$$

Table 2. Experimental cross sections of m-electron stripping, σ_m ($m = 1, 2$, and 3), and total cross sections σ_{tot} in collisions of Xe^{18+} and Ar^{8+} ions with inert gas atoms.

Process	Energy, MeV/u	σ_1, 10^{-18} cm^2	σ_2, 10^{-18} cm^2	σ_3, 10^{-18} cm^2	σ_{tot}, 10^{-18} cm^2	Reference
$\mathrm{Xe}^{18+} + \mathrm{He}$	6	3.0	1.7	0.2	4.9	[214]
$\mathrm{Xe}^{18+} + \mathrm{Ne}$	6	16	7.8	3.8	36	[214]
$\mathrm{Xe}^{18+} + \mathrm{Ar}$	6	24	11	5.6	56	[214]
$\mathrm{Xe}^{18+} + \mathrm{Kr}$	6	27	13	7.2	75	[214]
$\mathrm{Xe}^{18+} + \mathrm{Xe}$	6	34	16	9.0	95	[214]
$\mathrm{Ar}^{8+} + \mathrm{Xe}$	19	23	10	5.5	44	[155]

$$u = \frac{v^2}{I_{\mathrm{P}}/\mathrm{Ry}} = \frac{(\beta c)^2}{I_{\mathrm{P}}/\mathrm{Ry}}\,, \qquad (63)$$

where v and q are the velocity and charge of the incident ion, $\beta = v/c$, $c = 137$ is the speed of light, u is the reduced energy, Z is the atomic number of the target atom, I_{P} is the ionization potential of the incident ion in Ry, and n_0 is the principal quantum number of the outer shell in the incident ion.

The cross section (62) reaches its maximum at $u \approx 2$:

$$\sigma_{\max}\left[\frac{\mathrm{cm}^2}{\mathrm{atom}}\right] \approx 10^{-16}(Z+1)^2\left(\frac{\mathrm{Ry}}{I_{\mathrm{P}}}\right)^{1+0.01q}, \quad u_{\max} \approx 2\,. \quad (64)$$

For $v \to c$, cross section (62) tends to a constant value:

$$\sigma\left[\frac{\mathrm{cm}^2}{\mathrm{atom}}\right] \approx 3\times10^{-20}(Z+1)^2\left(\frac{\mathrm{Ry}}{I_{\mathrm{P}}}\right)^{0.01q}, \quad u \approx c^2\,\frac{\mathrm{Ry}}{I_{\mathrm{P}}}\,.$$

Formula (62) describing electron-loss cross sections is similar to formula (53) for electron-capture cross sections; these formulas can be adapted to estimate the lifetimes of ion beams in accelerators for ions passing through gaseous media (see review [26]).

5.2.1 Multiple-electron ionization of heavy ions. Ionization of heavy ions by neutral atoms (loss or stripping collisions), similar to the processes of electron capture, is characterized by a high probability of multiple-electron ionization, leading to its significant contribution to the total cross sections at low and medium collision energies. The magnitude of the contribution from multiple-electron ionization depends on the collision energy and the atomic structure of the colliding atomic particles. Table 2 collates the experimental cross sections of single-electron processes and the total electron-loss cross sections for collisions of xenon and argon ions with inert gas atoms. It is seen that, even for Ar^{8+} ions with ten electrons, the contribution of multiple-electron ionization is about 50%.

5.2.2 Ionization of target atoms. As an ion beam passes through a medium, information about the degree of ionization of atoms and molecules in the *medium* is of great importance, especially in estimating the conditions imposed on the pressure and concentrations of residual gas particles in high-power accelerators. The ionization of atoms and molecules of the residual gas by incident ions (44) leads to the appearance of a long-range Coulomb interaction between the particles and, at very high beam densities, to so-called *dynamic vacuum effects* [229], which significantly affect the ion–beam lifetimes and losses. In addition, data on ionization cross sections of neutral atoms and molecules by ion beams are of interest in beam therapy of various types of tumors, for example, for taking into account the effect of secondary electrons in the patient's body, which can lead to damage much greater than the direct damage by the incident ions.

Experimental and theoretical studies of the ionization of neutral atoms by multiply charged ions (including multiple-electron ionization) were carried out mainly in 1980–1995 (see Refs [23, 25, 230] and references cited therein). Experimental data were obtained mainly for inert He, Ne, Ar, Kr, and Xe gases at the BEVALAC (Berkeley, USA), UNILAC (Darmstadt, Germany), and RIKEN NC (Tokyo, Japan) accelerators for ion beams from protons to bare uranium nuclei at energies of 1–420 MeV/u. The accuracy of measuring the ionization cross sections of neutral atoms is about 30–50%.

Several basic theoretical approaches are used to calculate the ionization cross sections of neutral atoms by multiply charged ions: the independent particle method (IPM [231]), the Monte Carlo method (CTMC) [168], the classical deposition-energy model [232], and the quantum statistical approach [233, 234].

Recently, a method has been proposed in paper [230] for the determination of multiple-electron ionization cross sections of atoms by highly charged ions in the energy range of 1 MeV/u– 10 GeV/u with an accuracy up to a factor of 2, which is based on a combination of classical and quantum approaches. The contribution from multiple-electron ionization, which amounts to 20–35%, decreases with increasing energy but increases with increasing the atomic number of the target atom. These properties are illustrated in Fig. 17, where multiple-electron cross sections for the ionization of Ne and Ar atoms by multiply charged heavy ions are presented in a wide energy range, including relativistic energies.

5.3 Relativistic collisions.
Radiative electron-capture processes

At high incident ion energies, a recombination process competing with the 'normal' nonradiative capture NRC (43) is the radiative electron capture (REC) (45). REC is similar to the radiative recombination (RR) process, but differs by the capture of bound, not free, target electrons and the emission of a photon. The main results on REC processes, obtained experimentally and theoretically, are presented in review [143].

At high kinetic energy, the incident ion 'sees' that the weakly bound target electrons are practically motionless, so electron capture occurs with the emission of a photon as a third body, which takes away an excessive fraction of energy and momentum according to the conservation laws. REC processes are weaker depending on the effective charge of the target atoms, but with increasing energy their cross sections decrease much more slowly than NRC cross sections [see formulas (47), (48)]; therefore, under certain conditions it is necessary to take into account both recombination processes. At very high relativistic energies (relativistic factor $\gamma > 10$),

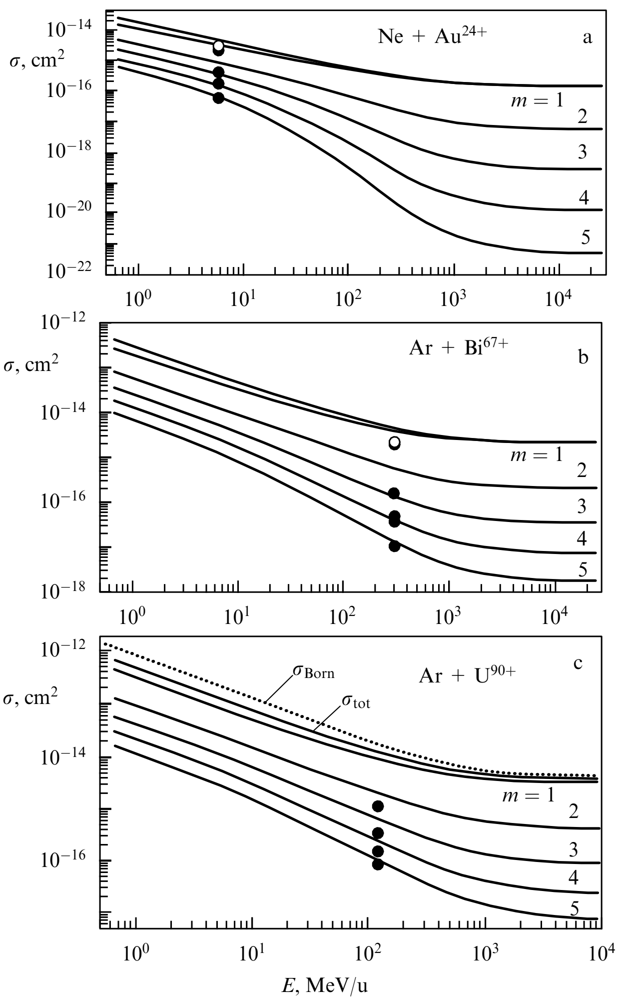

Figure 17. Cross sections of m-electron ionization of Ne and Ar atoms by Au^{24+} (a), Bi^{67+} (b), and U^{90+} (c) ions as a function of ion energy. Symbols — experiment: dots and circles — m-electron and total ionization cross sections, respectively [235, 236]. Curves — combined calculations in classical and quantum-mechanical approximations [230].

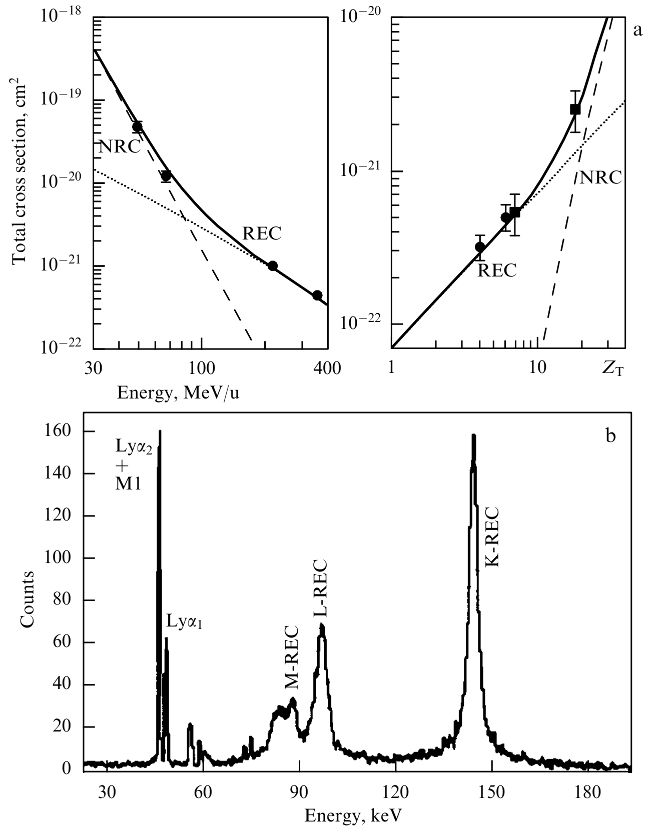

Figure 18. (a) NRC, REC, and the total charge-exchange cross sections of U^{92+} ions (bare nuclei) on neutral atoms at high collision energies. The left panel is the charge-exchange cross sections for N_2 molecules as a function of ion energy: the dashed line is the NRC cross section in the eikonal approximation, the points fit the REC cross section in the dipole approximation, and the solid curve is the total cross section — the sum of the NRC and REC cross sections. The right panel shows electron-capture cross sections for gaseous and solid targets at 295 MeV/u for the U^{92+} ion as a function of nuclear charge $Z_{\rm T}$ of a target atom: the dashed line is the NRC cross section in the eikonal approximation, the points fit the REC cross section in the dipole approximation, the solid curve is the total cross section — the sum of the NRC and REC cross sections. Experiment: solid squares — N_2 and Ar targets, dots — Be and C targets. (Taken from Ref. [251].) (b) X-ray spectrum of the H-like U^{91+} ion measured by the coincidence method for radiative capture of bare U^{92+} nuclei on nitrogen N_2 at 310 MeV/u. In addition to the usual transitions to the ground state (the Lyα_1, Lyα_2, M1 transitions), the peaks (K-, M-, and L-REC) associated with the decay of the states formed as a result of electron capture into the ground and excited states of the H-like U^{91+} ion are clearly seen. (Taken from Ref. [143].)

the electron capture of ions on atoms is accompanied by the formation of electron–positron pairs (see Refs [143, 237]), but these processes are not considered here.

X-ray spectra of REC photons play an important role in the spectroscopy of highly charged ions, in particular, in determining the polarization of radiation, photoionization of heavy ions, the probabilities of radiative transitions, studying the quantum electrodynamics effects, etc. (see Refs [143, 238]).

The first measurements of REC were performed in studies [239–241] at the BEVALAC accelerator at the Lawrence Berkeley National Laboratory, Berkeley CA (USA), and then with the development of powerful heavy-ion accelerators at other facilities, in particular, at SUPER-EBIT in Berkeley and at the Helmholtz Centre for Heavy Ion Research (GSI) in Darmstadt (see Ref. [143]). Calculation of the NRC cross sections in the relativistic region is carried out in the eikonal approximation [242–244], and the REC cross sections in the impulse approximation [143], the density matrix approximation [237], and the relativistic approximation [245, 246]. For estimations of the REC cross sections, the formulas of Stobbe [247] and Kramers [248] are often employed. The results of calculations of the NRC cross sections in the relativistic eikonal approximation are given in paper [249], and the radiative recombination and REC cross sections for bare nuclei of heavy ions are given in tables [250].

Figure 18a depicts experimental and theoretical cross sections of radiative and nonradiative electron capture of H-like uranium ions as a function of energy (on the left) and of the target atomic number (right). It can be seen that with an increase in energy and target atomic number, the radiative capture becomes dominant.

The experimental X-ray spectrum of H-like uranium ions formed during the radiative electron capture of bare uranium ions on nitrogen N_2 at an energy of 310 MeV/u is shown in Fig. 18b. It can be seen that the spectrum has a rather complex structure, where, in addition to transitions to the ground state, the lines associated with radiative transitions between excited states are also detected.

5.4 Target-density effects in electron capture and loss cross sections

The *density effect* (*target-density* or *gas-solid effect*) consists in increasing the average (equilibrium) charge of an ion beam in passing through a solid body in comparison with a gaseous target. The effect was observed experimentally by Lassen [117, 118] in studying beams of uranium ions passing through a carbon foil and a gaseous target, and later in measuring the energy loss (*stopping power*) for ions in gaseous and solid media [119, 125].

Briefly, the density effect consists in the following (see also review [1] and Section 3.6). In a rarefied medium (gas at low pressure), ions experience one or two collisions with the particles of the medium. In a dense medium, the time between neighboring collisions becomes shorter than the lifetime of the excited ionic states, which are destroyed by subsequent collisions with media particles, leading to ionization of excited ions, i.e., to an increase in their charge. In a dense medium, the charge exchange cross sections decrease, and, in contrast, the electron loss cross sections increase due to the contribution of ionization from excited states of the ions. The combined influence of both effects leads to an increase in the equilibrium average ion charge in a denser medium (see Refs [26, 126, 172, 252]).

The influence of the density effect naturally depends on the density of the target atoms, as well as on the ion energy and the atomic structure of colliding particles, i.e., on atomic energy levels, including inner shells, the probabilities of radiative transitions, excitation cross sections, and others. The density of particles, for example, molecules in a gaseous target, can be small, but the density effect can be very significant. With increasing target density, the electron capture cross sections can decrease up to 10 or more times, and the ionization cross sections increase by a factor of 1.5–2; therefore, when studying problems involving the passage of an ion beam through a medium, one must take into account the density effect generated by any medium: a gas, plasma, or solid.

The influence of the density effect on the charge exchange and stripping cross sections of 4 MeV (113 keV/u) chlorine ions upon passage through a molecular hydrogen target is illustrated in Fig. 19a at hydrogen densities $N = 5 \times 10^{13}$ – 3×10^{16} molecules/cm^3. These dependences were obtained from experimental data on ionic fractions of chlorine ion beams. It can be seen that the capture cross sections for the reaction $\mathrm{Cl}^{q+} \to \mathrm{Cl}^{(q-1)+}$ decrease to approximately 1.5 times under the given conditions, but the loss cross sections for $\mathrm{Cl}^{q+} \to \mathrm{Cl}^{(q+1)+}$ increase by approximately 20%. The density effect manifests itself more strongly at high densities, especially when ions pass through a solid body, where the density of atoms is of the order of 10^{23} atom/cm^3.

Figure 19b demonstrates the dependence of the loss and capture cross sections for argon ions at an energy of 6 MeV/u passing through a graphite foil as a function of argon charge calculated with and without the density effect. Calculated capture cross sections, when the effect is taken into account, decrease by approximately an order of magnitude, and the stripping cross sections increase about twofold. Accounting for the density effect leads to an average ion charge $\langle q \rangle = 16.8$, close to the experimental one: $\langle q \rangle_{\mathrm{exp}} = 17.0$, while the average charge calculated without the density effect is lower: $\langle q \rangle = 15.0$.

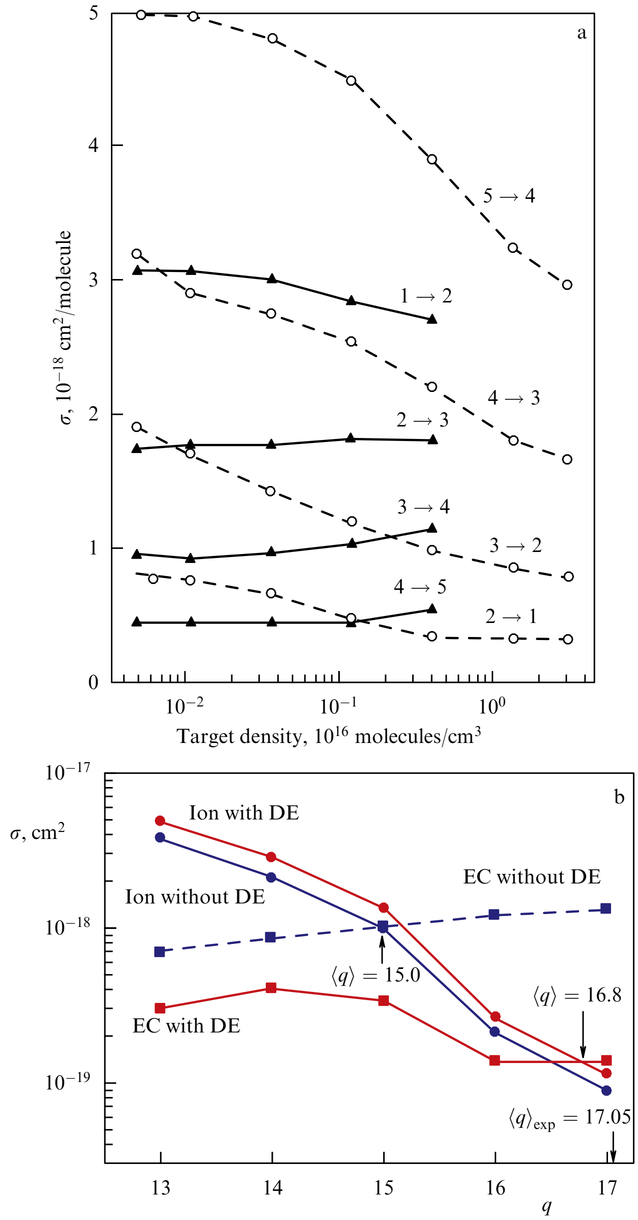

Figure 19. (a) Effective cross sections for single-electron capture $q \to q-1$ and stripping $q \to q+1$ of Cl^{q+} ions with an energy of 4 MeV (113 keV/u) passing through molecular hydrogen with a density of $5 \times 10^{13} - 3 \times 10^{16}$ molecules/cm^3 as a function of the target density. (Taken from Ref. [253].) (b) Effective cross sections for single-electron capture (EC) and loss (EL) of Ar^{q+} ions with an energy of 6 MeV/u passing through a carbon foil of a density of 1.3×10^{23} atom/cm^3 as a function of ion charge q, calculated with and without accounting for the target-density effect. The capture and loss cross sections, calculated with allowance for the density effect, intersect at $q = 16.8$, i.e., for an average ion charge close to the experimental value $\langle q \rangle_{\mathrm{exp}} = 17.0$. (Taken from Ref. [254].)

5.5 Processes of ion interactions with plasmas

Atomic characteristics of interactions between ion beams and plasmas are required to solve many problems in beam plasma diagnostics, e.g., by the heavy-ion beam probe (HIBP) method [255]), determining stopping power for ions in plasma (Section 3.5), determining the optimal conditions for obtaining the maximum charge of exit ion beams leaving different targets, and others.

The interaction of ions with plasma differs significantly from processes involving neutral atoms in ion passage through gaseous and solid targets, because of the presence of free electrons and ions in the plasma. In addition, the cross sections (more precisely, the rate coefficients of the processes) of the interactions between ions and the plasma highly depend on the temperature, electron density, and ionic components of the plasma.

Due to the presence of free electrons and ions in a plasma, besides the *loss* and *capture* processes on neutral atoms considered in Sections 5.1 and 5.2, additional interaction processes arise that lead to a change in the charge state of the incident ions. Let us consider the main additional processes.

(1) Radiation recombination — charge transfer (capture) of free electrons with a photon emission:

$$X^{q+} + \mathrm{e}^- \to X^{(q-1)+}(nl) + \hbar\omega\,, \quad \hbar\omega = E_{\mathrm{e}} + E(nl)\,, \quad (65)$$

where q is the charge of the X^{q+} ion, E_{e} is the kinetic energy of a free electron, $E(nl)$ and $E(nl) > 0$ is the binding energy of the ion in the state with quantum numbers n, l, whereto the electron was captured. Process (65) is inverse to photoionization and occurs at *any* energy E_{e} of a free electron.

(2) Dielectronic recombination:

$$X^{q+} + \mathrm{e}^- \to \left[X^{(q-1)+}\right]^{**} \to X^{(q-1)+}(nl) + \hbar\omega\,, \quad (66)$$

a two-step process, which is first accompanied by the capture of a free electron with simultaneous excitation of the inner-shell electron in the ion and the formation of an intermediate doubly excited state, and then by radiative decay, which leads to the formation of the ion $X^{(q-1)+}(nl)$ with photon emission, similarly to reaction (65). However, there is a big difference between processes (65) and (66): while the process (65) is possible for *any* values of the kinetic energy E_{e} of the free electron, process (66) only occurs at certain values E_{e} corresponding to the *resonance* condition:

$$E_{\mathrm{e}} \approx \Delta E - \frac{q^2\,\mathrm{Ry}}{n^2} < \Delta E\,, \quad \Delta E > 0\,, \quad (67)$$

where ΔE is the excitation energy driving transition in the ion $X^{(q-1)+}$.

(3) Ternary (three-particle) recombination — the inverse process of electron-impact ionization:

$$X^{q+} + \mathrm{e}^- + \mathrm{e}^- \to X^{(q-1)+} + \mathrm{e}^-\,. \quad (68)$$

(4) Multiple-electron ionization of the incident ion by free electrons e^- or A^{k+} ions in a plasma:

$$X^{q+} + \mathrm{e}^-,\ A^{k+} \to X^{(q+m)+} + A^{k+} + m\mathrm{e}^-\,, \quad m \geqslant 1\,. \quad (69)$$

(5) Ionization of the incident ion as a result of charge exchange with plasma ions, i.e., of ion–ion electron capture:

$$X^{q+} + A^{k+} \to X^{(q+1)+} + A^{(k-1)+}\,. \quad (70)$$

Cross sections and rate constants of processes (65)–(70), averaged over the Maxwellian energy distribution of the particles, have been well studied experimentally and theoretically under conditions of an isolated plasma (see Refs [11, 13, 26]).

5.5.1 Radiative recombination (RR). Radiative recombination relates to one of the main recombination mechanisms occurring in the passage of ions through a plasma target, since it occurs with a greater probability than electron capture on plasma atoms and ions.

Cross sections of radiative recombination (65) into Rydberg levels with $n \gg 1$, averaged over the orbital quantum numbers l, are usually determined by the Kramers formula [73, 256] or by semiempirical formulas [248] using the effective charge for the resulting ion $X^{(q-1)+}$. For low-lying n levels, the Kramers cross sections have to be multiplied by the Gaunt factor (see Refs [257, 258]).

The cross section of process (65) covering all levels n of the ion $X^{(q-1)+}(n_0^p)$ is given by the formula with account for vacancy of the shell n_0^p of the ground state (p is the number of equivalent electrons):

$$\sigma_{\mathrm{RR}}^{\mathrm{tot}}(n, E_{\mathrm{e}}) = \left(1 - \frac{p}{2n_0^2}\right)\sigma_{\mathrm{RR}}(n_0, E_{\mathrm{e}}) + \sum_{n>n_0}^{n_{\mathrm{cut}}} \sigma_{\mathrm{RR}}(n, E_{\mathrm{e}})\,, \quad (71)$$

where n_{cut} is the maximum principal quantum number, determined by the experimental conditions (large electron density, external electric field strength, etc.). We note that the main contribution to sum (71) is made by recombination to the ground state n_0 and the nearest levels. At large free-electron energies E_{e}, the cross section $\sigma_{\mathrm{RR}}(n, E_{\mathrm{e}}) \sim q^4/(n^3 E_{\mathrm{e}}^2)$.

5.5.2 Dielectronic recombination (DR). Dielectronic recombination represents an important recombination process that plays a principal role in the plasma ionization balance, in the deceleration of ion beams in a plasma and the formation of the effective charge in it, and in the study of the atomic characteristics of heavy many-electron ions such as the Lamb shift, isotope shift, and others (see Refs [259–261]). In addition, the emission spectral lines, called *dielectronic satellites*, play an important role in the diagnostics of hot plasmas, i.e., in determining its temperature, density, ionic components, etc. [11, 262].

DR cross sections are expressed in terms of the radiative and autoionization transition probabilities for the ground, intermediate, and final states, and manifest themselves as narrow resonances, the maximum of which increases substantially (approximately as q^4) with an increase in the ion charge q.

A diagram of the cross sections for radiative and dielectronic recombinations is presented in Fig. 20a as a function of electron energy. At low energies, the RR process prevails. As the energy increases, DR resonances appear in states with principal quantum numbers n, whose intensity decreases with increasing n as n^{-3}. Figure 20b shows the DR cross section (rate constant) of lithium-like Ni^{25+} ions for the $2\mathrm{s}-2\mathrm{p}$ transition, averaged over the electron distribution function; the principal quantum numbers n of resonances are marked in the figure.

It should be noted that the experimental and theoretical investigations of recombination processes, involving many-electron heavy ions, meet with significant difficulties associated with the atomic structure of such systems, since the number of electronic levels is very large even for the ground state. Figure 20c depicts results of the calculations of the density of states (the number of levels per energy unit) of W^{19+} ions which can be populated as a result of the DR of W^{20+} ($4\mathrm{f}^8\,{}^7\mathrm{F}_6$) ions through doubly excited $4\mathrm{f}^8 nl$ states. It can be seen that the density of levels is enormously high: 10^7 levels per eV of energy! Naturally, in calculating the cross

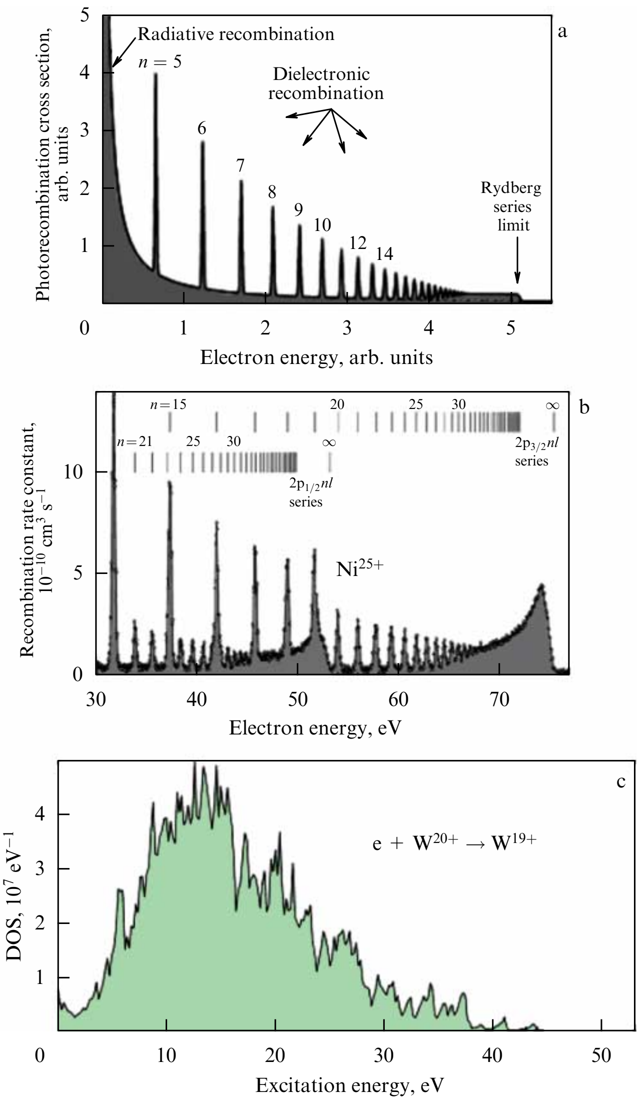

Figure 20. (a) Cross sections of radiative and dielectronic recombinations as a function of free-electron energy E_e. The principal quantum numbers of the Rydberg states, into which the electron capture took place, are indicated. (Taken from Ref. [263].) (b) Experimental DR rate constant of lithium-like Ni^{25+} ions for the 2s–2p transition, i.e., the quantity $\langle v\sigma_{DR}\rangle$ averaged over the electron energy distribution function in the storage ring; the principal quantum numbers n of resonance states are indicated in the figure. (Taken from Ref. [264]). (c) Results of the calculations of the density of W^{19+} ion states, which can be populated as a result of DR of W^{20+} $(4f^8\,{}^7F_6)$ ions through doubly excited $4f^8 nl$ states. (Taken from Ref. [260].)

sections and rate constants of recombination of heavy ions, conventional methods cannot be used; therefore, new approaches are applied, for example, the *quantum chaos* method [265–268] on the basis of a statistical approach to analyzing the spectrum and eigenvalues of quantum states of ions, which leads to much better agreement between theory and experiment (see paper [266]).

The processes of electron capture (65) and ionization (69) are considered in Refs [13, 16, 17, 23, 26, 50]. To calculate the cross sections for single-electron ionization by electron impact, Lotz's semiempirical formulas are widely used [269], and the cross sections for multiple-electron ionization are calculated according to the semiempirical formulas given in Refs [270–274].

5.5.3 Rate constants of the processes. Plasma components (atoms, ions, electrons) have different concentrations, depending on plasma temperature and density, so to describe an interaction of incident ions with a plasma, the *rate constants of the processes* are used, i.e., $N\langle v\sigma\rangle$ [s^{-1}] quantities averaged over a Maxwellian distribution of particle velocities v; here, N is the particle density (concentration) in a plasma.

When the ion *beam* interacts with a plasma, a Maxwellian function of the electron (or ion) velocity distribution $F(v, v_p, T)$ depends on the *projectile-ion velocity* v_p in a beam, and the quantity $\langle v\sigma\rangle$ [$cm^3\ s^{-1}$] is given by expression [15]:

$$\langle v\sigma\rangle = \int_0^\infty v\sigma(v)\,F(v, v_p, T)\,d^3v\,, \quad \int_0^\infty F(v, v_p, T)\,dv = 1\,, \tag{72}$$

$$\begin{aligned} F(v, v_p, T) &= \left(\frac{M}{2\pi k_B T}\right)^{3/2} \exp\left[-\frac{M}{2k_B T}(\mathbf{v}-\mathbf{v}_p)^2\right] \\ &= \left(\frac{M}{2\pi k_B T}\right)^{1/2} \frac{v}{v_p} \left\{\exp\left[-\frac{M}{2k_B T}(v-v_p)^2\right]\right. \\ &\quad \left. - \exp\left[-\frac{M}{2k_B T}(v+v_p)^2\right]\right\}, \end{aligned} \tag{73}$$

where $\mathbf{v} = \mathbf{v}_p - \mathbf{v}_{e,i}$ is a relative velocity vector, $v_{e,i}$ is the electron or ion velocity in a plasma, M is the reduced mass of colliding particles, and T is the electron or ion plasma temperature.

For low incident-ion velocities $v_p \to 0$, the function $F(v, v_p, T)$ transforms to the 'usual' Maxwellian function $F(v, T)$, while at a relatively low plasma temperature one obtains

$$F(v, v_p, T) = \delta(v - v_p)\,, \quad \frac{2T}{M} \to 0\,, \tag{74}$$

$$\langle v\sigma\rangle \approx v_p \sigma(v_p)\,, \quad v_p \gg v_{th} = 1.13\sqrt{\frac{2T_e}{m}}\,, \tag{75}$$

where v_{th} is the thermal electron velocity in plasma. Thus, the rate constants for the processes involving fast projectiles in a cold plasma are defined by the *product* of the ion velocity and cross section of the process. Two important consequences follow from this inference:

(1) the rate constants of atomic processes for fast heavy ions do not depend on the plasma temperature or velocity distribution of plasma particles;

(2) the rate constants are determined only by the cross sections of the processes.

In the case of low ion velocities, $v_p \leqslant v_{th}$, the rate constants of processes are defined by formula (72), i.e., using a Maxwellian function which depends on ion velocity v_p and plasma temperature T.

The most often realized case is $v_p \geqslant v_{th}$, when the rate constants of all considered processes (except three-particle recombination) depend linearly on the particle density N:

$$\kappa = N v_r \sigma(v_r)\ [s^{-1}]\,, \tag{76}$$

$$v_r \approx \sqrt{v_p^2 + v_{th}^2}\,, \qquad v_{th} \approx 1.13\sqrt{\frac{2T_e}{m}}\,, \tag{77}$$

where v_r is the relative velocity of incident ions, N is the particle density, and T_e is the plasma electron temperature.

5.5.4 Three-particle (ternary) recombination (TR). Two incoming electrons participate in the TR process (68): one is captured by an ion, and the other carries away the excess part of the energy. The TR rate constant is usually calculated in the classical approximation [275]:

$$\kappa_{\mathrm{TR}} = \frac{2^5 \pi^2 e^{10}}{m^5} \frac{q^3 N_{\mathrm{e}}^2}{v_{\mathrm{r}}^9}$$
$$\approx 2.9 \times 10^{-31}\ [\mathrm{cm^3\,s^{-1}}] N_{\mathrm{e}}^2\ [\mathrm{cm^{-3}}]\ \frac{q^3}{v_{\mathrm{r}}^9\ [\mathrm{a.u.}]}\,, \qquad (78)$$

where q is the incident-ion charge, and v_{r} is the relative velocity (77).

A comparison of the RR and TR rates for the case of $v_{\mathrm{p}} \geqslant v_{\mathrm{th}}$ gives the following estimate [50]:

$$\frac{\kappa_{\mathrm{RR}}}{\kappa_{\mathrm{TR}}} = 1.6 \times 10^{17}\ \frac{q v_{\mathrm{r}}^6}{N_{\mathrm{e}}\ [\mathrm{cm^{-3}}]}\,. \qquad (79)$$

It is seen from the last formula that the rate constant κ_{TR} is small and is comparable to the recombination rate only at very high electron densities.

A comparison of the rate constants of electron capture (EC) and radiative recombination (RR) processes gives

$$\frac{\kappa_{\mathrm{EC}}}{\kappa_{\mathrm{RR}}} \approx 10^7\ \frac{N_{\mathrm{at}}}{N_{\mathrm{e}}}\ \frac{q Z_{\mathrm{T}}^5}{v_{\mathrm{r}}^8\ [\mathrm{a.u.}]}\,, \qquad (80)$$

where N_{at} and N_{e} are the densities of neutral atoms and electrons in a plasma, and Z_{T} is the target atomic number. The relative contribution of EC and RR processes depends on the density ratio $N_{\mathrm{at}}/N_{\mathrm{e}}$ and the ion relative velocity v_{r}.

Figure 21a depicts concentrations of protons and neutral hydrogen atoms in the hydrogen plasma as a function of plasma temperature. In a cold plasma, $T \approx 1$ eV, the ratio $N_{\mathrm{at}}/N_{\mathrm{e}} \approx 30$, and for ions with $q = 20$ and energy 1.5 MeV/u ($v_{\mathrm{p}} = 7.7$ a.u.), the ratio of the rate constants (80) is on the order of 10^3, i.e., in a cold plasma, the rate constant of electron capture on neutral atoms far exceeds the rate constant of radiative recombination. In a fully ionized hydrogen plasma with temperature $T \approx 10$ eV, the ratio $N_{\mathrm{at}}/N_{\mathrm{e}} \approx 10^{-5}$, and the ratio of the rate constants reaches

$$\frac{\kappa_{\mathrm{RR}}}{\kappa_{\mathrm{EC}}} \approx 10^3\,, \qquad (81)$$

i.e., in a strongly ionized plasma, the RR process is the main recombination process.

This is confirmed by the data in Fig. 21b, where the rate constants of recombination and ionization of iodine ions with charges $q < 60$ and energy 1.5 MeV/u in a hydrogen plasma with temperature $T \approx 10$ eV and electron density $N_{\mathrm{e}} \approx 10^{17}$ cm^{-3} are given. Rate constants presented in Fig. 21b were calculated with the following parameters: iodine charge ranges $0 \leqslant q < 60$, ion energy is 1.5 MeV/u, and, for H plasma, electron temperature $T_{\mathrm{e}} = 10$ eV and density $N_{\mathrm{e}} = 10^{17}$ cm^{-3}. For ions with $q > 5$, the ionization rates practically coincide for the gas and plasma targets.

As can be seen from Fig. 21b, in a strongly ionized plasma, the RR rate is much larger than EC rate, and the TR rate is much smaller than the EC and RR rates. From Fig. 21b, it is also possible to estimate the average charge $\bar{q}$ of iodine ions in a cold hydrogen gas and a fully ionized plasma: $\bar{q}_{\mathrm{gas}} \approx 20$ and $\bar{q}_{\mathrm{plasma}} \approx 40$ (indicated by the arrows in the figure). Thus, plasma is a more efficient medium for stripping heavy ions than a cold gas of the same element, as discussed in Section 3. The main difficulty in considering the SP in a plasma relates to accounting for dielectronic recombination processes, which play an important role in the recombination of ion beams in a plasma.

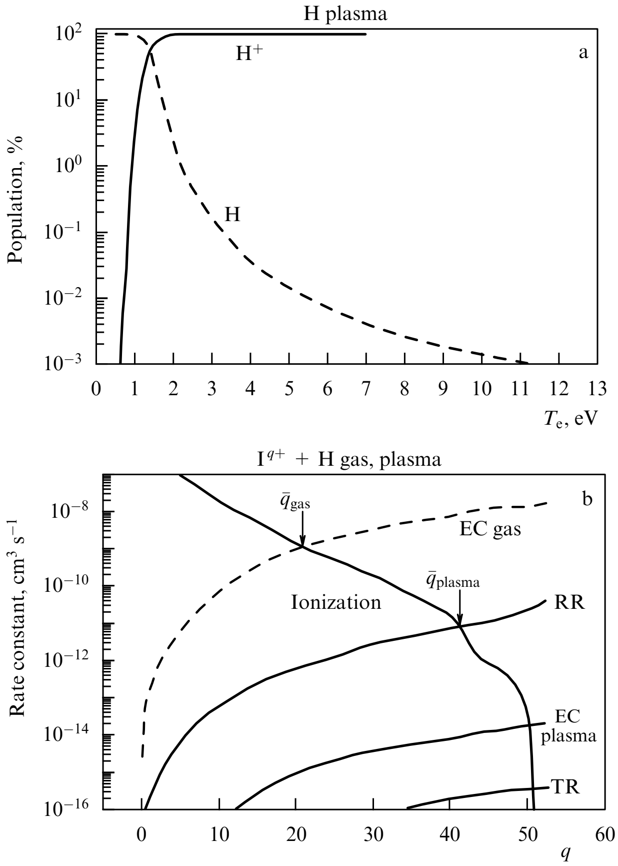

Figure 21. (a) Calculated relative concentrations of protons and neutral hydrogen atoms in a hydrogen plasma as a function of plasma temperature: the solid curve corresponds to protons, and the dashed line to hydrogen atoms. (Taken from Ref. [276].) b) Calculated ionization and recombination rate constants as a function of ion charge q for I^{q+} ions with an energy of 1.5 MeV/u passing through a cold hydrogen gas and an almost completely ionized hydrogen plasma with parameters: electron temperature $T_{\mathrm{e}} = 10$ eV, density $N_{\mathrm{e}} = 10^{17}$ cm^{-3}. EC gas (dashed line) and EC plasma (solid line) correspond to the rate constants of electron capture on bound electrons of hydrogen atoms in a gas and a plasma, respectively. The 'ionization' curve fits the ionization rate by the target particles, which is the same for gas and plasma if $q > 5$. Curves RR and TR fit the rates of radiative recombination and three-particle recombination, respectively. The processes of dielectronic recombination are not taken into account. The arrows indicate the average charge of iodine ions in a gas ($\bar{q}_{\mathrm{gas}} \approx 20$) and in a plasma ($\bar{q}_{\mathrm{plasma}} \approx 40$). The rate constants of processes are taken from Ref. [50].

6. Computer programs for calculating ion charge-state fractions

At present, there are a few computer programs for calculating the evolution of charge-state fractions, when the ion beam passes mainly through gaseous and solid media: ETACHA, CHARGE, and GLOBAL.

6.1 ETACHA code

ETACHA [277] is one of the first programs for calculating ion charge-state fractions in *solid* targets (foils) at energies $E = 10-80$ MeV/u, corresponding to the range of operation of the French accelerator GANIL (Grand Accélérateur National d'Ions Lourds). The program is based on the solution of linear differential balance equations (24), (25) in the independent particle model for incident ions having up to 28 (Ni) electrons, i.e., containing $1s^2, 2s^2, \ldots, 3d^{10}$ electron shells. The program also provides calculations of interaction cross sections in the first order of perturbation theory — loss, capture, excitation, and de-excitation — and takes into account the ion energy losses, i.e., the stopping power in matter (Section 3).

Despite the simplicity and ease of use, ETACHA has several disadvantages: first of all, a large calculation error at beam energies $E > 30$ MeV/u and also for ions heavier than argon, i.e., with $Z_N > 18$ (see Refs [72, 142, 278]).

Recently, a new version of the ETACHA program has been presented [279], where the range of applicability of the program has been extended to lower energies $E = 0.05-30$ MeV/u and also to heavier ions possessing up to 60 electrons (Fig. 22).

6.2 CHARGE and GLOBAL programs

The programs CHARGE and GLOBAL [72] are designed to calculate ion charge-state fractions in the range of high and *relativistic* energies $E \geqslant 100$ MeV/u for ions with charges $Z_N \geqslant 30$, passing through gaseous and solid targets. The programs are available for online use on the Internet [280].

The CHARGE program uses an analytical solution to the fraction problem in Allison's three-component model [127], and is applied for cases where nuclei and H- and He-like ions constitute the main fractions. The program also calculates electron loss, radiative and nonradiative capture cross sections, and approximately double-electron capture and ionization cross sections.

The GLOBAL program is based on the numerical solution of differential balance equations (24), (25) by the Runge–Kutta method for the number of ionic fractions up to $N \leqslant 28$, but allows for a large number of significant simplifications in the calculation of cross sections, which makes the program rather limited for use, especially, for large ion charges q and heavy-atom targets. The results of calculations with both programs coincide for a three-component problem. The accuracy of calculating fractions by the CHARGE and GLOBAL programs is within a factor of 2.

6.3 BREIT code

The BREIT program (Balance Rate Equations for Ion Transportation) was recently created to calculate ion charge-state fractions at energies $E = 50$ keV/u–50 GeV/u for the number of fractions $3 \leqslant N < 200$ [281] in various media: gases, solids, and plasmas. The program is based on the analytical solution of the balance equations (24), (25) by the diagonalization method of the interaction matrix, consisting of electron loss, capture, and other cross sections. Unlike the programs mentioned above, in the BREIT program the cross sections are set in the *input file*, which includes multiple-electron cross sections, and taking into account the target-density effect following the results obtained in Ref. [126]. Users of the BREIT code are free to choose the interaction cross sections in the framework of any approximation used for their calculation. Experimental data can also be utilized as input cross sections. The ability of taking into account the multiple-electron processes and the density effect in the BREIT input file is of great importance, because accounting for the density effect leads to a change in the average charge by a factor of 1.5–2 [282], and of multiple-electron processes by 20–30% [133]. The BREIT program is also available for online use on the Internet [283].

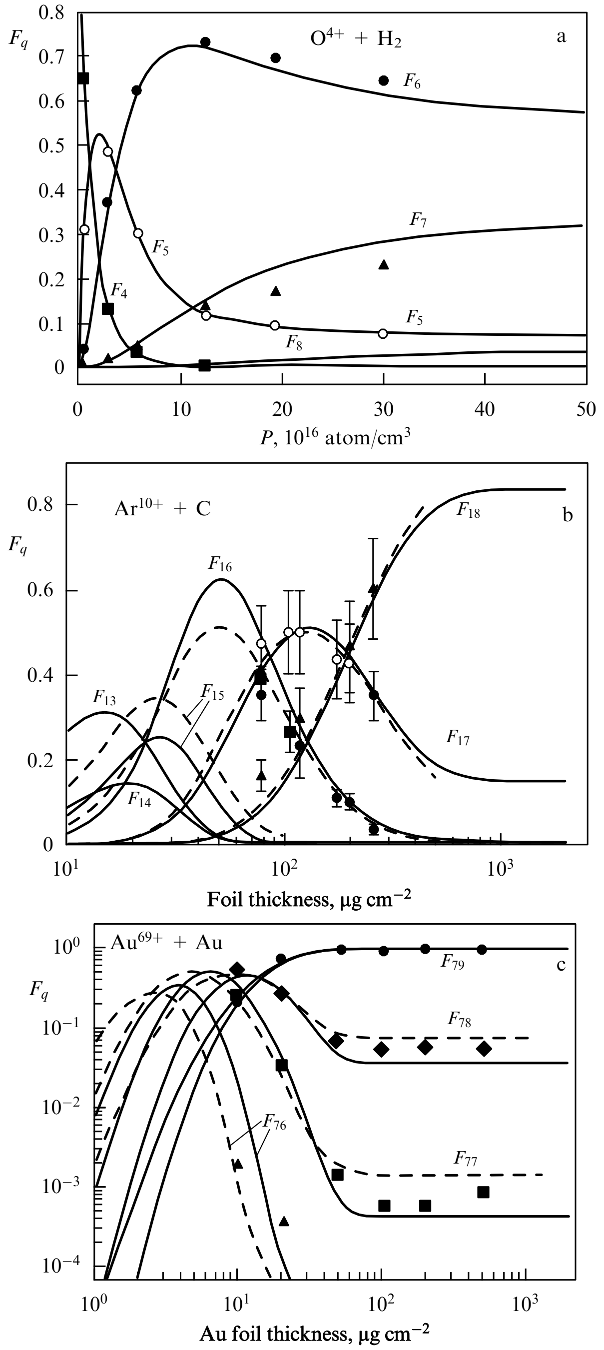

Figure 22. (a) Evolution of the fractions F_q $(4 \leqslant q \leqslant 7)$ of oxygen ions in collisions of 800-keV/u O^{4+} ions with hydrogen gas as a function of gas pressure. Symbols — experiment [284], and solid curves — calculation by the BREIT code with account for the density effect. (Taken from Ref. [281].) (b) Evolution of the fractions F_q $(13 \leqslant q \leqslant 18)$ of argon ions in collisions of 13.6-MeV/u Ar^{10+} ions with a carbon foil as a function of target thickness. Symbols with error bars — experiment [279], and solid curves — BREIT calculations with account for the density effect. (Taken from Ref. [281].) (c) Evolution of the fractions F_q $(76 \leqslant q \leqslant 79)$ of gold ions in collision of 1-GeV/u Au^{69+} ions with a gold foil as a function of target thickness. Symbols — experiment [72], and solid curves — BREIT calculations with account for the density effect. (Taken from Ref. [281].)

To calculate the ion charge-state fractions in plasma targets, the BREIT input file does not lean upon the cross sections, but on the *rate constants* $\langle Nv\sigma \rangle$ of reactions with account for additional (relative to gas and solid targets) processes, such as radiative and dielectronic recombinations, and ionization by free plasma electrons (see, e.g., Ref. [50] and Section 5.5), where N is the density of plasma particles.

Figure 22 plots experimental data for equilibrium and nonequilibrium fractions of light and heavy ions upon passage through gas and solid targets in comparison with calculated results obtained with the above programs (for more details, see paper [281]).

The fractions $F_q(x)$ of oxygen ions in collisions of 800-keV/u O^{4+} ions with hydrogen gas as a function of the gas density $P \leqslant 5 \times 10^{17}$ atom/cm^3 are shown in Fig. 22a. Experimental data [284] are marked by symbols, and the BREIT calculations by solid curves. In general, the experimental and calculated data are in good agreement with each other. The density effect was taken into account in calculating the BREIT cross sections. Since the equilibrium regime was not achieved in the experiment, equilibrium fractions calculated by the BREIT program are presented as follows: $F_5(\infty) \approx 0.066$, $F_6(\infty) \approx 0.55$, $F_7(\infty) \approx 0.34$, and $F_8(\infty) \approx 0.043$, equilibrium charge $\bar{q} \approx 6.4$, and equilibrium thickness $x_{\text{eq}} \approx 24$ μg cm^{-2}, which was obtained at hydrogen pressure $P \approx 120 \times 10^{16}$ atom/cm^3.

The evolution of argon ion fractions in carbon foils with the passage of 13.6-MeV/u Ar^{10+} ions is exemplified in Fig. 22b. Experimental data [284] are shown by symbols with experimental errors, new-ETACHA calculations are given by dashed curves [279] and the BREIT results are fitted by solid curves. Experimental data for $F_{16}(x)$, $F_{17}(x)$, and $F_{18}(x)$ fractions are in good agreement with calculations performed by both programs. According to the BREIT calculations, the equilibrium thickness of the target for this case is $x_{\text{eq}} \approx 1000$ μg cm^{-2}.

Figure 22c depicts the evolution of the $F_q(x)$ fractions of gold ions in relativistic collisions of Ne-like Au^{69+} ions with golden foil at the energy of 1 GeV/u. Symbols denote experimental data from Ref. [72], the dashed curves are the GLOBAL calculation [280], and the solid curves are the BREIT calculation [281]. Experimental data for the maximum fractions $F_{79}(x)$, $F_{78}(x)$, $F_{77}(x)$, and $F_{76}(x)$ agree with the calculations performed by both programs within a factor of 2.

6.4 Monte Carlo code for calculating charge-state fractions in plasmas

Recently (see Refs [114–116]), a Monte Carlo (MC) program was developed for calculating F_q fractions and energy loss in interactions of fast heavy-ion beams with a plasma at energies $E > 10$ MeV/u. The MC program uses a previous version of the ETACHA program [277] to calculate cross sections of radiative and nonradiative electron capture, ion ionization and excitation, as well as of de-excitation and recombination processes. Similarly to the ETACHA code, the MC program is able to perform calculations for ions with the number of electrons up to 28 in a plasma with an ion density of $10^{18} < N_{\text{i}} < 10^{23}$ cm^{-3} and a temperature of $10 < T < 200$ eV. In the MC program, the target-density effect is also taken into account.

As for the use of the programs for calculating the $F_q(x)$ fractions, it should be noted that the $F_q(x)$ magnitudes, obtained with the balance equations (24), (25), are very sensitive to the cross sections employed for description of ion interactions with the target particles. The accuracy of calculated *nonequilibrium* fractions is within a factor of 2, because experimental and theoretical single- and multiple-electron cross sections are known with an accuracy of 10–50%. The accuracy of the *equilibrium*-fraction calculations in gases and foils is a little bit higher because it depends mainly on ratios between single-electron loss-to-capture cross sections, which are obtained more precisely than the multiple-electron ones.

7. Use of charge-state fractions in applications

In this section, two examples of the application of equilibrium ion fractions are considered: the detection of superheavy elements in nuclear physics, and the synthesis of oxygen in the atmosphere of a star in astrophysics.

7.1 Detection of superheavy elements

The heaviest natural element on Earth is uranium (atomic number $Z = 92$), and chemical elements heavier than uranium, the so-called *superheavy* elements (SHEs), are produced by artificial nuclear fusion of the nuclei of two elements. SHEs exist a very short time and then decay. Recently (2010–2016), superheavy elements with $Z = 113 - 118$ have been synthesized. Table 3 shows a list of heavy and superheavy elements, together with their atomic numbers and some other characteristics.

The properties of atoms and ions of heavy and superheavy elements are of great interest in atomic physics (the structure of electron shells, QED effects), quantum chemistry, and, naturally, in nuclear physics in studying the structure of nuclear shells and the stability of isotopes, and in the search for an 'island of stability' (see Refs [131, 299–305] and references cited therein). Work on the creation and detection of SHEs is being intensively carried out at JINR (Dubna), the Institute of Physical and Chemical Research (RIKEN, Japan), Lawrence Berkeley National Laboratory (USA), Oak Ridge National Laboratory (USA), and the Helmholtz Centre for Heavy Ion Research (GSI) in Darmstadt (see Ref. [300]).

Superheavy elements are usually produced in interactions between ion beams and foils of heavy atom materials at collision energies of about several hundred keV/u, when the rate constants of the synthesis reactions are close to maximum. For example, in order to obtain ions of the ^{277}Cn isotope (nuclear charge $Z_{\text{N}} = 112$, mass $M = 277$ a.m.u.), the beams of zinc ions ($Z = 30$, $M = 70$) collide with lead foils ($Z = 82$, $M = 208$) at an energy of about 350 keV/u:

$$^{70}\text{Zn}^{\,p+} + {}^{208}\text{Pb} \to {}^{277}\text{Cn}^{\,q+} + \text{n}\,, \tag{82}$$

where p and q are the charge states of the ions.

One of the main methods for detecting superheavy elements is based on the property of *equilibrium* charge-state fractions of ions (Section 4.2), which do not depend on the charge state of the incident ions. This property of *atomic* interactions of ion beams with matter has formed the basis for the method of detecting heavy and superheavy elements. To detect SHEs, so-called *gas-filled separators* are exploited with H_2 or He gas or their mixture at a pressure of several mbars (see Refs [130, 131, 300–305]).

The distribution of F_q fractions of SHE (Cn^{q+}) ions over charge states q after nuclear reaction (82) is unknown, but if

Table 3. Periodic Table including atomic number Z of the element, symbol, name, mass M, electronic configuration of four outer shells, ionization potential IP, and references to experimental (exp.) or theoretical (theor.) papers where IP values were obtained. The half-lives of the most stable isotopes are also given from wikisite [298]. Elements Uue and Ubn mean 119th and 120th in Latin; they do not yet have a name.

Atomic number Z	Symbol	Name	Mass M, a.m.u.	Electronic configuration	IP, eV	IP, exp.	IP, theor.	Half-life
80	Hg	Mercury	201	$4f^{14}5p^65d^{10}6s^2$	10.44	[285]		
82	Pb	Lead	207	$5p^65d^{10}6s^26p^2$	7.42	[286]		
83	Bi	Bismuth	209	$5p^65d^{10}6s^26p^3$	7.29			2×10^{19} years
87	Fr	Francium	223	$5d^{10}6s^26p^67s^1$	4.07	[287]		22 min
88	Ra	Radium	226	$5d^{10}6s^26p^67s^2$	5.28	[288]		1600 years
89	Ac	Actinium	227	$6s^26p^67s^26d^1$	5.38	[289]		21.77 years
92	U	Uranium	238	$6p^65f^36d^17s^2$	6.19	[290]		4.5×10^9 years
98	Cf	Californium	251	$6s^26p^65f^{10}7s^2$	6.28			900 years
100	Fm	Fermium	257	$6s^26p^65f^{12}7s^2$	6.50			100.5 days
102	No	Nobelium	259	$6s^26p^65f^{14}7s^2$	6.63		[291]	58 min
103	Lr	Lawrencium	266	$6p^65f^{14}7s^27p^1$	4.90			11 h
104	Rf	Rutherfordium	267	$6p^65f^{14}6d^27s^2$	6.01		[292]	1.3 h
109	Mt	Meitnerium	278	$6p^65f^{14}6d^77s^2$	9.55			7.6 s
110	Ds	Darmstadtium	281	$6p^65f^{14}6d^87s^2$	10.38			3.7 min
111	Rg	Roentgenium	282	$6p^65f^{14}6d^97s^2$	11.21			2.1 min
112	Cn	Copernicium	285	$6p^65f^{14}6d^{10}7s^2$	12.03			8.9 min
113	Nh	Nihonium	286	$5f^{14}6d^{10}7s^27p^1$	4.10			19.6 s
114	Fl	Flerovium	289	$5f^{14}6d^{10}7s^27p^2$	8.54		[293]	1.1 min
115	Mc	Moscovium	289	$5f^{14}6d^{10}7s^27p^3$	5.58		[294]	220 ms
116	Lv	Livermorium	293	$5f^{14}6d^{10}7s^27p^4$	6.69			61 ms
117	Ts	Tennessine	294	$5f^{14}6d^{10}7s^27p^5$	7.64		[295]	78 ms
118	Og	Oganesson	294	$5f^{14}6d^{10}7s^27p^6$	8.32			890 μs
119	—	(Uue)	—	$6d^{10}7s^27p^68s^1$	4.79		[296]	
120	—	(Ubn)	—	$6d^{10}7s^27p^68s^2$	5.85		[297]	

ions are directed into a gas-filled separator, i.e., into a gas-collision chamber, then at a certain target thickness an *equilibrium* distribution of the SHE fractions is reached with an *average equilibrium* charge state $\bar{q}$ determined by formula (28):

$$\bar{q} = \sum_q qF_q(\infty)\,, \quad \sum_q F_q = 1\,, \tag{83}$$

in which the quantity $\bar{q}$ does not depend on the charge state q of initial ions. The distribution of SHE ions over q after a separator becomes much more narrow, and a contribution to sum (83) is made by a small number of fractions F_q. Knowing the equilibrium charge of the SHE under study, it is possible to determine the required *magnetic rigidity* $B\rho$ of the dipole in the separator, required for detecting the SHE element with a given average charge, using the Lorentz formula:

$$B\rho = \frac{Mv}{\bar{q}}\,. \tag{84}$$

Here B, ρ, M, and v are the magnetic field induction, radius of curvature, and mass and velocity of the ion, respectively. Thus, knowing the equilibrium average charge of the ion beam at the output from the target, the mass and velocity of the ion being studied, it is possible to determine the magnetic rigidity of the dipole magnet required for its detection, i.e., to determine the value of the required magnetic field B.

Determining magnetic rigidity $B\rho$ plays an important role in these experiments, because the number of generated superheavy ions is very small and significantly decreases as the atomic number Z increases: the rate of formation of synthesized ions can go from several thousand ions per day for relatively light ions up to one ion in a few weeks (!) for superheavy elements.

For a rough estimate of the average charge $\bar{q}$ of an SHE, the Bohr formula is usually invoked [Section 4.3, formula (34)]:

$$\bar{q} = vZ^{1/3}\,, \quad 1 < v < Z^{2/3}\,, \tag{85}$$

which holds true for ions with large Z_N and mediate ion velocities v. Bohr's formula (34) and other semiclassical and semiempirical formulas for the average charge, considered in Section 4, have a number of serious disadvantages. First of all, they do not account for the atomic structure of colliding

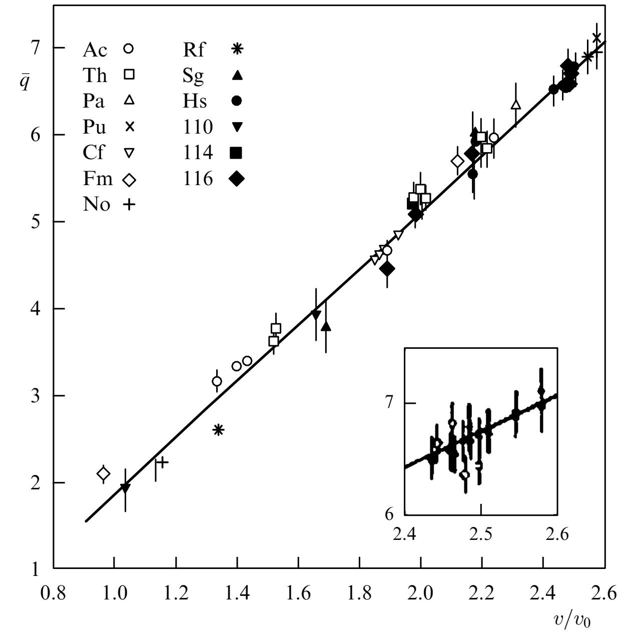

Figure 23. Experimental dependence of the equilibrium average charge $\bar{q}$ for ions with atomic number $Z = 89-116$ as a function of relative velocity v at a molecular hydrogen pressure of 1 Torr, obtained using DGFRS (Dubna Gas-Filled Recoil Separator). In the inset, the $\bar{q}$ values measured at 0.5 and 1.5 Torr (circles) for the number of atoms are added to those for No atoms, which are not described by the linear dependence (86) due to the influence of the density effect (hydrogen gas pressure) in the separator. (Taken from Ref. [130].)

particles or the target-density effect, both depending on the gas pressure in the separator. Experiments have shown that both effects are very significant, and semiempirical corrections must be introduced when applying formula (85) (see, e.g., Refs [303–305]).

Figure 23 shows experimental average charge values [130] for heavy and superheavy ions ($Z = 89-116$) as a function of relative velocity $v = 1-2.6$ a.u. measured at a molecular hydrogen pressure $P \sim 1$ Torr. Experimental data [130] are well approximated by the linear dependence of the average charge on velocity according to a formula close to Bohr's formula (85):

$$\bar{q} \approx 3.26v - 1.39\,. \tag{86}$$

At gas pressures of 0.5 and 1.5 Torr, experimental data differ from the linear dependence, as shown in the inset to figure, due to the target-density effect, which is not taken into account in formula (86).

Similar measurements of the average charge $\bar{q}$ of heavy and superheavy elements with atomic numbers $Z = 80-114$ were carried out on TASCA (TransActinide Separator and Chemistry Apparatus), GSI, Darmstadt, with He as a filling gas at pressures of $P = 0.2-2.0$ mbar and energies of several hundred keV/u [132]. The measured data are presented in Table 4 in comparison with Bohr's formula (85), $\bar{q}_B$, two semiempirical formulas SE1 and SE2, and the results $\bar{q}_{th}$ of atomic calculations performed in Ref. [132]. The formula SE1 for $\bar{q}$ is based on the semiempirical dependence obtained in Ref. [132] for SHEs up to Rg ($Z = 111$) at an H_2 gas pressure of 0.66 mbar. Average charge $\bar{q} \approx 6.8$ was predicted [132] using the modified formula ES1 for SHEs with $Z = 117$ at an He pressure of 0.8 mbar. This value was later used in Ref. [305] to detect the 117th element on a TASCA separator with the magnetic rigidity $B\rho = 2.20$ T m.

The $\bar{q}_{SE2}$ values in Table 4 were estimated from a semiempirical formula [140] obtained from analysis of the experimental data for ions with atomic numbers $Z = 1-92$ and gaseous targets with $Z = 1-54$. It can be seen from the table that Bohr's formula overestimates the experimental data by approximately a factor of 2. A slightly better result is given by the $\bar{q}_{SE2}$ formula, and the best agreement is achieved using the $\bar{q}_{SE1}$ formula.

It should be noted that the determination of magnetic rigidity by the average ion charge is a very complicated experimental task, which, as a rule, is usually solved semiempirically by calibration of a gas-filled separator with an average charge of isotopes of *stable* elements, taking into account the properties of a particular experimental setup.

Table 4. Experimental and theoretical average charges $\bar{q}$ for ions of heavy and superheavy elements. The atomic number of the element, the nuclear reaction for its production, the ion velocity in a.u., and the He pressure in the separator are also given. ER is evaporation residue, $\bar{q}_B$ is given by Bohr's formula (85), and $\bar{q}_{SE2}$ is the semiempirical formula [140]. (Taken from Ref. [132].)

ER	Z	Reaction	v, a.u.	P, mbar	$\bar{q}_{exp}$	$\bar{q}_B$	$\bar{q}_{SE1}$	$\bar{q}_{SE2}$	$\bar{q}_{th}$
^{180}Hg	80	^{144}Sm(^{40}Ar, 4n)	2.84	0.6	6.97 ± 0.30	12.2	7.40	9.07	6.04
^{188}Pb	82	^{144}Sm(^{48}Ca, 4n)	3.22	0.8	8.45 ± 0.19	14.0	8.60	10.55	7.83
^{205,206}Fr	87	^{181}Ta(^{30}Si, 3–4n)	2.04	0.5	5.67 ± 0.19	9.0	6.06	6.46	5.96
$^{209-211}$Ra	88	^{158,160}Gd(^{54}Cr, 3–4n)	3.17	0.6	9.37 ± 0.31	14.1	9.22	10.47	8.05
^{215}Ac	89	^{179}Au(^{22}Ne, 4n)	1.39	0.8	4.28 ± 0.42	6.2	4.20	4.22	5.75
^{221,222}U	92	^{176}Yb(^{50}Ti, 4–5n)	2.89	0.8	8.76 ± 0.29	13.0	8.64	9.80	8.27
^{252,254}No	102	^{206,208}Pb(^{48}Ca, 2n)	2.40	0.8	6.68 ± 0.18	11.2	6.57	8.30	7.23
$^{254-256}$Rf	104	^{206,208}Pb(^{50}Ti, 1–2n)	2.65	0.8	7.32 ± 0.25	12.5	7.30	9.37	7.02
^{288}Fl	114	^{244}Pu(^{48}Ca, 4n)	2.30	0.8	6.70 ± 0.37	11.1	6.97	8.28	8.02
^{287,288}Uup	115	^{243}Am(^{48}Ca, 3–4n)	2.28	0.8		11.1	7.03	8.23	7.70
^{293,294}Uus	117	^{249}Bk(^{48}Ca, 3–4n)	2.25	0.8		11.0	7.16	8.19	8.58
^{295,296}Uue	119	^{249}Bk(^{50}Ti, 3–4n)	2.42	0.8		11.9	7.83	8.92	8.73
^{295,296}Ubn	120	^{249}Cf(^{50}Ti, 3–4n)	2.43	0.8		12.0	7.93	9.02	9.03

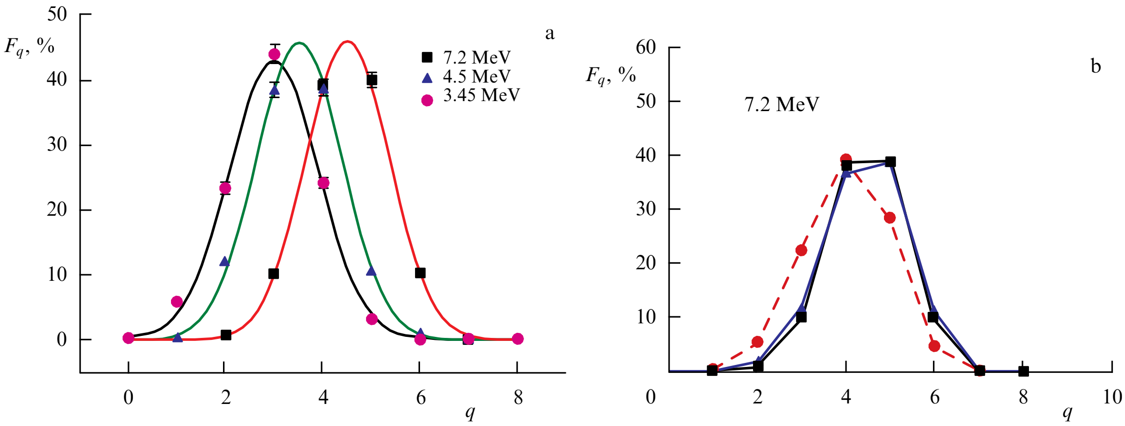

Figure 24. (Color online.) (a) Charge-state fractions F_q (%) of oxygen ions at energies of 7.2, 4.5, and 3.45 MeV: symbols — experimental data, and curves — Gaussian distributions. (b) Charge-state fractions F_q (%) of oxygen ions at 7.2 MeV energy: experiment (black curve) and theoretical calculations of the equilibrium distribution of ^{16}O ions passing through gaseous helium: red curve — calculated without DE, and blue curve — with DE accounted for. (Taken from Ref. [308].)

Table 5. Experimental equilibrium F_q (%) fractions of oxygen ions after their passing through gaseous helium at a pressure of 6 Torr at ion energies of 3.45, 4.5, and 7.2 MeV [308]. At the end of the table, average charges $\bar{q} = \sum qF_q$ are also given.

Energy, MeV	$q = 1+$	2+	3+	4+	5+	6+	$\bar{q}$
3.45	5.8 ± 0.2	23.2 ± 0.7	43.9 ± 1.3	24.0 ± 0.7	3.1 ± 0.1	—	2.95
4.5	—	11.8 ± 0.3	38.4 ± 1.1	38.7 ± 1.1	10.3 ± 0.3	0.8 ± 0.02	3.50
7.2	—	0.7 ± 0.02	10.2 ± 0.3	39.2 ± 1.1	39.8 ± 1.2	10.1 ± 0.3	4.48

In paper [132], for the first time, the average charges for SHEs with $Z = 80-120$ were calculated on the basis of *atomic calculations* of electron loss and capture cross sections, taking into account the density effect and using the solution of balance equations (24), (25) for equilibrium average ion charges. In Table 4, the data calculated this way are indicated by $\bar{q}_{\rm th}$; they agree with the experimental data within 20%. However, for precise measurements of SHEs, an accuracy on the order of a few percent is required.

7.2 Role of atomic processes in the stellar astrophysics

Atomic processes and the associated fractions of ion beams play an important role in the nuclear reactions proceeding in astrophysical objects. For example, the nuclear reactions

$$3\,{}^4\mathrm{He}^{++} \to {}^{12}\mathrm{C}\,, \quad {}^{12}\mathrm{C} + {}^4\mathrm{He} \to {}^{16}\mathrm{O} + \gamma \qquad (87)$$

for energies $E_{\rm cm} \leqslant 0.7$ MeV in the center-of-mass system play a key role in 'burning' helium in stars and determine the relative carbon-to-oxygen content of ^{12}C/^{16}O [306], which, in turn, affects the late stages of star evolution and nuclear fusion reactions in them. Here, γ means gamma quanta. The rate constant of the nuclear reaction ^{4}He(^{12}C, ^{16}O)γ has not been determined experimentally so far, although efforts have been made for about 50 years. This occurs because of the small value of the cross section and the energy range that is not yet achievable under laboratory conditions.

Studies of the measurement of the cross sections for the ^{4}He(^{12}C, ^{16}O)γ reaction at energies close to astrophysical conditions are being intensively carried out at the Kyushu University accelerator [307], where a ^{12}C beam is injected into an He gas target, and the resulting oxygen ions ^{16}O in one charge state are separated from the carbon beam and other particles by a gas-filled (helium) separator and recorded by the Si detector. To obtain the total cross section of the reaction ^{4}He(^{12}C, ^{16}O)γ, it is necessary to know all charge-state fractions F_q of the resulting ^{16}O ions, which depend on ion energy and He target density (the density effect, Section 5.4). Thus, in fact, the same experimental method for measuring ionic fractions and average ion charge states is used, as discussed in Section 7.1 for detecting superheavy elements.

Recently, equilibrium and nonequilibrium fractions of oxygen ions were measured in Ref. [308] at energies of 7.2, 4.5, and 3.45 MeV and at He-gas pressure of 6 Torr (density of 2.0×10^{17} cm^{-3}). The experimental results of the equilibrium distribution of fractions and average charges are given in Table 5. As the ion energy increases, the $\bar{q}$ value increases, and at a minimum experimental energy of 3.45 MeV, the fractions F_2, F_3, and F_4 make the main contribution to the average ion charge.

The experimental equilibrium fractions are described by a Gaussian distribution, as can be seen from Fig. 24a. Figure 24b shows the distribution of the equilibrium charge of oxygen ions at 7.2 MeV in comparison with the theoretical calculations performed with and without accounting for the density effect (DE). It can be seen that taking the effect into account substantially improves agreement between theory and experiment (for more details, see paper [308]). In the future, it is planned to carry out similar experiments at the Kyushu University accelerator at lower ion energies to determine the cross sections of nuclear fusion with the formation of oxygen ions.

8. Conclusions

Interactions of heavy ions with gaseous, solid, and plasma media are considered including ion slowing-down, charge-state fraction dynamics, charge-changing cross sections of ion collisions with particles, and the detection of superheavy elements. All these items are based on atomic interactions of colliding particles and their atomic structure: electron shells, the cross sections of ionization, recombination, excitation processes, radiative transition probabilities, and other characteristics.

The focus is on the analysis of processes involving heavy many-electron systems, which are more complicated and at the same time more interesting than processes involving a few-electron ions. In processes with many-electron atoms and ions, the electrons of the inner shells play a large, and often the major, role. The contribution from multielectron transitions to the total probability of processes increases, for example, the contribution to multiple-electron capture and loss of heavy ions in collisions with neutral target atoms reaches about 50%, which leads to a change in the equilibrium average charge of ions at the exit from the target by 20–30% and to an asymmetry of its Gaussian distribution over charge. The contribution of multiple-electron processes depends on the kinetic energy of the ions: it is large at low and medium energies, and becomes small at high and relativistic energies.

In the interaction of ions with matter, the role of the target density effect is also large, which significantly affects the electron-loss and electron-capture cross sections, the ion stopping power in matter, the equilibrium average charge of the ion beam, and so on. Therefore, when creating new computer programs for calculating the evolution of ion charge fractions based on solving balance equations with effective cross sections as coefficients, it is necessary to take into account two important factors: the contribution of multiple-electron processes, and the target-density effect. As for including the density effect, there are still unsolved problems, for example, the dependences of the multiple-electron loss and capture cross sections on the target density are still unknown. Experimental data related to these dependences are also absent. Theoretically, it is possible to estimate quite accurately the influence of the density effect on *single-electron* cross sections, which is a rather complicated problem, but it is not yet clear what the role is of the effect on *multiple-electron* cross sections, a role that is large and substantially affects many characteristics of ion interactions with media.

Another interesting area for future research is the interaction of ions with plasmas, which has been studied less deeply in detail both experimentally and theoretically than gaseous and solid targets (foils). First of all, this is due to the presence of a larger number of processes of ion beam interaction with plasma (radiative and dielectronic recombinations, triple recombination, etc.). In this case, the effect of dielectronic recombination processes on the stopping power of plasma media and the effective charge of ions in plasmas is large, which is primarily due to the complex atomic structure of heavy ions (high density of states). This problem is currently being solved on the basis of the quantum chaos method, which is used quite rarely. The processes of dielectronic recombination are especially important for studying the energy 'windows' of incident ions in a hot plasma, where the effective charge of the ion beam is much larger than that in a cold gas, also due to the contribution from dielectronic recombination processes.

Acknowledgments. The authors are grateful to H Weick, C Scheidenberger, J Khuyagbaatar, A Yakushev, O Rosmej, M Imai, Th Stöhlker, and I Tupitsyn for valuable discussions of the manuscript and fruitful remarks.

References

1. Betz H-D *Rev. Mod. Phys.* **44** 465 (1972)
2. Sellin I A (Ed.) *Structure and Collisions of Ions and Atoms* (Berlin: Springer-Verlag, 1978)
3. Ahlen S P *Rev. Mod. Phys.* **52** 121 (1980)
4. Betz H D, in *Applied Atomic Collisions Physics* Vol. 4 *Condensed Matter* (Ed. S Datz) (New York: Academic Press, 1983) p. 2
5. Ziegler J F, Biersack J P, Littmark U *The Stopping and Range of Ions in Solids* (The Stopping and Ranges of Ions of Matter, Vol. 1) (New York: Pergamon, 1985)
6. Amaldi U, Kraft G *Europhys. News* **36** 114 (2005)
7. Schardt D, Elsässer Th, Schulz-Ertner D *Rev. Mod. Phys.* **82** 383 (2010)
8. Nikoghosyan A et al. *Int. J. Radiat. Oncology Biol. Phys.* **58** 89 (2004)
9. Schmidt B, Wetzig K *Ion Beams in Materials Processing and Analysis* (Wien: Springer, 2013)
10. Sigmund P *Particle Penetration and Radiation Effects* Vol. 2 (Springer Series in Solid-State Sciences, Vol. 179) (Berlin: Springer, 2014)
11. Presnyakov L P *Sov. Phys. Usp.* **19** 387 (1976); *Usp. Fiz. Nauk* **119** 49 (1976)
12. Sobelman I I, Vainshtein L A, Yukov E A *Excitation of Atoms and Broadening of Spectral Lines* (Berlin: Springer-Verlag, 1981); Translated from Russian: Vainshtein L A, Sobelman I I, Yukov E A *Vozbuzhdenie Atomov i Ushirenie Spektral'nykh Linii* (Moscow: Nauka, 1979)
13. Presnyakov L P, Shevelko V P, Janev R K *Elementarnye Protsessy s Uchastiem Mnogozaryadnykh Ionov* (Elementary Processes Involving Multiply Charged Ions) (Moscow: Energoatomizdat, 1986)
14. Vainshtein L A, Shevelko V P *Struktura i Kharakteristiki Ionov v Goryachei Plazme* (The Structure and Characteristics of Ions in Hot Plasma) (Moscow: Nauka, 1986)
15. Janev R K et al. *Elementary Processes in Hydrogen–Helium Plasmas: Cross Sections and Reaction Rate Coefficients* (Berlin: Springer-Verlag, 1987)
16. Nikitin E E, Smirnov B M *Atomno-molekulyarnye Protsessy: v Zadachakh s Resheniyami* (Atomic-Molecular Processes) (Moscow: Nauka, 1988)
17. Parilis E S et al. *Ozhe-protsessy pri Atomnykh Stolknoveniyakh* (Auger Processes in Atomic Collisions) (Ed. O B Firsov) (Tashkent: FAN, 1989)
18. Fritsch W, Lin C D *Phys. Rep.* **202** 1 (1991)
19. Bransden B H, McDowell M R C *Charge Exchange and the Theory of Ion-Atom Collisions* (Oxford: Clarendon Press, 1992)
20. Janev R K (Ed.) *Atomic and Molecular Processes in Fusion Edge Plasmas* (New York: Plenum Press, 1995)
21. Lebedev V S, Beigman I L *Physics of Highly Excited Atoms and Ions* (Berlin: Springer-Verlag, 1998)
22. Smirnov B M *Phys. Usp.* **44** 221 (2001); *Usp. Fiz. Nauk* **171** 233 (2001)
23. Stolterfoht N, DuBois R D, Rivarola R D *Electron Emission in Heavy Ion-Atom Collisions* (Berlin: Springer, 1997)
24. Beyer H, Shevelko V P *Introduction to the Physics of Highly Charged Ions* (Bristol: IOP Publ., 2003)
25. Shevelko V P, Tawara H (Eds) *Atomic Processes in Basic and Applied Physics* (Berlin: Springer, 2012)
26. Tolstikhina I Yu, Shevelko V P *Phys. Usp.* **56** 213 (2013); *Usp. Fiz. Nauk* **183** 225 (2013)
27. Sharkov B Yu *Nucl. Instrum. Meth. Phys. Res. A* **577** 14 (2007)
28. Logan B G, Perkins L J, Barnard J J *Phys. Plasmas* **15** 072701 (2008)
29. Geissel H et al. *Nucl. Instrum. Meth. Phys. Res. B* **195** 3 (2002)
30. Geissel H, Münzenberg G, Riisager K *Annu. Rev. Nucl. Part. Sci.* **45** 163 (1995)
31. Fortov V E, Hoffmann D H H, Sharkov B Yu *Phys. Usp.* **51** 109 (2008); *Usp. Fiz. Nauk* **178** 113 (2008)
32. Dennerl K *Space Sci. Rev.* **157** 57 (2010)
33. Trautmann C, in *Ion Beams in Nanoscience and Technology* (Eds R Hellborg, H J Whitlow, Y Zhang) (Berlin: Springer, 2009) p. 369
34. International Atomic Energy Agency. Atomic Molecular Data Services, https://www-amdis.iaea.org/

35. FAIR Baseline Technical Report (2006), http://www.fair-center.eu/fileadmin/fair/publications_FAIR/FAIR_BTR_1.pdf; GSI. FAIR, https://www.gsi.de/forschungbeschleuniger/fair.htm
36. Wien W, Sitzungsber K *Sitzungsber. K. Preuß. Akad. Wiss.* 773 (1911)
37. Folger H (Ed.) "Heavy ion targets and related phenomena" *Nucl. Instrum. Meth. Phys. Res. A* **282** (1989) Special issue
38. Adams D P et al., Report SAND2015-8325 (Albuquerque, NM: Sandia National Laboratories, 2015)
39. Lebedev S G, Lebedev A S *Phys. Rev. ST Accel. Beams* **11** 020401 (2008)
40. Tahir N A et al. *Phys. Rev. E* **90** 063112 (2014)
41. Tahir N A et al. *J. Phys. A* **39** 4755 (2006)
42. Hoffmann D H H et al. *Phys. Rev. A* **42** 2313 (1990)
43. Gardès D et al. *Nucl. Instrum. Meth. Phys. Res. A* **415** 698 (1998)
44. Mintsev V et al. *Nucl. Instrum. Meth. Phys. Res. A* **415** 715 (1998)
45. Ogawa M et al. *Nucl. Instrum. Meth. Phys. Res. A* **464** 72 (2001)
46. Chabot M et al. *Phys. Rev. E* **51** 3504 (1995)
47. Rouille G et al. *Nucl. Instrum. Meth. Phys. Res. A* **464** 428 (2001)
48. Fleurier C et al. *J. Phys. Colloques* **49** C7-141 (1988)
49. Hoffmann D H H et al. *Phys. Scripta* **2006** 1 (2006)
50. Peter Th, Meyer-ter-Vehn J *Phys. Rev. A* **43** 1998 (1991); *Phys. Rev. A* **43** 2015 (1991)
51. Jacobi J et al. *Phys. Rev. Lett.* **74** 1550 (1995)
52. Alton G D, Sparrow R A, Olson R E *Phys. Rev. A* **45** 5957 (1992)
53. Obolensky O I et al. *Nucl. Instrum. Meth. Phys. Res. B* **266** 1623 (2008)
54. Scheidenberger Ch "Untersuchung der Abbremsung relativistischer Schwerionen in Materie im Energiebereich 100–1000 MeV/u", PhD Thesis (Giessen: Giessen Physikalische Institut, 1994)
55. Northcliffe L C, Schilling R F *Atom. Data Nucl. Data Tabl.* **7** 233 (1970)
56. Ziegler J F, Biersack J B "Computer programme SRIM-2000/01", http://www.srim.org
57. Vollmer O *Nucl. Instrum. Meth.* **121** 373 (1974)
58. Närmann A, Sigmund P *Phys. Rev. A* **49** 4709 (1994)
59. Landau L *J. Phys. USSR* **8** 201 (1944)
60. Vavilov P V *Sov. Phys. JETP* **5** 749 (1957); *Zh. Eksp. Teor. Fiz.* **32** 920 (1957)
61. Scheidenberger C, Geissel H *Nucl. Instrum. Meth. Phys. Res. B* **135** 25 (1998)
62. Andersen H H, Sigmund P (Eds) *Proc. of the Intern. Workshop on the Slowing Down of Ions STOPOI* (Nucl. Instrum. Meth. Phys. Res. B, Vol. 69, Iss. 1) (Amsterdam: North-Holland, 1992)
63. Bethe H A *Phys. Rev.* **89** 1256 (1953)
64. Highland V L *Nucl. Instrum. Meth.* **129** 497 (1975)
65. Lynch G R, Dahl O I *Nucl. Instrum. Meth. Phys. Res. B* **58** 6 (1991)
66. Eidelman S et al. (Particle Data Group) *Phys. Lett. B* **592** 1 (2004)
67. Lindhard J, Sørensen A H *Phys. Rev. A* **53** 2443 (1996)
68. Geissel H, Scheidenberger C *Nucl. Instrum. Meth. Phys. Res. B* **136–138** 114 (1998)
69. Geissel H, Report GSI-82-12-A (Darmstadt: GSI, 1982); https://cds.cern.ch/record/140718
70. Datz S *Nucl. Instrum. Meth. Phys. Res. B* **164–165** 1 (2000)
71. Stopping Power of Matter for Ions. Heavier Ions, https://www-nds.iaea.org/stopping/stopping_heav.html
72. Scheidenberger C et al. *Nucl. Instrum. Meth. Phys. Res. B* **142** 441 (1998)
73. Bethe H A, Salpeter E E *Quantum Mechanics of One- and Two-Electron Atoms* (Berlin: Springer, 1957)
74. Landau L D, Lifshitz E M *Quantum Mechanics: Non-Relativistic Theory* (Oxford: Pergamon Press, 1965); Translated from Russian: *Kvantovaya Mekhanika: Nerelyativistskaya Teoriya* (Moscow: Fizmatgiz, 1963)
75. "Stopping powers and ranges for protons and alpha particles", ICRU Report No. 49 (Bethesda, MD: International Commission on Radiation Units and Measurements, 1993)
76. Bloch F *Ann. Physik* **5** 285 (1933)
77. Barkas W H, Dyer N J, Heckman H H *Phys. Rev. Lett.* **11** 26 (1963)
78. Fermi E *Phys. Rev.* **57** 485 (1940)
79. Scheidenberger C et al. *Phys. Rev. Lett.* **73** 50 (1994)
80. Weick H et al. *Nucl. Instrum. Meth. Phys. Res. B* **164–165** 168 (2000)
81. Bimbot R et al. *Nucl. Instrum. Meth.* **174** 231 (1980)
82. Hibbert F, Bimbot R, Gauvin H *Nucl. Instrum. Meth. Phys. Res. B* **36** 357 (1989)
83. Anthony J M, Lanford W A *Phys. Rev. A* **25** 1868 (1982)
84. Pierce T E, Blann M *Phys. Rev.* **173** 390 (1968)
85. Hubert F, Bimbot R, Gauvin H *Atom. Data Nucl. Data Tabl.* **46** 1 (1990)
86. Brandt W, Kitagawa M *Phys. Rev. B* **25** 5631 (1982)
87. Rachno I L, Mokhov N V, Striganov S I, Fermilab-Conf-05-019-AD (Batavia, IL: Fermilab, 2005)
88. Hoffmann D H H et al. *Nucl. Instrum. Meth. Phys. Res. B* **90** 1 (1994)
89. Barriga-Carrasco M D *Phys. Rev. E* **88** 043107 (2013)
90. Janni J F *Atom. Data Nucl. Data Tabl.* **27** 147 (1982)
91. Ziegler J F *Handbook of Stopping Cross-sections for Energetic Ions in All Elements* (The Stopping and Ranges of Ions in Matter, Vol. 5) (New York: Pergamon Press, 1980); Littmark U, Ziegler J F *Handbook of Range Distributions for Energetic Ions in All Elements* (The Stopping and Ranges of Ions in Matter, Vol. 6) (New York: Pergamon Press, 1980)
92. Bimbot R *Nucl. Instrum. Meth. Phys. Res. B* **69** 1 (1992)
93. Stopping-Power and Range Tables for Electrons, Protons, and Helium Ions, https://www.nist.gov/pml/data/star/index.cfm/
94. International Commission on Radiation Units and Measurements, Inc. (ICRU), https://www.icru.org/
95. Paul H, Schinner A *Nucl. Instrum. Meth. Phys. Res. B* **209** 252 (2003)
96. Paul H "Stopping power of matter for ions graphs. Data, comments and programs", https://www-nds.iaea.org/stopping/
97. Paul H, Schinner A *Nucl. Instrum. Meth. Phys. Res. B* **195** 166 (2002)
98. Bragg W H, Kleeman R *Philos. Mag. A* **8** 726 (1904)
99. Tsujii H et al. (Eds) *Carbon-Ion Radiotherapy* (Tokyo: Springer, 2014)
100. Bohr N *Philos. Mag.* **30** 581 (1915)
101. Nardi E, Zinamon Z *Phys. Rev. Lett.* **49** 1251 (1982)
102. Cowern N E B *J. Phys. Colloques* **44** C8-107 (1983)
103. Basko M M *Sov. J. Plasma Phys.* **10** 689 (1984); *Fiz. Plazmy* **10** 1195 (1984)
104. Meyer-ter-Vehn J et al. *Phys. Plasmas* **2** 1313 (1990)
105. Zwicknagel G, Toepffer C, Reinhard P-G *Phys. Rep.* **309** 117 (1999); *Phys. Rep.* **314** 671 (1999)
106. Shibata K et al. *J. Appl. Phys.* **91** 4833 (2002)
107. Hasegawa J et al. *Laser Part. Beams* **21** 7 (2003)
108. Hoffmann D H H et al. *Z. Phys. A* **30** 339 (1988)
109. Hoffmann D H H et al. *Phys. Rev. A* **42** 2313 (1990)
110. Jacoby J et al. *Phys. Rev. Lett.* **74** 1550 (1995)
111. Engelbrecht M et al. *Nucl. Instrum. Meth. Phys. Res. A* **415** 621 (1998)
112. Gardes D et al. *Phys. Rev. A* **46** 5101 (1992)
113. Rosmej F B et al. *Phys. Rev. E* **66** 056402 (2002)
114. Frank A et al. *Phys. Rev. E* **81** 026401 (2010)
115. Frank A et al. *Phys. Rev. Lett.* **110** 115001 (2013)
116. Ortner A et al. *Phys. Rev. E* **91** 023104 (2015)
117. Lassen N O *Kgl. Danske Vidensk. Selskab. Math.-Fys. Medd.* **26** (5) (1951)
118. Lassen N O *Kgl. Danske Vidensk. Selskab. Math.-Fys. Medd.* **26** (12) (1951)
119. Geissel H et al. *Phys. Lett. A* **99** 77 (1983)
120. Bohr N, Lindhard J *Kgl. Danske Vidensk. Selskab. Math.-Fys. Medd.* **28** (7) (1954)
121. Betz H D, Grodzins L *Phys. Rev. Lett.* **25** 211 (1970)
122. Miyoshi T et al. *Nucl. Instrum. Meth. Phys. Res. B* **258** 329 (2007)
123. Fettouhi A et al. *Nucl. Instrum. Meth. Phys. Res. B* **245** 32 (2006)
124. Ogawa H et al. *Phys. Rev. A* **75** 020703(R) (2007)
125. Geissel H et al. *Nucl. Instrum. Meth. B* **194** 21 (1982)
126. Shevelko V P et al. *J. Phys. B* **38** 2675 (2005)
127. Allison S K *Rev. Mod. Phys.* **30** 1137 (1958)
128. Datz S et al. *Phys. Rev. A* **2** 430 (1970)
129. Imai M et al. *Nucl. Instrum. Meth. Phys. Res. B* **267** 2675 (2009)
130. Oganessian Yu Ts et al. *Phys. Rev. C* **64** 064309 (2001)
131. Oganessian Yu Ts, Utyonkov V K *Rep. Prog. Phys.* **78** 036301 (2015)
132. Khuyagbaatar J et al. *Phys. Rev. A* **88** 042703 (2013)
133. Shevelko V P, Winckler N, Litsarev M S *Nucl. Instrum. Meth. Phys. Res. B* **330** 82 (2014)

134. Bohr N *Phys. Rev.* **58** 654 (1940)
135. Bohr N *Phys. Rev.* **59** 270 (1941)
136. Lamb W E (Jr.) *Phys. Rev.* **58** 696 (1940)
137. Betz H-D et al. *Phys. Lett.* **22** 643 (1966)
138. Nikolaev V S, Dmitriev I S *Phys. Lett. A* **28** 277 (1968)
139. Shima K, Kuno N, Yamanouchi M *Phys. Rev. A* **40** 3557 (1989)
140. Schiwietz G, Grande P L *Nucl. Instrum. Meth. Phys. Res. B* **175–177** 125 (2001)
141. To K X, Drouin R *Nucl. Instrum. Meth.* **160** 461 (1979)
142. Miyoshi T "Penetration of fast positive ions through carbon foils: analysis of density effects", PhD (Chiba, Japan: NIRS, 2009)
143. Eichler J, Stöhlker Th *Phys. Rep.* **439** 1 (2007)
144. Loand H H, Tite W L *Atom. Data Nucl. Data Tabl.* **1** 305 (1969)
145. Dehmel R C, Chan H K, Fleischmann H H *Atom. Data Nucl. Data Tabl.* **5** 231 (1973)
146. Erb W, Report GSI-P-78 (Darmstadt: GSI, 1978)
147. Franzke B *IEEE Trans. Nucl. Sci.* **28** 2116 (1981)
148. Stohlker T et al. *J. Phys. B* **25** 4527 (1992)
149. Ma X et al. *Phys. Rev. A* **64** 012704 (2001)
150. Weber G et al. *Phys. Rev. ST Accel. Beams* **12** 084201 (2009)
151. Weber G et al. *Phys. Rev. ST Accel. Beams* **18** 034403 (2015)
152. Olson R E et al. *J. Phys. B* **35** 1893 (2002)
153. Olson R E et al. *J. Phys. B* **37** 4539 (2004)
154. Perumal A N et al. *Nucl. Instrum. Meth. Phys. Res. B* **227** 251 (2005)
155. Mueller D et al. *Phys. Plasmas* **8** 1753 (2001)
156. Alonso J, Gould H *Phys. Rev. A* **26** 1134(R) (1982)
157. Kuboki H et al. *Phys. Rev. ST Accel. Beams* **13** 093501 (2010)
158. Okuno H et al. *Phys. Rev. ST Accel. Beams* **14** 033503 (2011)
159. Imao H et al. *Phys. Rev. ST Accel. Beams* **15** 123501 (2012)
160. DuBois R D et al. *Phys. Rev. A* **68** 042701 (2003)
161. Santos A C F, DuBois R D *Phys. Rev. A* **69** 042709 (2004)
162. Voitkiv A, Ullrich J *Relativistic Collisions of Structured Atomic Particles* (Berlin: Springer, 2008)
163. Tolstikhina I Yu, Shevelko V P *JETP Lett.* **94** 152 (2011); *Pis'ma Zh. Eksp. Teor. Fiz.* **94** 157 (2011)
164. Shevelko V P et al. *Nucl. Instrum. Meth. Phys. Res. B* **278** 63 (2012)
165. Presnyakov L P, Ulantsev A D *Sov. J. Quantum Electron.* **4** 1320 (1975); *Kvantovaya Elektron.* **1** 3277 (1974)
166. Chibisov M I *JETP Lett.* **24** 46 (1976); *Pis'ma Zh. Eksp. Teor. Fiz.* **24** 56 (1976)
167. Thwaites D I *Nucl. Instrum. Meth. Phys. Res. B* **12** 84 (1985)
168. Olson R E, Ullrich J, Schmidt-Böcking H *Phys. Rev. A* **39** 5572 (1989)
169. Belkić D, Mančev I, Hanssen J *Rev. Mod. Phys.* **80** 249 (2008)
170. Perez J A, Olson R E, Beiersdorfer P *J. Phys. B* **34** 3063 (2001)
171. Blank I et al. *Phys. Rev. A* **85** 022712 (2012)
172. Shevelko V P et al. *J. Phys. B* **37** 201 (2004)
173. Schlachter A S et al. *Phys. Rev. A* **27** 3372(R) (1983)
174. Olson R E et al. *Nucl. Instrum. Meth. Phys. Res. A* **544** 333 (2005)
175. Crandall D H et al. *Phys. Rev. Lett.* **36** 858 (1976)
176. Klinger H, Muller A, Salzborn E *J. Phys. B* **8** 230 (1975)
177. Müller A, Salzborn E *Phys. Lett. A* **62** 391 (1977)
178. Crandall D H, Phaneuf R A, Meyer F W *Phys. Rev. A* **22** 379 (1980)
179. Tawara H et al. *J. Phys. B* **18** 337 (1985)
180. Müller A et al. *Phys. Rev. A* **33** 3010 (1986)
181. Selberg N, Biedermann C, Cederquist H *Phys. Rev. A* **54** 4127 (1996)
182. Selberg N, Biedermann C, Cederquist H *Phys. Rev. A* **56** 4623 (1997)
183. Kimura M et al. *J. Phys. B* **28** L643 (1995)
184. Nakamura N et al. *J. Phys. B* **28** 2959 (1995)
185. Cocke C L, Olson R E *Phys. Rep.* **205** 153 (1991)
186. Knudsen K, Haugen H K, Hvelplund P *Phys. Rev. A* **24** 2287(R) (1981)
187. Nakai Y et al. *Phys. Scripta* **1989** 77 (1989)
188. Stolterfoht N et al. *Phys. Rev. Lett.* **99** 103201 (2007)
189. Deumens E et al. *Rev. Mod. Phys.* **66** 917 (1994)
190. Stolterfoht N et al. *Phys. Rev. A* **81** 052704 (2010)
191. Cabrera-Trujillo R et al. *Phys. Rev. A* **83** 012715 (2011)
192. Barragán P et al. *Phys. Rev. A* **82** 030701(R) (2010)
193. Tolstikhina I Yu, Kato D, Shevelko V P *Phys. Rev. A* **84** 012706 (2011)
194. Loreau J et al. *Phys. Rev. A* **84** 052720 (2011)
195. Tolstikhina I Yu et al. *J. Phys. B* **45** 145201 (2012)
196. Tolstikhina I Yu et al. *J. Phys. B* **47** 035206 (2014)
197. Zhao S et al. *Phys. Lett. A* **379** 319 (2015)
198. Solov'ev E A *Sov. Phys. Usp.* **32** 228 (1989); *Usp. Fiz. Nauk* **157** 437 (1989)
199. Solov'ev E A *J. Phys. B* **38** R153 (2005)
200. Tolstikhina I Yu, Tolstikhin O I *Phys. Rev. A* **92** 042707 (2015)
201. Komarov I V, Ponomarev L I, Slavyanov S Yu *Sferoidal'nye i Kulonovskie Sferoidal'nye Funktsii* (Spheroidal and Coulomb Spheroidal Functions) (Moscow: Nauka, 1976)
202. Solov'ev E A, in *ITAMP Workshop on Hidden Crossings in Ion-Atom Collisions and in Other Nonadiabatic Transitions* (Cambridge: Harvard Smithsonian Center for Astrophysics, 1991)
203. Liu C-N et al. *Phys. Rev. A* **67** 052705 (2003)
204. Andreić Ž, Kunze H-J, Tolstikhina I *Opt. Lett.* **40** 2600 (2015)
205. Kunze H J, Ellwi S S, Andreić Ž *Czech. J. Phys.* **56** B280 (2006)
206. Kunze H-J, Ellwi S S, Andreić Ž *Phys. Lett. A* **334** 37 (2005)
207. Matthews D L et al. *Phys. Rev. Lett.* **54** 110 (1985)
208. Suckewer S et al. *Phys. Rev. Lett.* **55** 1753 (1985)
209. Zhang J (Ed.) *X-Ray Lasers 2004, Proc. of the 9th Intern. Conf. on X-Ray Lasers, Beijing, China, 24–28 May 2004* (Institute of Physics Conf. Ser., No. 186) (Bristol: CRC Press, 2005)
210. Daido H *Rep. Prog. Phys.* **65** 1513 (2002)
211. Elton R C *X-Ray Lasers* (Boston: Academic Press, 1990)
212. Shin H-J, Kim D-E, Lee T-N *Phys. Rev. E* **50** 1376 (1994)
213. Aschke L et al. *J. Phys. IV* **11** Pr2-547 (2001)
214. Watson R L et al. *Phys. Rev. A* **67** 022706 (2003)
215. Meyerhof W E et al. *Phys. Rev. A* **32** 3291 (1985)
216. Anholt R et al. *Phys. Rev. A* **32** 3302 (1985)
217. Anholt R, Meyerhof W E *Phys. Rev. A* **33** 1556 (1986)
218. Anholt R et al. *Phys. Rev. A* **33** 2270 (1986)
219. Anholt R, Becker U *Phys. Rev. A* **36** 4628 (1987)
220. Stöhlker Th et al. *Nucl. Instrum. Meth. Phys. Res. B* **61** 408 (1991)
221. Scheidenberger C et al. *Nucl. Instrum. Meth. Phys. Res. B* **90** 36 (1994)
222. Stöhlker Th et al. *Phys. Rev. A* **51** 2098 (1995)
223. Stöhlker Th et al. *Phys. Rev. A* **57** 845 (1998)
224. Matveev V I, Sidorov D B *Tech. Phys.* **52** 839 (2007); *Zh. Tekh. Fiz.* **77** (7) 18 (2007)
225. Tolstikhina I Yu et al. *JETP* **119** 1 (2014); *Zh. Eksp. Teor. Fiz.* **146** 5 (2014)
226. Song M-Y et al. *Nucl. Instrum. Meth. Phys. Res. B* **267** 2369 (2009)
227. Shevelko V P et al. *J. Phys. B* **43** 215202 (2010)
228. Shevelko V P et al. *Nucl. Instrum. Meth. Phys. Res. B* **269** 1455 (2011)
229. Omet C et al. *New J. Phys.* **8** 284 (2006)
230. Tolstikhina I Yu, Shevelko V P *Phys. Scripta* **90** 074033 (2015)
231. McGuire J H, Weaver L *Phys. Rev. A* **16** 41 (1977)
232. Cocke C L *Phys. Rev. A* **20** 749 (1979)
233. Horbatsch M *Z. Phys. D* **21** S63 (1991)
234. Horbatsch M *J. Phys. B* **25** 3797 (1992)
235. Berg H et al. *J. Phys. B* **21** 3929 (1988)
236. Berg H, PhD Thesis (Darmstadt: GSI, 1993); Report GSI-93-12 (Darmstadt: GSI, 1993)
237. Vane C R et al. *Phys. Scripta* **1997** 167 (1997)
238. Fritzsche S, Surzhykov A, Stöhlker Th *Phys. Rev. A* **72** 012704 (2005)
239. Raisbeck G, Yiou F *Phys. Rev. A* **4** 1858 (1971)
240. Schnopper H W et al. *Phys. Rev. Lett.* **29** 898 (1972)
241. Kienle P et al. *Phys. Rev. Lett.* **31** 1099 (1973)
242. Eichler J, Chan F T *Phys. Rev. A* **20** 104 (1979)
243. Eichler J K M *Phys. Rev. A* **23** 498 (1981)
244. Eichler J *Phys. Rev. A* **32** 112 (1985)
245. Ichihara A, Shirai T, Eichker J *Phys. Rev. A* **49** 1875 (1994)
246. Eichler J, Meyerhof W E *Relativistic Atomic Collisions* (San Diego: Academic Press, 1995)
247. Stobbe M *Ann. Physik* **7** 661 (1930)
248. Kim Y S, Pratt R H *Phys. Rev. A* **27** 2913 (1983)
249. Ichihara A, Shirai T, Eichler J *Atom. Data Nucl. Data Tabl.* **55** 63 (1993)
250. Iåhihara A, Eichler J *Atom. Data Nucl. Data Tabl.* **74** 1 (2000)
251. Stöhlker Th et al. *Phys. Rev. A* **58** 2043 (1998)
252. Ogawa H et al. *Phys. Rev. A* **75** 020703(R) (2007)
253. Ryding G, Betz H D, Wittkower A B *Phys. Rev. Lett.* **24** 123 (1970)
254. Miyoshi T et al. *Nucl. Instrum. Meth. Phys. Res. B* **251** 79 (2006)

255. Hickok R L *Rev. Sci. Instrum.* **38** 142 (1967)
256. Kramers H A *Philos. Mag.* **46** 836 (1923)
257. Pajek M, Schuch R *Phys. Lett. A* **166** 235 (1992)
258. Omidvar K, McAllister A M *Phys. Rev. A* **51** 1063 (1995)
259. Müller A, Schippers S, in *The Physics of Multiply and Highly Charged Ions* Vol. 1 (Ed. F J Currell) (Dordrecht: Kluwer Acad. Publ., 2003) p. 269
260. Schippers S et al. *Phys. Rev. A* **83** 012711 (2011)
261. Müller A *Atoms* **3** 120 (2015)
262. Gabriel A H, in *Highlights of Astronomy, As Presented at the XIVth General Assembly of the I.A.U. 1970* (Ed. C De Jager) (Dordrecht: Reidel, 1971) p. 486
263. Müller A *Adv. Atom. Mol. Opt. Phys.* **55** 293 (2008)
264. Schippers S et al. *Phys. Rev. A* **62** 022708 (2000)
265. Flambaum V V et al. *Phys. Rev. A* **66** 012713 (2002)
266. Gribakin G F, Sahoo S *J. Phys. B* **36** 3349 (2003)
267. Dzuba V A et al. *Phys. Rev. A* **86** 022714 (2012)
268. Dzuba V A et al. *Phys. Rev. A* **88** 062713 (2013)
269. Lotz W *J. Opt. Soc. Am.* **6** 206 (1970)
270. Fisher V et al. *J. Phys. B* **28** 3027 (1995)
271. Shevelko V P, Tawara H *J. Phys. B* **28** L589 (1995)
272. Bélenger C et al. *J. Phys. B* **30** 2667 (1997)
273. Shevelko V P et al. *J. Phys. B* **38** 525 (2005)
274. Shevelko V P et al. *J. Phys. B* **39** 1499 (2006)
275. Gurevich A V, Pitaevskii L P *Sov. Phys. JETP* **19** 870 (1964); *Zh. Eksp. Teor. Fiz.* **46** 1281 (1964)
276. House L L *Astrophys. J. Suppl.* **8** 307 (1964)
277. Rozet J P, Stéphan C, Vernhet D *Nucl. Instrum. Meth. Phys. Res. B* **107** 67 (1996)
278. Sato Y et al. *Nucl. Instrum. Meth. Phys. Res. B* **225** 439 (2004)
279. Lamour E et al. *Phys. Rev. A* **92** 042703 (2015)
280. LISE++. Version 6.3, http://lise.nscl.msu.edu/6_3/lise++_6_3.pdf
281. Winckler N et al. *Nucl. Instrum. Meth. Phys. Res. B* **392** 67 (2017)
282. Shevelko V P, Winckler N, Tolstikhina I Yu *Nucl. Instrum. Meth. Phys. Res. B* **377** 77 (2016)
283. BREIT. Balance rate equations for ion transportation, http://breit.gsi.de
284. Liu W et al. *Nucl. Instrum. Meth. Phys. Res. A* **496** 198 (2003)
285. Baig M A *J. Phys. B* **16** 1511 (1983)
286. Wood D R, Andrew K L *J. Opt. Soc. Am.* **58** 818 (1968)
287. Arnold E et al. *J. Phys. B* **23** 3511 (1990)
288. Armstrong J A, Wynne J J, Tomkins F S *J. Phys. B* **13** L133 (1980)
289. Roßnagel J et al. *Phys. Rev. A* **85** 012525 (2012)
290. Coste A et al. *J. Opt. Soc. Am.* **72** 103 (1982)
291. Borschevsky A et al. *Phys. Rev. A* **75** 042514 (2007)
292. Eliav E, Kaldor U, Ishikawa Y *Phys. Rev. Lett.* **74** 1079 (1995)
293. Landau A et al. *J. Chem. Phys.* **114** 2977 (2001)
294. Eliav E, Kaldor U, Ishikawa Y *Mol. Phys.* **94** 181 (1998)
295. Chang Z, Li J, Dong C *J. Phys. Chem. A* **114** 13388 (2010)
296. Eliav E et al. *Chem. Phys.* **311** 163 (2005)
297. Borschevsky A et al. *Phys. Rev. A* **87** 022502 (2013)
298. Periodic table, https://en.wikipedia.org/wiki/Periodic_table
299. Oganessian Yu Ts *Pure Appl. Chem.* **76** 1715 (2004)
300. Düllmann C E et al. (Eds) *Nucl. Phys. A* **944** (2015) Special Issue on Superheavy Elements
301. Morita K et al. *Nucl. Instrum. Meth. Phys. Res. B* **70** 220 (1992)
302. Leino M *Nucl. Instrum. Meth. Phys. Res. B* **126** 320 (1997)
303. Gregorich K E et al. *Phys. Rev. C* **72** 014605 (2005)
304. Khuyagbaatar J et al. *Nucl. Instrum. Meth. Phys. Res. A* **689** 40 (2012)
305. Khuyagbaatar J et al. *Phys. Rev. Lett.* **112** 172501 (2014)
306. Weaver T A, Woosley S E *Phys. Rep.* **227** 65 (1993)
307. Fujita K et al. *AIP Conf. Proc.* **1269** 289 (2010)
308. Liu S et al. *Nucl. Instrum. Meth. Phys. Res. B* **328** 14 (2014)